Master thesis and internship[BR]- Master's thesis : Design of a reflective infrared spectrograph for exoplanet spectroscopy[BR]- Integration internship

Auteur : Dubuc, Armand
Promoteur(s) : Loicq, Jerome
Faculté : Faculté des Sciences appliquées
Diplôme : Master en ingénieur civil en aérospatiale, à finalité spécialisée en "aerospace engineering"
Année académique : 2020-2021
URI/URL : http://hdl.handle.net/2268.2/11475

LIÈGE université

CENTRE SPATIAL DE LIÈGE

Design of a reflective infrared spectrograph for exoplanet spectroscopy

University of Liège - School of Engineering and Computer Science

Master's thesis carried out to obtain the degree of Master of Science in Aerospace Engineering specialised in Space and Optics Engineering

Armand Dubuc

Supervisor
Pr Jérôme Loicq

Co-supervisor
Ir Colin Dandumont

Research Center
CSL - Centre Spatial de Liège

Academic year
2020 - 2021

Table of contents

List of Figures

List of Tables

Abstract

This master thesis is dedicated to the design of a thermal infrared, single-mode fibre-fed spectrograph associated with a ground-based nulling interferometer. This is done in the framework of SCIFY, a European Research Council (ERC) Consolidator project lead by Denis Defrère and dedicated to the spectroscopy of exoplanets. The configuration is chosen to be entirely reflective as an alternative to the grism design. The instrument operates in the L band ($3.5 - 4\,\mu$m) in which water and methane have strong signatures, and aims to achieve a resolution power of $R = 2000$. The different considerations related to ground-based spectroscopy are presented. Several methods to reduce off-axis aberration are also investigated. The spectrograph is analysed with ray-tracing software (CODE-V) and optimised to meet the scientific requirements.

Key words: thermal infrared spectroscopy, fiber-fed, exoplanets, SCIFY.

Ce mémoire est consacré à la conception d'un spectrographe en infrarouge thermique à alimentation par des fibres optiques monomodes et associé à un interféromètre de type nulling au sol. Ceci est réalisé dans le cadre de SCIFY, un projet financé par le Conseil européen de la recherche (CER), dirigé par Denis Defrère et consacré à la spectroscopie des exoplanètes. Une configuration réflective est analysée afin de proposer une alternative au design possédant un grism. L'instrument opère dans la bande L ($3.5 - 4\,\mu$m) dans laquelle l'eau et le méthane ont de fortes signatures spectrales, et vise à atteindre un pouvoir de résolution de $R = 2000$. Les différentes considérations liées à la spectroscopie au sol sont présentées. Plusieurs méthodes pour réduire l'aberration hors axe sont égalements étudiées. Le spectrograph est analysé à l'aide d'un logiciel de ray-tracing (CODE-V) et optimisé pour répondre aux exigences scientifiques.

Mots clés: spectroscopie en infrarouge thermique, fibre optiques, exoplanètes, SCIFY.

Acknowledgements

First of all, I would like to thank Professor Jérôme Loicq who made it possible for me to do this master thesis. Our weekly meetings allowed me to progress without too much blockage during the whole semester. Thank you also for reviewing my thesis.

Secondly, I would like to thank my co-supervisor Colin Dandumont who gave me a vast amount of literature as well as great advice that allowed me to start my work on a solid basis. Also thank you for the time you spent proofreading my work.

Then, I want to express my gratitude to Alexandra Amazzoli, optical designer of the SCIFY team at CSL who helped me to understand the optimization processes and macros of CODE-V.

Also, thank you to my roommates who were also my co-workers during the entire year. The mutual help we gave each other helped a lot and gave me motivation.

Finally, I would like to thank my family and friends that supported me. More specifically to my mother who travelled hours by train to bring me the PC charger that I forgot at home two days before the deadline of the manuscript. Also thank you to my sister who helped with the proofreading.

Chapter 1

Introduction

The purpose of this master thesis, resulting from the collaboration between the SCIFY project and the Centre Spatial de Liège (CSL) of the Liège University (ULiège), is to propose a single-mode, fibre-fed, reflective spectrograph design associated with a nulling interferometer for the characterization of extra-solar planetary systems.

This first chapter introduces the scientific motivations for the detection and characterization of exoplanets. Also, the SCIFY project is described together with the scientific requirements. In chapter 2, a general overview of ground-based spectroscopy is presented through state-of-the-art of current and future facilities and their instruments. Next, the different limitations associated with ground-based spectroscopy are explored. Thereafter, in chapter 3 the theoretical background for spectrographs as well as the different existing configurations are examined to establish selection criteria. This is then used for the optical design of the spectrograph in chapter 4, where the different parameters that characterize the spectrograph are computed and analysed through the parametric study. In addition, different techniques for aberration correction are investigated. Finally, in chapter 5, the selected design is implemented and optimised in ray-tracing software (CODE-V). The data provided by the software is then analysed.

1.1 The search for exoplanets

Recently, the discovery of exoplanets is a trending topic in space research. Statistically speaking, it can be hypothesized that there are billions of potentially habitable Earth-sized planets only in the Milky Way. Over the last two decades, NASA has confirmed the discovery of more than 4000 exoplanets and thousands of more planet candidates have been identified. [1] [2] Those are detected by various methods such as radial velocity, astrometry, direct imaging, transit, and

gravitational microlensing. [3]

Beyond driving the fields of planetary formation, evolution, structure and orbital mechanics in a new direction and helping scientists better understand how our solar system evolved, the discovery of exoplanets also raises philosophical discussions such as the well known Fermi paradox [1]. The ultimate goal is to understand the place of Earth and the Solar System in the universe, understanding the formation of planets and how unique is the Earth as a planetary host for biological activity.

1.1.1 In the past

For hundreds of years, humans have wondered if there were planets around other stars. Already in the sixteenth century, an Italian philosopher Giordano Bruno suggested that there were stars similar to ours, implying that they would have their own planets. [5] In the eighteenth century, Isaac Newton shared the same ideas. He mentioned in his famous Principia: *"...if the fixed stars are the centres of similar systems, they will all be constructed according to a similar design and subject to the dominion of One."*

1.1.2 Nowadays

The two first confirmed exoplanet discoveries were on 9 January 1992 by radio astronomers Aleksander Wolszczan and Dale Frail, followed by the third one in 1994. Although an exoplanet had already been detected in 1988 by the Canadian astronomers Bruce Campbell, G.A.H. Walker, and Stephenson Yang, it took until 2002 for it to be confirmed by improved detection techniques. However, the first discovery of a planet orbiting a Sun-like star was by Mayor and Queloz in 1995. They detected the exoplanet through its tiny gravitational pull on its star, 51 Pegasi and received the 2019 Nobel prize in physics. [6]

In February 2014, NASA's Kepler mission announced the discovery of 715 new planets orbiting 305 stars, revealing multiple-planet systems much like our solar system. [7] In August 2016, the European Southern Observatory (ESO) announced the discovery of Proxima Centauri b, a rocky planet in the habitable zone of Proxima Centauri, the closest star to Earth. [8] As of 31 March 2021, 4705 confirmed exoplanets are listed in the Extrasolar Planets Encyclopedia [1] with

[1]The Fermi paradox, named after Italian-American physicist Enrico Fermi, is the apparent contradiction between the lack of evidence for extraterrestrial civilizations and various high estimates for their probability. [4]

thousands of other "candidate" exoplanet detections that require further observations. [2] Since the first exoplanets were discovered in the early 1990s, the number of known exoplanets has doubled approximately every 27 months.

1.1.3 The science of exoplanet spectroscopy

The light emitted by a planet and/or the light transmitted through its atmosphere contains specific signatures directly related to its physical properties. The surface temperature, the chemical composition of the atmosphere and potentially the presence of biomarkers can be determined by spectral analysis of the incoming light. [9] However, detecting the light of an exoplanet is an extremely difficult task because of the high light intensity of its host star and/or the small angular separation from it. For instance, the angular separation of the Earth from the Sun seen from a distance of 10 pc. is approximately 100 milliarcsec. Also, the luminosity contrast between Earth and the Sun is about 10^{-10} in the visible and 10^{-7} in the mid-infrared. [10] Because of this, most exoplanets are detected indirectly, by measuring their effect on their host star.

1.1.4 Observation targets

In the context of this master thesis, observation targets are considered to be extrasolar planetary systems. In most cases, exoplanets are detected by radial velocity, transit, microlensing, and direct imaging methods. Moreover, the mass-period distribution plot in Fig. 1.1 shows that the radial velocity method is more biased towards the detection of massive planets with a larger period, whereas using the transit method, planets with a lower period are detected. It can also be seen that few exoplanets were detected by direct imaging (blue stars on the plot). This reinforces the motivation for projects like SCIFY to emerge to obtain larger samples of exoplanets.

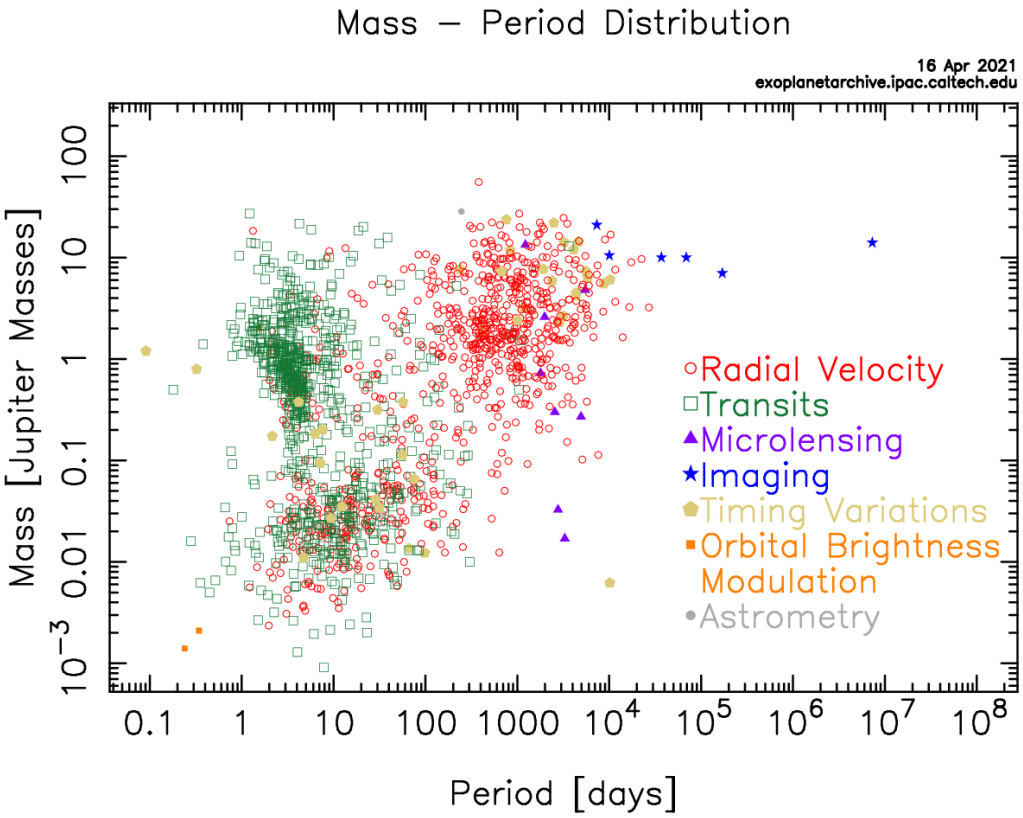

Figure 1.1: Mass-period distribution of detected exoplanets with the corresponding detection method. Credit: NASA Exoplanet Archive

The focus is on the observation of sun-like stars to locate and characterise rocky planets in the vicinity of the stars habitable zone. Despite its name, which can be misinterpreted, the habitable zone does not necessarily correspond to a region where life can exist or where humanity could live. It is defined as the region around the star where water can exist in liquid form on the surface of an orbiting planet. For example, if a planet is too close to its parent star, its surface might be too hot and water would have evaporated. Inversely, if the planet is located too far from the star, the water is frozen. Of course, this depends on many factors such as the size and age of the star but also the atmospheric condition of the planet (e.g. the presence of greenhouse gas).

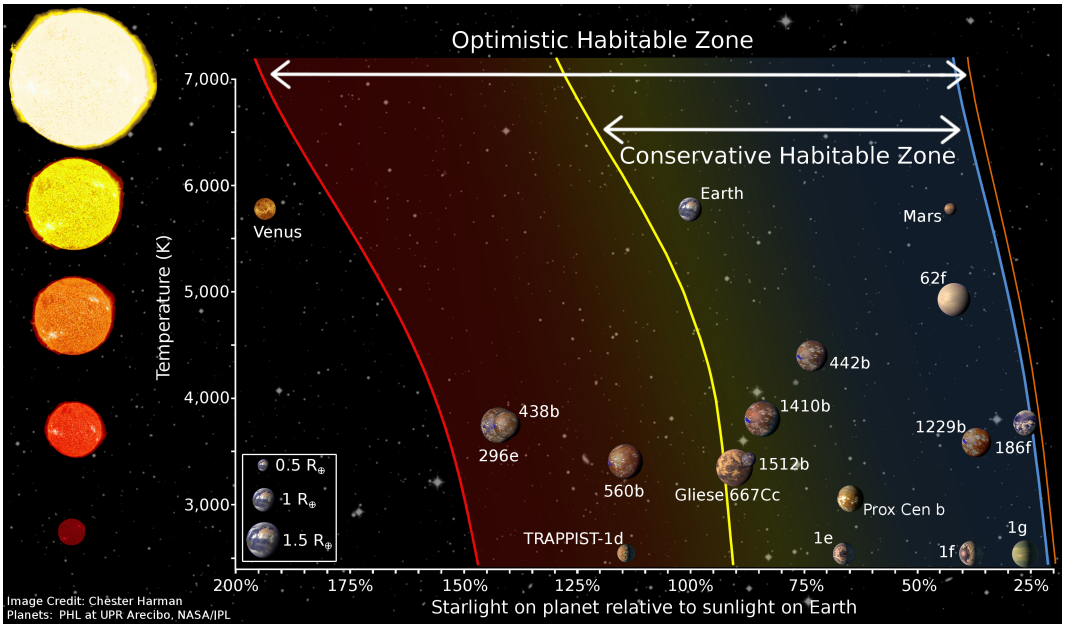

Figure 1.2: Diagram depicting the habitable zone boundaries around stars, and how the boundaries are affected by star type. By Chester Harman, CC BY-SA 4.0 [11]

The habitable zone tends to vary with time as the radiance and size of stars vary as they age. This leads to the definition of the Conservative Habitable Zone (CHZ) which is the region in which liquid water can exist over the entire main sequence lifetime of a star. This is represented in Fig. 1.2 for Venus, Mars, Earth, and significant exoplanets such as TRAPPIST-1d and Proxima Centauri b. This region is the most promising for the detection of biosignatures with the use of infrared spectroscopy. In fact, molecules such as H_2O absorb some of the light energy emitted or reflected by the planet at well-defined frequencies, mostly in the infrared. Therefore, the shape of the absorption spectrum gives direct information about the molecules present in the planet's atmosphere. This will be described in more detail in Sec. 2.2.2.

In most cases, indirect detection methods do not allow the characterisation of the planet's atmosphere. A solution to discriminate the planet's light from its parent star with sufficient angular resolution is nulling interferometry combined with high dispersion spectroscopy. By combining two or more signals, an interference pattern is created such that incoming signals cancel themselves out. This allows putting the parent star in a blind spot so that a weaker signal (e.g. planetary photons) are observed. The planetary light can then be injected into a spectrograph which separates the incoming light into a range of wavelengths. By analysing the transmission spectrum, the planet's atmosphere can be characterised. Although at the moment only a very small sample of terrestrial planets is available, the next-generation 30-40m ground-based Extremely Large Telescope (ELT) will be

able to observe smaller and more close-in exoplanets and potentially detect the first biosignatures.

1.2 Principle of nulling interferometry

As previously mentioned, the combination of nulling interferometry with high dispersion spectroscopy is logically the next step to improve sensitivity and broaden the science scope of direct imaging and spectroscopy. [12] In 1978, Bracewell proposed nulling interferometry as a solution to directly detect extrasolar planets. [13] The basic principle can be associated with the double-slit experiment[1]. Instead of observing a target with a single telescope, the light is collected by two or more telescopes separated from each other with distance b. This distance is called the baseline length and is directly related to the resolution that can be achieved. The schematic configuration of a Bracewell interferometer with the corresponding interference pattern is represented in Fig. 1.3.

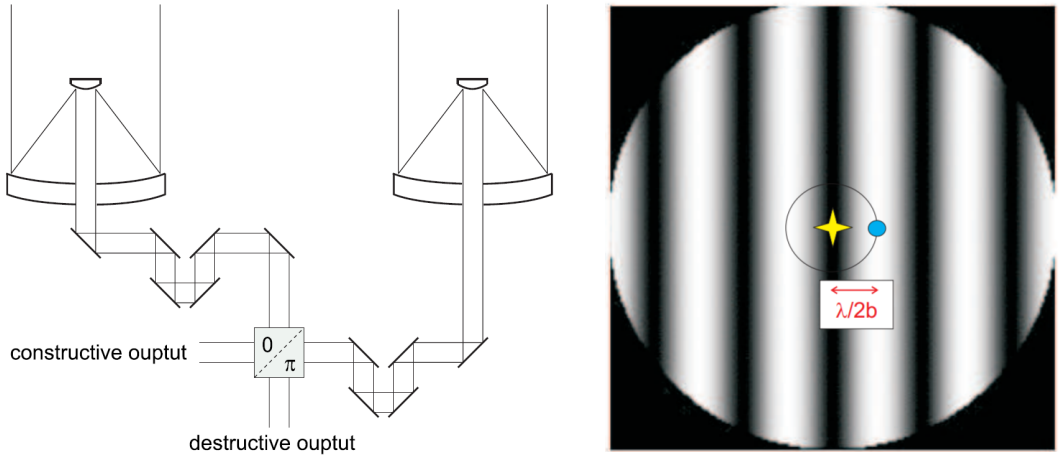

(a) (b)

Figure 1.3: **(a)** Schematic configuration of a Bracewell interferometer [14] with **(b)** the corresponding response on the sky. [10]

In the basic configuration, the two telescopes are in phase opposition. The phase difference of π is created by the achromatic phase shifter (APS), producing destructive interference on the line of sight (where the star is located). At an angular distance $\lambda/2b$ (λ is the wavelength and b the baseline length) from the line-of-sight, the interference is constructive and the flux from a planet located

[1] In modern physics, the double-slit experiment is a demonstration that light and matter can display characteristics of both classically defined waves and particles. By subsequently 'shooting' photons through two distinct slits, a diffraction pattern is observed indicating the wave behaviour of light.

at this position is fully transmitted. [10] This means that by adjusting the baseline length, the angular resolution of the interferometer can be tuned to match the observed target. By rotating the nuller in the plane perpendicular to the star direction, the planets move through the different peaks and nulls of the response while the star remains in a dark fringe. This creates a variation of the incoming flux with time from which the planet's flux can be extracted to inject in a spectrograph for characterisation.

1.3 The SCIFY project

Self-Calibrated Interferometry For exoplanet spectroscopY (SCIFY) is the name of a European Research Council (ERC) Consolidator project that started in October 2020 at KU Leuven. It is lead by Denis Defrère, Associate professor of Astronomy and Instrumentation at the department of astronomy of KU Leuven. SCIFY aims at building Hi-5 (High-contrast Interferometry up to 5 μm), a high-contrast thermal near-infrared imager for the Very Large Telescope Interferometer (VLTI) situated in Chile. Its main goal is to characterize young extra-solar planetary systems as well as exozodiacal dust around southern main-sequence stars and shed light on the formation and evolution of planets. In the long term, the SCIFY project will be a cornerstone in the roadmap leading to the characterisation of terrestrial exoplanets and the search for life beyond Earth. The project received funding from the European Research Council (ERC) under the European Union's Horizon 2020 research and innovation programme. [15]

1.3.1 Scientific objectives

The scientific objectives of the project are mainly contextualized around the detection and characterization of exoplanets to obtain a better understanding of their formation and evolution. The main goal is to build the first interferometric instrument with sufficient dynamic range and angular resolution to directly characterise exoplanets (Hi-5). This is achieved by leveraging the state-of-the-art infrastructure and long baselines of the VLTI.

The instrument operates in thermal near-infrared (L and M bands, $3 - 5\,\mu$m) in which water and methane have strong signatures. This will allow SCIFY to carry out several exoplanet programmes to study young Jupiter-like exoplanets at the most relevant angular separations (i.e., close to the snow line). Additionally, it will enable us to make progress in various scientific areas such as exozodiacal disks, extragalactic astrophysics and stellar physics. [16]

1.3.2 Scientific requirements

The scientific requirements are specified to achieve the scientific objectives described in the previous section. The design of the spectrograph takes these requirements as primary inputs to obtain the desired optical performances. In the case of SCIFY, the specifications focus on the observed spectral range and the achievable resolving power.

The required wavelength range extends over 500 nm and is located in the infrared L-band. The associated resolving power that must be achieved to distinctively characterize the water and methane signatures has been set to $R = 2000$. This resolving power criteria will be explained in more detail in Sec. 2.2.2. Also low and high resolution modes have been considered by the project ($R = 100$ and $R = 10000$ respectively). Each wavelength resolution element $\delta\lambda$ has to be discretized by 3 pixels. Also, the spot size for each wavelength has to be contained within a 2 by 2 pixel square. The scientific requirements are tabulated in Tab. 1.1.

Parameter	**Requirement**
Spectral range	$3.5 - 4.0\,\mu$m
Resolving power	2000
Sampling	3 pixels
Max spot size	2 pixels

Table 1.1: Scientific requirements on the near-infrared spectrograph.

Chapter 2

Overview of ground-based spectroscopy

2.1 State-of-the-art

The possibilities of current technologies are presented through a state-of-the-art of ground-based spectro-interferometric instruments. Moreover, it allows identifying the different facilities that could be compatible with the SCIFY project. Finally, the different spectral bands, resolution power, and their corresponding applications are presented.

2.1.1 Very Large Telescope Interferometer (VLTI)

The ESO Very Large Telescope Interferometer consists of the coherent combination of the four 8.2m diameter Unit Telescopes or the four 1.8m diameter Auxiliary Telescopes as illustrated in Fig.2.1. The interference created by the complex system of mirrors allows seeing details up to 25 times finer than with the individual telescopes. With this kind of precision, the VLTI provides the required milliarcsecond angular resolution at low and intermediate spectral resolution for deep ultraviolet (300 nm) to mid-infrared (24 μm) wavelengths. This is the equivalent of distinguishing the two headlights of a car at the distance of the Moon. [17]

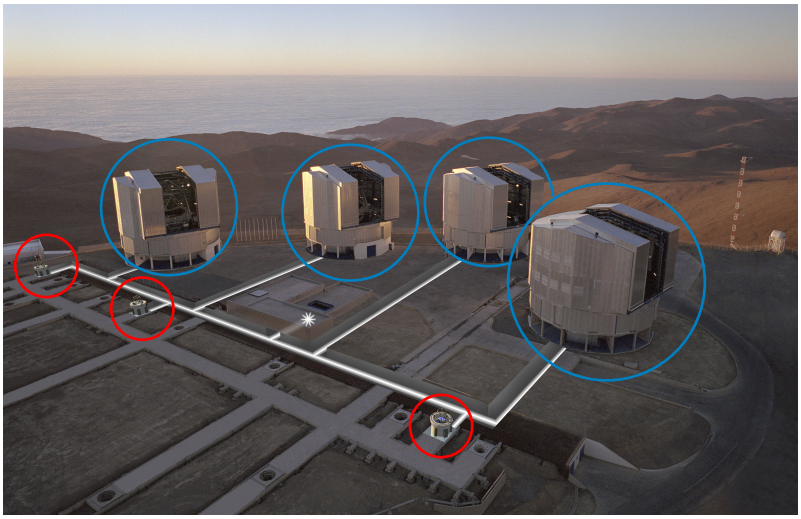

Figure 2.1: The four Unit Telescopes (encircled in blue) that form the VLTI together with 3 of the Auxiliary Telescopes (encircled in red). By ESO - ESO, CC BY 4.0. [18]

This ground-based facility is located in Cerro Paranal in the Atacama Desert of northern Chile and is considered the world's most advanced astronomical observatory. Its strategic position in the Southern hemisphere together with its unique characteristics makes the facility very attractive for scientific research and allows the VLTI instruments to carry out several high-impact exoplanet programmes to characterise the chemical composition of exoplanets.

MIDI - MID-infrared Interferometric instrument

MIDI was the mid-infrared instrument of the VLTI and operated in the N-band (8 to 13 μm). Its main goal was to disperse the light into a refractive spectrograph to analyse the dust composition and shape of the observation targets. The interference was created by combining the light coming from two of the VLTI telescopes (either from the Unit Telescopes or from the Auxiliary Telescopes). It consisted of two relatively low spectral resolution modes: R$\sim$30 (prism) and R$\sim$230 (grism). [19] Until recently, MIDI was the most productive interferometric instrument ever (surpassed by AMBER) with 159 publications starting from 2004. [20] However, it was decommissioned at the end of March 2015 to allow the preparation of the VLTI for the second-generation instruments.

AMBER - Astronomical Multi-BEam combineR

AMBER is one of the VLTI instruments that combines and disperses up to three beams of either the Unit Telescopes or the Auxiliary Telescopes. It operates in the near-infrared in the J, H and K bands (1.05 to 2.4 μm) and is organized into three

basic components.

First, the AMBER Warm Optics function is to correct for the atmospheric dispersion and polarisation effect and provide proper calibration. Spatial filtering is also made using single-mode fibres. Next, the refractive spectrograph performs spectral analysis at low (R∼30), moderate (R∼1500) and high (R∼12000) spectral resolutions by the means of a prism (for the low-resolution mode) and grisms (for the medium and high-resolution modes). It provides milli-arcsecond spatial resolution for compact astronomical sources in the considered wavelength domain. [21] Finally, the spectrograph is responsible for the formation of the images on a HAWAI I detector where only a 512x512 pixels quadrant is used. The general layout showing the position of the various optical modules is presented in Fig. 2.2

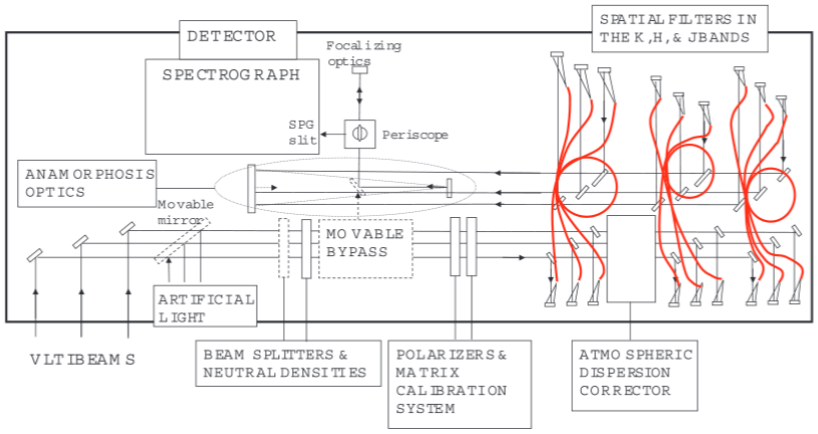

Figure 2.2: General layout of the AMBER instrument. (from Robbe-Dubois et al. 2007)

From 2006 to 2019, 164 refereed publication using data from AMBER have been posted in the ESO press release, surpassing its precursor MIDI. [20] Various scientific questions have been solved such as understanding how discs around Be-stars rotate, how dust forms around an erupting star and mapping of hot dust around active galactic nuclei. Today, AMBER is decommissioned as second-generation instruments (GRAVITY and MATISSE) have been developed for the VLTI.

GRAVITY

GRAVITY is one of the second-generation VLTI instrument first proposed in 2005. It is a 4-way beam combiner operating in the K-band (1.95 to 2.45 μm). K-band operation provides optimum resolution and sensitivity in highly dust extincted regions. This allows to map with spectro-differential astrometry the broad-line regions of active galactic nuclei, image circumstellar disks in young stellar objects and see their jets evolve in real-time, and detect and characterize exoplanets

especially around low mass stars and binaries. [22] The instrument includes two spectrometers in the considered wavelength range for the simultaneous detection of the interferometric signals of two astronomical sources (a faint science object and a brighter fringe tracking object). Three spectral resolution modes, R∼22, R∼500 and R∼4500 are available. Both prism/grism spectrometer have an almost identical design which is shown in Fig. 2.3

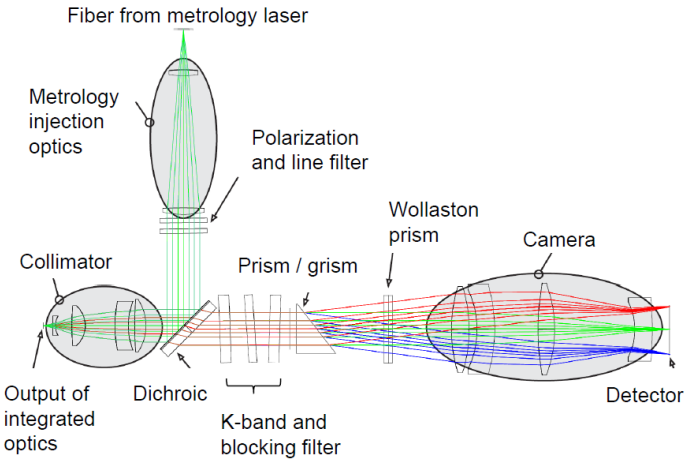

Figure 2.3: Optical design of the two spectrometers of GRAVITY for the example of the science spectrometer in high spectral resolution polarimetric configuration. [22]

MATISSE - Multi AperTure mid-Infrared SpectroScopic Experiment

MATISSE, together with GRAVITY and PIONIER, is a second-generation instrument of the VLTI. It combines the beams of four telescopes and operates in the L (3.0 to 4.0 μm), M (4.6 to 5.0 μm), and N (8.0 to 13.0 μm) bands. This offers unique capabilities as it is the first instrument to open the L- and M-bands to long-baseline infrared interferometry making it an extension of AMBER and will be complementary to METIS (the Mid-infrared European Extremely Large Telescope (E-ELT) instrument). Moreover, MATISSE provides an angular resolution of only several milli-arcsecond and spectral resolutions between R∼30 and R∼5000. It is composed of the Warm OPtics (WOP) where the L-, M- and N-bands are separated and two Cold Optics Benches (COB).

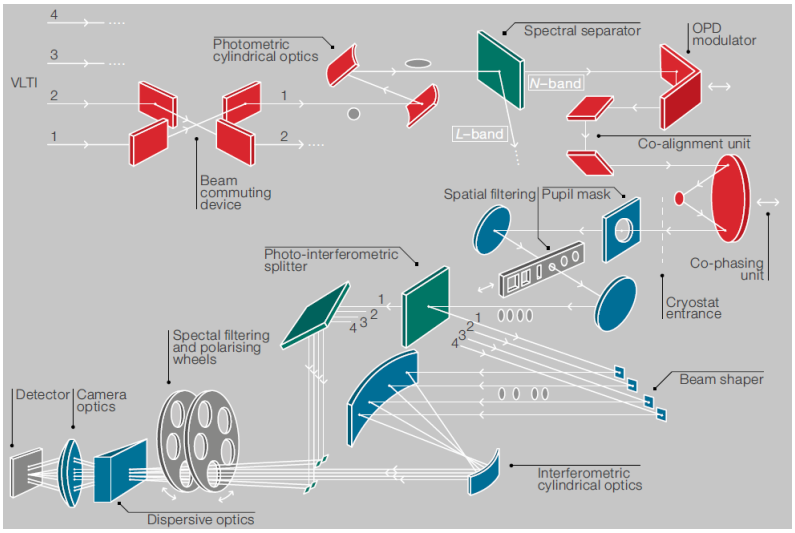

Figure 2.4: The schematic layout of the MATISSE instrument. The red parts represent optical elements located on the warm optics table at ambient temperature. The blue parts represent optical elements of the cold optics bench located in the cryostats. Only one COB with its elements and detector is shown. [23]

MATISSE saw its first light in March 2018 and will pursue the observations made by its predecessors MIDI and AMBER but with even more ambitious goals. The main scientific objectives consist of observing proto-planetary discs around progenitors to Solar-type stars and dust tori around active galactic nuclei. Additionally, the expected performance of this second-generation instrument will open up other fields of study. These range from the study of the birth of a massive star, the structure, dynamics and chemistry of evolved stars, the early evolution of Solar System minor bodies, to the characterization of hot Jupiters. [23]

2.1.2 Extremely Large Telescope (E-ELT)

Certainly, the most promising ground-based telescope for future astronomical observation is the Europe Extremely Large Telescope (E-ELT). It is the largest ground optical/near-infrared telescope project currently under construction in the world. The design consists of a 39.3m diameter primary mirror and a 4.1m secondary mirror (see Fig. 2.5). The primary mirror consists of 798 1.45m hexagonal segments. This makes the ELT significantly larger than the current largest telescopes, allowing it to gather 13 times more light. The ELT is planned to start operations in 2025.

Figure 2.5: Artist impression of the European Extremely Large Telescope (E-ELT) in its enclosure. Credit: ESO

The E-ELT will feature adaptive-optics assisted imaging and high-dispersion spectroscopic instruments to observe smaller and more close-in exoplanets. Moreover, it will have a resolution high enough to produce images 16 times sharper than the Hubble Space Telescope. This will allow us to obtain the first direct images of Earth-like planets, which have too faint signatures to be observed by current technologies. Additionally, the telescope will bring answers to other science topics such as fundamental physics, the formation and evolution of black holes, stars and galaxies as well as observing and understanding the earliest epoch of the Universe. [24]

METIS - Mid-infrared ELT Imager and Spectrograph

METIS is a mid-infrared imager and reflective spectrograph proposed for the European Extremely Large Telescope, currently undergoing a Phase A instrumentation study. It is the only proposed instrument to include imaging and spectroscopy in the thermal infrared spectrum from 2.9 to 14 μm (L, M and N bands with possible extension to Q band). The instrument consists of two main modes, each using adaptive optics correction. First, an 18 by 18 arcsecond FoV, diffraction-limited imager that features coronography at L- and N-band, long-slit spectroscopy with resolution power ranging from R$\sim$900 to R$\sim$5000 at L-, M- and N-bands, and polarimetry at N-band. The second mode consists of an integral field unit (IFU) feeding a high resolution (R$\sim$100 000) echelle grating spectrograph at the L- and M-bands (2.9 to 5.3 μm) with an FoV of about 0.4 $\times$ 1.5 arcseconds. [25]

The science drivers for METIS will be complementary to the James Webb Space Telescope (JWST) and the second-generation instrument MATISSE from the VLTI.

It covers a wide range of scientific topics, mostly focused on objects that are dust-obscured (hence the use of mid-infrared spectroscopy). Among other features, high dispersion spectroscopy will provide a deeper spectral analysis of younger planetary systems to assess their physical and chemical properties such as orbital parameters, internal structure, temperature profiles and atmospheric composition. Also, METIS will enable the determination of the composition and temperature gradients in the planetary formation disc, determine isotope ratios in cometary water and how it relates to that of terrestrial water. Furthermore, it will monitor the growth of supermassive black holes in galactic nuclei by analysing the size, geometry and dynamics of the circum-nuclear tori. [26]

Other instruments

Besides METIS, many other imagers and spectrographs undergo E-ELT Phase A instrumentation studies. Most of them are expected to operate in the near-infrared such as EAGLE, MICADO and SIMPLE but some of the proposed instruments also feature observation in the visible spectrum. A comparison of the characteristics of the instruments is presented in Fig. 2.6.

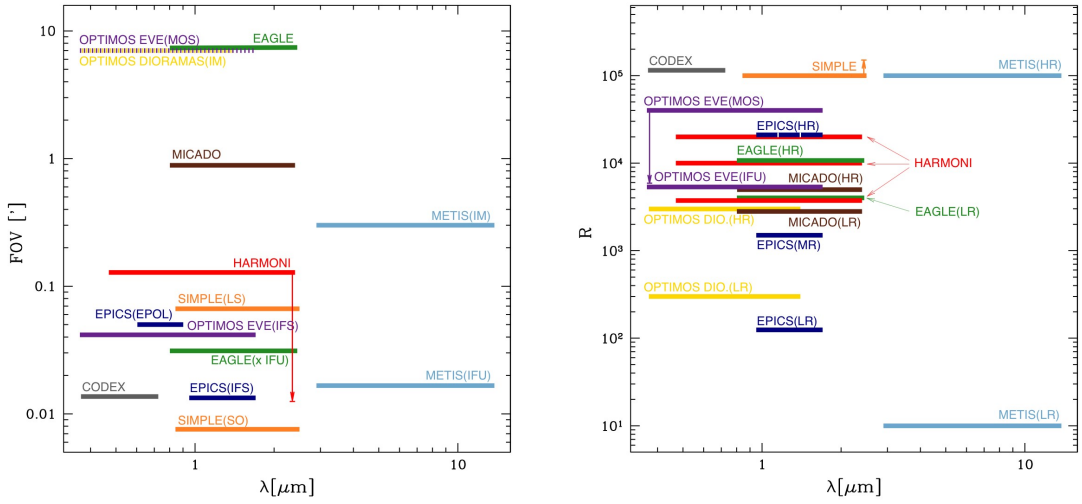

(a) (b)

Figure 2.6: Characteristics of the eight E-ELT proposed instruments currently under study. **(a)** Width of the FoV vs. wavelength coverage. **(b)** Spectral resolution vs. wavelength coverage. Credit: ESO

2.2 The importance of infrared spectroscopy

Over the years, experimental spectroscopy has proven to be a fundamental tool in the fields of physics, chemistry, and astronomy. As described in the previous sec-

tion, many applications of astronomical observation are associated with the use of a spectrometer. For the future, spectroscopy is expected to continue to expand as all the instruments proposed for the next-generation telescope E-ELT contain a spectrometer. More specifically, infrared spectroscopy allows the characterisation of extra-solar planetary systems as the specific signatures contained in the light emitted by a planet is directly related to its chemical composition.

2.2.1 Molecular absorption

When an electromagnetic signal interacts with matter, absorption, emission and scattering by atoms or molecules occur. This is due to the presence of covalent bonds in almost any organic or inorganic compound. A molecule composed of N atoms can be considered as $3N-6$ (or $3N-5$ for linear molecules) non-coupled linear oscillators named vibrational normal modes [27]. This is what is called the harmonic approximation. Using the harmonic oscillator and wave equations of quantum mechanics, the energy associated with the kth mode can be written as,

$$E_{v_k} = \left(\frac{1}{2} + v_k\right)\hbar\omega_k$$

where v_k is the vibrational quantum number ($v_k = 0, 1, 2, ...$) and ω_k is the vibrational frequency. Transitions in vibrational energy levels can be brought about by absorption of radiation, provided the energy of the radiation exactly matches the difference in energy levels between the vibrational quantum states of the molecule and provided the vibration causes a change in dipole moment. This can be expressed as,

$$\Delta E_k = \hbar\omega_k$$

This means that each chemical species is associated with the absorption of energy at well-defined frequencies of electromagnetic radiation. Usually, vibrational absorption occurs in the infrared region of the electromagnetic spectrum with wavelengths between 2.5 μm and 25 μm. Absorption bands in the near infrared (NIR) region (750 - 2500 nm) are weaker and arise from vibrational overtones and combination bands. [27] Combination bands occur when two molecular vibrations modes are excited simultaneously. When a molecule is excited from the ground vibrational state to a higher vibrational state and the vibrational quantum number v_k is greater than or equal to 2 then an overtone absorption results. The intensity of overtone bands reduces by one order of overtone for each successive overtone. So, the energy change can be expressed as,

- $\Delta E = n\hbar\omega_k \;\; n = 1, 2, 3, ...$ (overtone absorption)
- $\Delta E = m\hbar\omega_k + n\hbar\omega_l \;\; m, n = 1, 2, 3, ...$ (combination bands)

Those appear for non-harmonic potentials or in the presence of external perturbations.

2.2.2 Biosignatures

As soon as photons from an exoplanet can be distinguished from the photons of its parent star, a photometric and spectral analysis of the planet is feasible by the means of a spectrograph. By observing the absorption or transmittance spectrum, the physical and chemical properties of the planet and its atmosphere, such as their size, temperature and climate structure can be deduced. More importantly, the identification of some atmospheric molecules such as H_2O, CO_2, O_3, NH_3, and CH_4 could indicate the possibility for life to prosper on the planet. [15]

As molecules all have specific shapes and different chemical bonds (see Sec. 2.2.1), each species can be associated with a well-defined spectral signature. In the visible and near-infrared wavelength range, the detected flux from an Earth-like planet is reflected starlight while in the thermal infrared, the planet's thermal emission is observed. For example, the spectra of Earth in the infrared domain displays features of water vapour and molecular oxygen (mainly in the near-infrared). However, the reflected spectra of Venus and Mars display fewer features. This is where the mid-infrared proves to be useful.

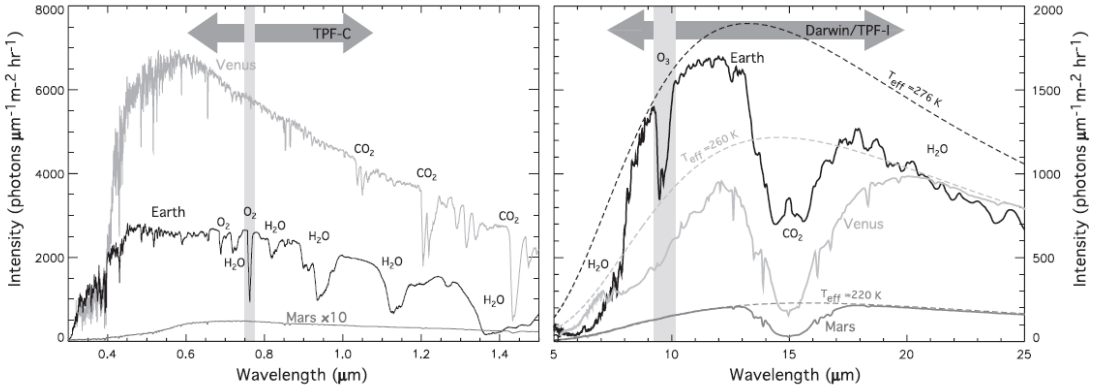

Figure 2.7: Spectra of Earth, Venus and Mars. **Left:** reflection spectra at $R \sim 100$. **Righ:** mid-IR thermal emission at the same resolution. Spectra presented here are model results, validated after comparisons with observation. [28]

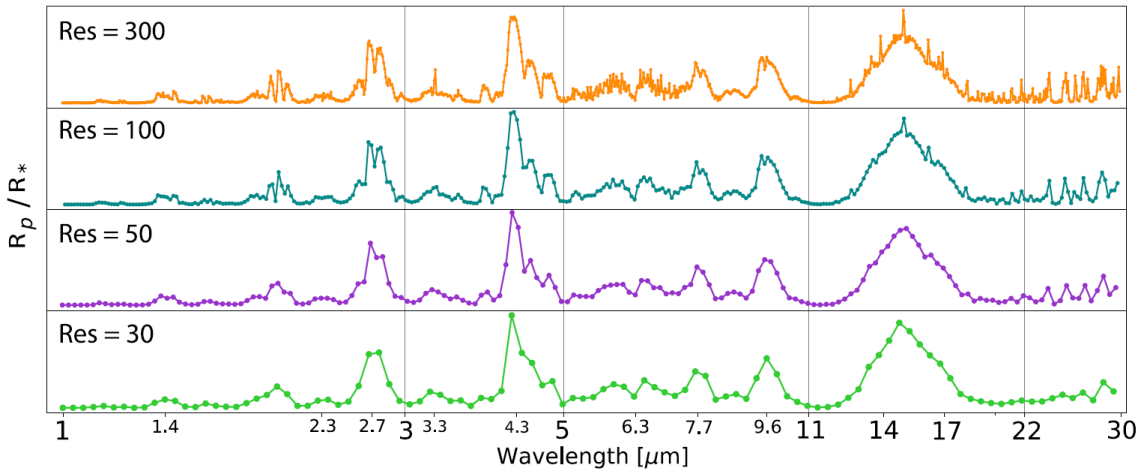

Figure 2.8: Influence of resolution on spectral features. The plots are synthetic transmission spectra of our Earth-like atmosphere model for different spectral resolutions ($R = 30$, 50, 100 and 300). [29]

As can be seen in Fig. 2.7, strong features of ozone, water vapour and CO_2 can be observed using low resolution (R$\sim$100) spectroscopy for the example of Venus, Mars and Earth. [28] On the other hand, CH_4 absorbs throughout the VIS-NIR-MIR with its strongest bands at 1.65, 2.4, 3.3, and $7 - 8\,\mu$m. However, at each of CH_4's strong bands, it overlaps with H_2O absorption, which makes uniquely detecting CH_4 problematic at low spectral resolution. [30] Increasing the spectral resolution reduces the degeneracy between spectral features of different molecules, hence the high resolving power requirement ($R = 2000$). Moreover, lower resolution results in the blending of features, causing a loss of information. This is represented in Fig. 2.8.

High-resolution infrared spectroscopy is expected to show promising results in the near future. Next-generation telescopes could potentially detect oxygen, methane and ozone on a distant replica of Earth. These compounds occur as a consequence of extended biomass production by oxygenic photosynthesis, potentially indicating the presence of life.

2.3 Considerations for ground based spectroscopy

2.3.1 Atmospheric window

In the previous section, the possibility to observe biosignatures such as water vapour and oxygen on distant planets was discussed. However, when observing extra-planetary objects from the ground, one should choose carefully which wavelength range is observed. As a matter of fact, water vapour, ozone and CO_2

are also present in Earth's own atmosphere and absorb part of the spectrum. The atmospheric window refers to a range of wavelengths over which there is relatively little absorption of radiation by atmospheric gases. At these intervals, light can propagate down to the ground without being absorbed. As depicted in Fig. 2.9, two major windows are present in the visible window, from $\sim$ 0.3 to $\sim$ 0.9 μm and the infrared window, from $\sim$ 8 to $\sim$ 13 μm as well as in the radio band. These wavelength ranges are thus crucial for ground-based observation. For the other wavelength range, other techniques are required such as space-based telescopes.

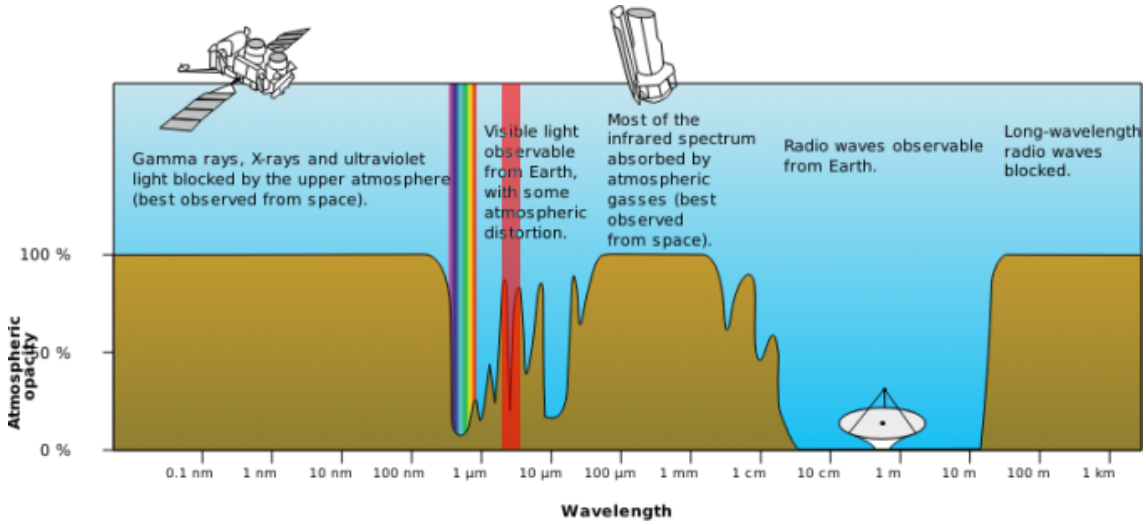

Figure 2.9: Atmospheric Electromagnetic Opacity of Earth. The considered wavelength range for the SCIFY project (3.5 – 4.0 μm) is highlighted in red. Copyright: NASA

In the infrared, most of the light from the Universe coming to Earth is absorbed by water vapour and carbon dioxide in the atmosphere. However, there are few minor infrared windows where light can make it through to a ground-based telescope. Secondly, the atmosphere and Earth itself have a non-zero temperature and consequently emit thermal radiation. In many applications, the infrared radiation of the Earth is stronger than the object in space being observed. As a consequence, only wavelengths that can pass through the atmosphere and at which the atmosphere is dim can provide meaningful data. The infrared window of Earth is illustrated in more detail in Fig. 2.10.

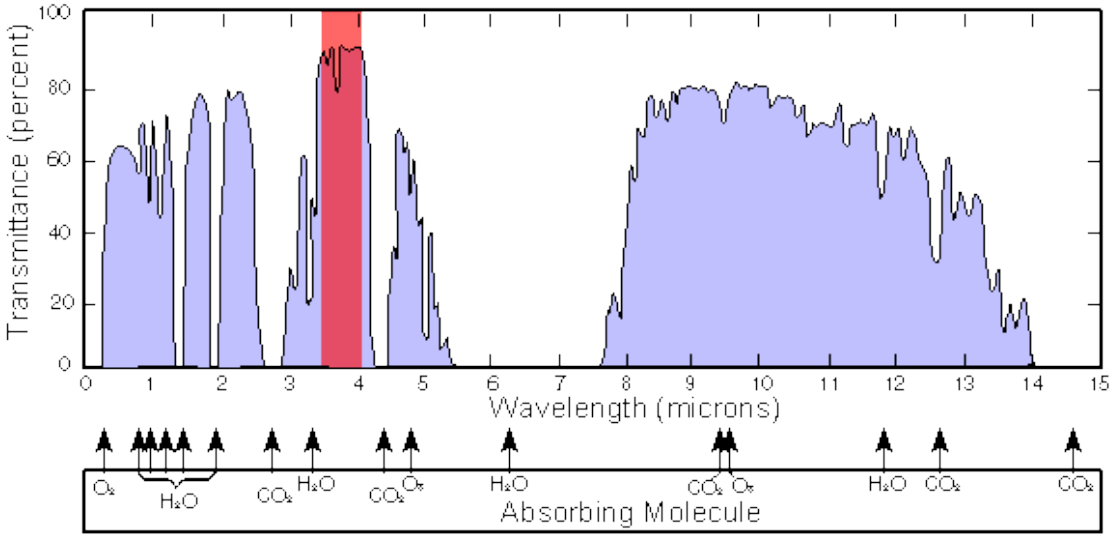

Figure 2.10: Atmospheric transmittance spectrum of Earth. The considered wavelength range for the SCIFY project ($3.5 - 4.0\,\mu$m) is highlighted in red. Public Domain.

From fig. 2.10, a few infrared windows can be seen. Ideally, those have both high sky transparency and low sky emission and are located mainly below $4\,\mu$m. The main infrared windows are tabulated in Tab. 2.1.

Wavelength Range	**Band**	**Sky Transparency**	**Sky Brightness**
$1.1 - 1.4\,\mu$m	J	high	low at night
$1.5 - 1.8\,\mu$m	H	high	very low
$2.0 - 2.4\,\mu$m	K	high	very low
$3.0 - 4.0\,\mu$m	L	$3.0 - 3.5\,\mu$m: medium $3.5 - 4.0\,\mu$m: high	low
$4.6 - 5.0\,\mu$m	M	low	high
$7.5 - 14.5\,\mu$m	N	$8 - 9\,\mu$m: medium $10 - 12\,\mu$m: medium others: low	very high

Table 2.1: Infrared windows in Earth's atmosphere with their corresponding spectral band notation as well as qualitative description of the sky transparency and brightness.

2.3.2 Noise sources

In the absence of degrading effects by the atmosphere, the resolution achieved by a telescope is determined by the diffraction of light. The image of a point-like astronomical source formed on the detector is then represented by the Point Spread Function (PSF). In practice, for ground-based observatories, the light must first pass through the atmosphere which causes a degradation of the image quality. This is due to several natural or artificial processes such as sky brightness, light scattering, molecular absorption, thermal emission or even the presence of clouds and man-made light pollution. These processes play a huge role to qualify a site for frontline ground-based astronomy.

Sky brightness

The night-sky brightness in the optical and near-infrared is one of the only parameters that is possible to keep at its natural level by preventing light pollution in the vicinity of the observatory. [31] During the daytime, the Sun is the dominant source of light, making observations impossible. But even at night time, natural atmospheric emission (airglow), indirect scattering of sunlight, starlight and light pollution induce noise for observation of faint, distant objects.

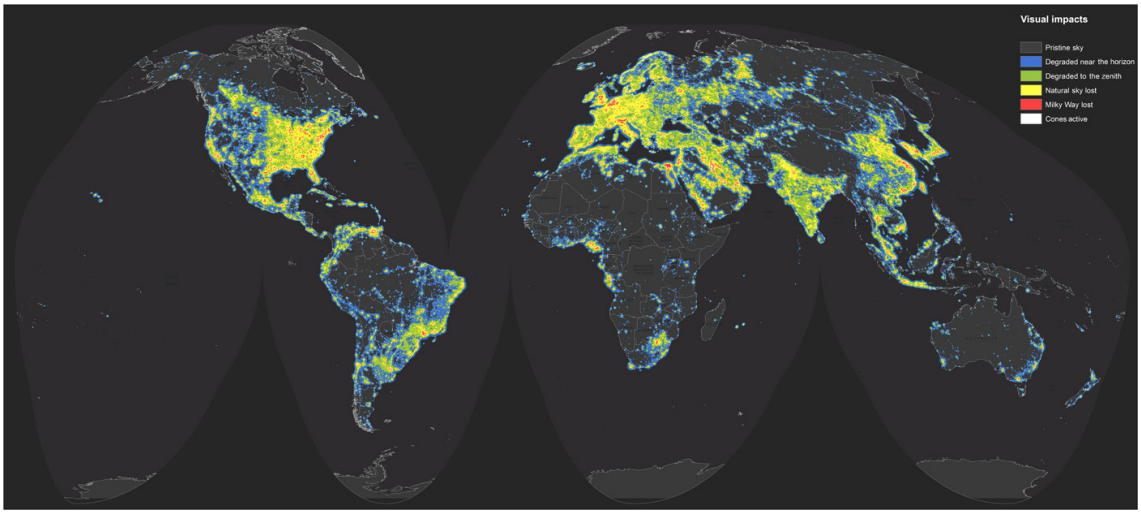

Figure 2.11: World map of artificial sky brightness as a ratio to the natural sky brightness. The color scale represents the intensity of artificial light pollution in the corresponding region from black (= pristine sky) to red (= heavily polluted). The visual impact corresponding to each color is described in the top right corner. [32]

Figure 2.11 displays the artificial sky brightness as a ratio to the natural sky brightness. The importance of the location of the observation site is strongly emphasised. Moreover, atmospheric emission also plays an important role in

sky background noise. This is observed mainly in the visible wavelength range where Sodium and Mercury emissions are the main sources of light pollution (see Fig.2.12a). [33] For the sky surface brightness in the near infrared, a strong air-mass dependency in the J and H bands, and a mild one in the K band was assessed by Sanchez et al. at the Calar Alto observatory (see Fig. 2.12b). [34]

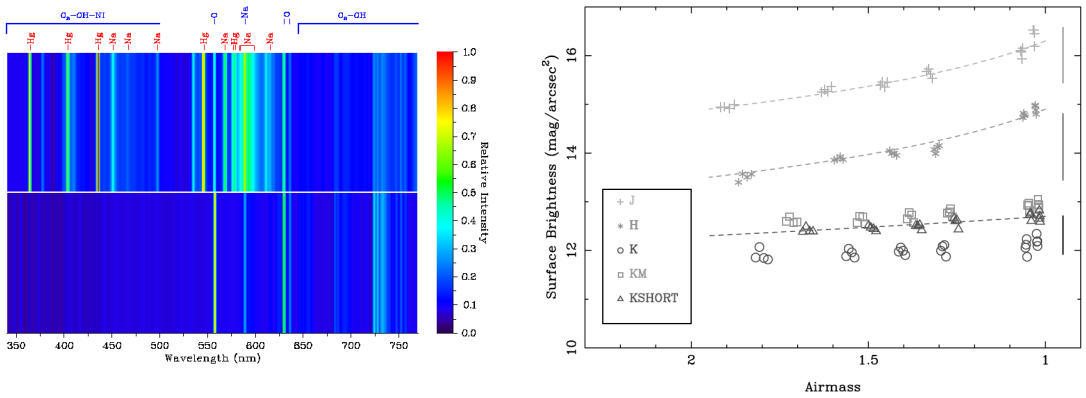

(a) (b)

Figure 2.12: **(a)** Comparison between a night sky spectrum taken at Cerro Paranal-Chile during dark time (lower panel) and one taken in Asiago-Italy (upper panel). [31] **(b)** Variation of near-infrared surface sky brightness in different bands as a function of the air mass for the night of the 31st January 2008. [34]

Atmospheric scattering

Atmospheric scattering is an interaction process between light and particles in the atmosphere. Light scattering is associated with a change in spatial distribution or diffusion of electromagnetic energy rather than the transformation of energy. There are three main types of scattering that impact solar radiation: Rayleigh scattering, Mie scattering, and non-selective scattering. The type and amount of scattering depend on the size of the particles present in the atmosphere as well as on the wavelength of the incoming light. Both dependencies can be described by the size parameter $x = 2\pi a/\lambda$ where a is the particle radius. This is represented in Fig. 2.13

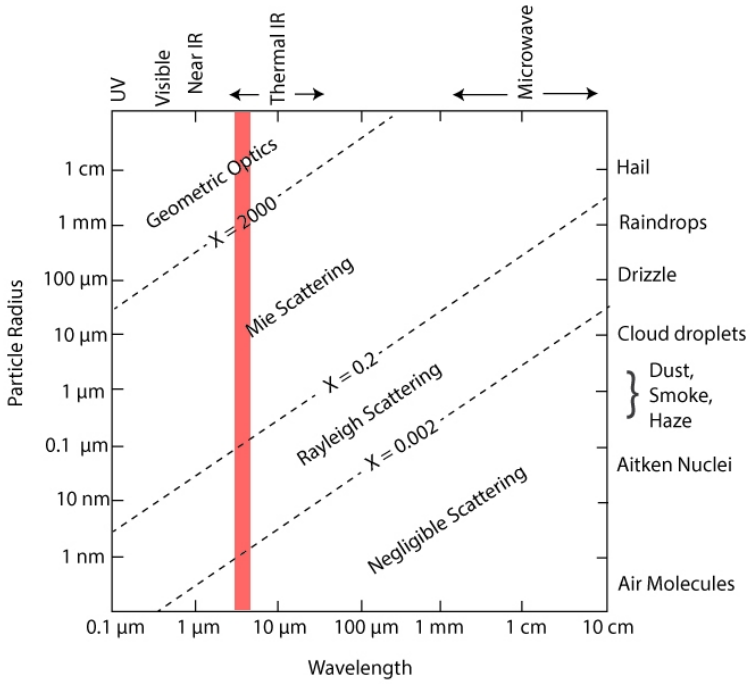

Figure 2.13: Graph of size parameter x and type of scattering as a function of radiation wavelength and particle radius. Radiation and particle types are shown at the right and top, respectively. The considered wavelength range for the SCIFY project ($3.5 - 4.0\,\mu$m) is highlighted in red. Credit: W. Brune (after Grant Petty). [35]

Rayleigh Scattering is associated with the scattering caused by particles that are smaller in size than the wavelength of radiation in contact with them. The amount of scattering is therefore wavelength dependent. In fact, shorter wavelengths are more readily scattered than longer wavelength which explains the blue colour of the sky. As in the visible spectrum, blue has a shorter wavelength than red, it will be more scattered by small atmospheric particles or molecules such as NO_2 and O_2. [36] The amount of scattering is characterized by the scattering cross-section σ. As its name suggests, it represents an effective area for collision. The higher this cross-section, the more the light will be scattered. For the Rayleigh approximation, the cross-section can be written as the analytic function, [37]

$$\sigma_{\text{Ray}} = \frac{8\pi}{3}\left(\frac{2\pi n_{med}}{\lambda}\right)^4 a^6 \left(\frac{m^2-1}{m^2+2}\right)^2 \tag{2.1}$$

where λ is the vacuum wavelength, a is the particle radius and $m = n_{\text{sph}}/n_{\text{med}}$ is the ratio of the refractive index of the particle to that of the surrounding medium. The expression clearly emphasises the wavelength dependence of Rayleigh scattering as $\sigma_{\text{Ray}} \sim \lambda^{-4}$. This type of scattering is thus mainly dominant in the UV.

Mie scattering, on the other hand, can be associated with the behaviour of light interacting with any kind of particles. [38] Nevertheless, it is usually describing an interaction between light that has wavelengths of similar size to the atmospheric particles, mainly larger ones such as pollen, dust, smoke and water droplets. [39] It is a wavelength-dependent process that explains the diffusion of light in the infrared region. It is also responsible, together with non-selective scatter, for the white appearance of the clouds.

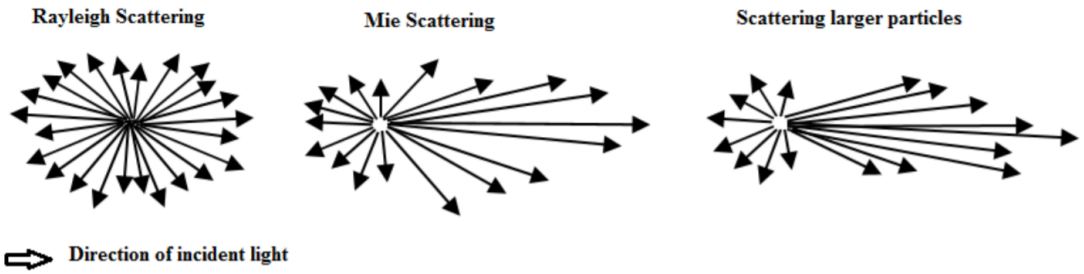

Figure 2.14: Patterns of Rayleigh, Mie and Non-selective scattering. [40]

Finally, **non-selective scatter** occurs when the size of the particle is significantly larger than the wavelength of the incoming light. It mainly occurs in the lower portion of the atmosphere where larger particles such as water droplets are located. Unlike the other two described scattering process, it is not wavelength-dependent (hence its name) and is the primary cause of haze and the white appearance of fog and clouds. As all wavelength are scattered by the larger water droplets present in clouds, most of the energy is blocked preventing high-quality observations. Therefore, the weather condition plays an important role in astronomical observations. The difference in scattering patterns for the 3 types is shown in Fig. 2.14.

Molecular absorption

The atmospheric window is mainly determined by the molecular absorption processes that take place in the atmosphere. The absorption of the incoming electromagnetic energy is associated with a molecular transition. Those transitions can be electronic (by ionization), vibrational or rotational. The energy levels involved for the different types of transition are generally well separated so that, [27]

$$E_{\text{el}} > E_{\text{vib}} > E_{\text{rot}}$$

This means that electronic transitions are mainly occurring in the UV. They are associated with the ionisation and dissociation processes of oxygen and ozone as depicted in Fig. 2.15

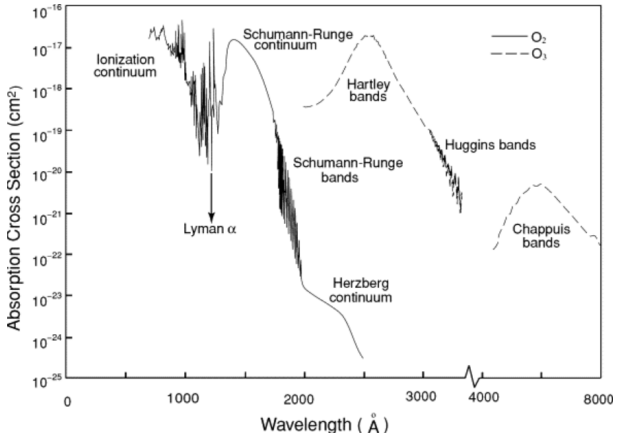

Figure 2.15: Absorption cross section of ozone and molecular oxygen in the ultraviolet spectral region [41].

As described in Sec. 2.2.1, vibrational features occur in the mid and near-infrared whereas rotational features typically occur in the far infrared. [42]

Thermal emission

Any matter that has a temperature greater than absolute zero emits electromagnetic waves (= thermal radiation). In the case of the Earth and its atmosphere, it can be approximated as a black body. The spectral radiance of a black-body is described by Planck's law for a given frequency ν at absolute temperature T,

$$B(\nu, T) = \frac{2h\nu^3}{c^2} \frac{1}{e^{\frac{h\nu}{k_B T}} - 1} \tag{2.2}$$

where k_B is the Boltzmann constant, h is the Planck constant and c is the speed of light. For the Earth we have $T \sim 300$K giving a peak emission at $10\,\mu$m. It emits thus mostly in the thermal infrared.

Additionally, an important source of thermal noise is caused by the instruments. As a matter of fact, the bulk of the atmosphere is generally $\sim$ 20K colder than the telescope mirrors. Then, for wavelengths less than $\sim$ 13K, instrumental noise (telescope mirrors, warm optics, spectrograph,...) is dominant. The only solution to this issue is cooling the entire system down to very low temperatures. Typically, spectrographs operating in the NIR ($1 - 5\,\mu$m) have their main components cooled to $\sim$ 70K, whilst the detectors are held at $\sim$ 25K to $\sim$ 4K or less and the whole instrument is enclosed in a vacuum chamber. [43]

Atmospheric dispersion

Another difficulty that has to be considered in ground-based astronomy is atmospheric dispersion. Atmospheric refraction in the Earth's atmosphere changes the observed position of a star from its true position due to the variation in air density as a function of altitude. In fact, the index of refraction increases as the density of air increases causing the velocity of light to decrease. According to Snell's law, this is accompanied by a change in angle of incidence of the incoming light, modifying the perceived position of the observed object from the ground.

Moreover, the variation of the refraction index of air with the wavelength induces chromatism. For standard temperature and pressure, Cauchy's formula gives the refractive index of the atmosphere, [43]

$$\mu = 1.000287566 + \frac{1.3412 \times 10^{-18}}{\lambda^2} + \frac{3.777 \times 10^{-32}}{\lambda^4} \tag{2.3}$$

This can strongly influence spectroscopic observations at large air masses as part of the flux can be lost when the light passes through slits or fibres. [44] In the past, most investigators have avoided this problem by orienting their spectrograph slit to be aligned with the direction of the dispersion. [45] Also, Donnelly has discussed the effect of atmospheric refraction on fibre-fed spectroscopic instruments. [46] Alternatively, an Atmospheric Dispersion Corrector (ADC) may be used. It is a system made of two rotating prisms designed for a maximum air-mass correction when aligned with their dispersion directions being parallel and in opposition to that of the atmosphere.

2.4 Fibre optics in spectroscopy

The use of fibre optics to transmit starlight from the focal plane of the telescope to a spectrograph was first introduced by Narinder Kapany in the late fifties. He proposed using fibres as a way of reformatting a stellar image into a linear slit, to act as an image slicer. [47] However, the first experiments in astronomical spectroscopy using a fibre-fed spectrograph is attributed to Hubbard, Angel and Gresham in 1978. [48] Over time, with the availability of fused silica technologies, the use of fibres in astronomy became more practicable. [49]

2.4.1 Basic principles of fibre optics

A fibre optic cable is a waveguide that transmits light along its axis. Usually, optical fibres are composed of a core and a cladding that surrounds them. To understand how it functions, the concept of Total Internal Reflection (TIR) has to be

introduced. According to Snell's law, the relation between the angle of incidence (θ_i) and angle of refraction (θ_r) of a light ray passing through a boundary between two different media is given by,

$$n_1 \sin\theta_i = n_2 \sin\theta_r$$
$$\Leftrightarrow \sin\theta_r = \frac{n_1}{n_2} \sin\theta_i$$

where n_1 and n_2 are the refraction index of both media. This means that an increase of the incidence angle is accompanied by an increase of the reflectance angle if $n_1 > n_2$. At some point, the sine of the angle of refraction reaches a value bigger than one and the light is completely reflected at the boundary of the interface (= total internal reflection). The largest incidence angle for which there is still refraction or for which $\theta_r = 90°$ is the critical angle θ_c,

$$\theta_c = \arcsin\left(\frac{n_2}{n_1}\right) \tag{2.4}$$

In the case of fibre optics, this critical angle corresponds to the maximum angle with the axis of the optical fibre at which the light entering propagates through the fibre by total internal reflections at the core-cladding interfaces. Because of the circular shape of the fibres, this forms an acceptance cone (see Fig. 2.16).

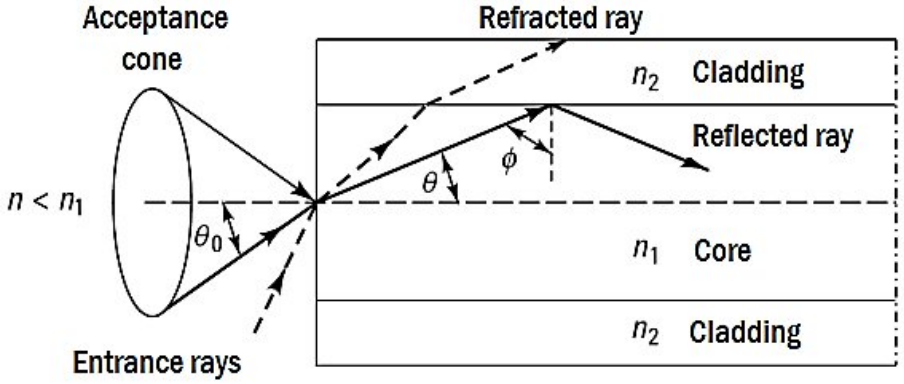

Figure 2.16: Acceptance cone in an optical fiber with uniform core index of refraction. [50]

for angles of incidence at the core-cladding interface ϕ greater than the critical angle, the light will travel through the fibre. From Fig. 2.16, we have,

$$\theta_r = 90° - \phi$$

Also, the incidence angle θ_i at the air-core interface is equal to the acceptance angle θ_a if $\phi = \theta_c$. By applying Snell's law, this gives,

$$n_{\text{air}} \sin \theta_a = n_{\text{core}} \sin 90° - \theta_c \tag{2.5}$$

After some basic trigonometry, injecting Eq. 2.4 into 2.5 and considering $n_{\text{air}} = 1$,

$$\begin{aligned} \sin \theta_a &= n_{\text{core}} \sqrt{1 - \frac{n_{\text{cladding}}^2}{n_{\text{core}}^2}} \\ \Leftrightarrow \sin \theta_a &= n_{\text{core}} \sqrt{\frac{n_{\text{core}}^2 - n_{\text{cladding}}^2}{n_{\text{core}}^2}} \\ \Leftrightarrow \theta_a &= \sin^{-1} \sqrt{n_{\text{core}}^2 - n_{\text{cladding}}^2} \end{aligned}$$

The acceptance angle is thus determined by the difference in refractive index between the core and the cladding. Usually, the core and cladding are made out of similar glass. The difference in refractive index is made by doping the core glass with index-raising materials such as germania (GeO_2) and alumina (Al_2O_3). Inversely, the index of the cladding may be lowered by index-lowering agents such as boron oxide (B_2O_3). [51]

2.4.2 Single mode fibres

In the context of this study, the spectrograph is fed by single-mode fibres realigned to simulate a linear slit. First of all, the general concept of optical fibre modes has to be understood. As a light flux is fundamentally an electromagnetic wave, it can be mathematically described by Maxwell's equations. These describe the propagation of the energy through a medium. A mode is an allowed solution to Maxwell's equations or a path that light rays can follow when travelling through a fibre cable. The number of modes that the fibre provides is depending on its size, design and properties (e.g refractive index). [52]

Optical fibres are generally classified into two categories, single-mode fibres (SMF) and multimode fibres (MMF), depending on whether the fibre carries one mode or more modes respectively. [53] The number of modes supported by a fibre cable can be calculated from the V-number or normalized frequency defined as, [52]

$$V = \frac{2\pi d}{\lambda}(\text{NA}) \tag{2.6}$$

where d is the core diameter, λ the wavelength of the propagated light and NA the numerical aperture of the fibre. For a step-index fibre cable, the number of

modes (N) has a V^2 dependency ($N \sim V^2$). The number of modes propagated through the fibre cable is therefore directly related to the fibre core radius. In fact, single-mode fibres usually have a relatively small core and can guide only the fundamental mode (i.e the transverse mode). SMFs are characterized by the fact that the electric profile is constant throughout the fibre. This means that the electric field at the output of the fibre is independent of the electric profile at the input. Inversely, multi-mode fibres usually have a larger core radius and/or a larger index difference between core and cladding. [53]

2.4.3 Advantages of optical fibres

Mechanical stability

The use of fibre optics has opened many new opportunities. For example, in modern spectroscopy, fibre optic cables enable to easily control and confine the optical signals flowing from source to sample and onto the detector. The main advantage of this technology is to decouple the instrument from the telescope. The design constraints like stiffness, weight and volume are then highly relaxed. Moreover, one of the most important sources of error in a spectrograph attached to telescopes is the shift of the spectrum on the detector due to mechanical flexures during observations. The use of fibre optics allows higher spectral stability as the assembly is mechanically more stable. Additionally, decoupling the instrument from the telescope allows placing the spectrograph in a vacuum chamber, increasing the stability even further. The High Accuracy Radial velocity Planet Searcher (HARPS) at the ESO La Silla 3.6m telescope is an example of application of this. In fact, this fibre-fed high-resolution echelle spectrograph is optimised for mechanical stability, providing measurements of radial velocities with the highest accuracy currently available. [54]

Multi-Object Spectroscopy

Secondly, fibres may allow simultaneous observations of many objects with only one spectrograph. The basic principle of Multi-Object Spectroscopy (MOS) consists of aligning several fibres and place them in front of the spectrograph slit. Each fibre can be associated with a different light source at the telescope focal plane. The detector can therefore record the spectra from each fibre. The first instrument for multi-object spectroscopy was the MEDUSA spectrograph, implemented by John Hill and his colleagues. [49] The technique consisted of placing an aperture plate in the telescope focal plane with holes drilled at the location of the observed objects. Later, more advanced technologies were used where the fibres are positioned automatically for each field. A more recent example is the Fibre Large Array Multi-Element Spectrograph (FLAMES), an intermediate

and high-resolution spectrograph of the VLT. It feeds two different spectrographs covering the whole visual range. GIRAFFE, one of the two spectrographs, allows observation of up to 130 targets at the time with intermediate or high resolution (from $R \sim 5000$ to $R \sim 30000$). [55]

Integral field Spectroscopy

Another application of optical fibres is integral field spectroscopy. Instead of placing them on individual objects, the fibres are packed into a bundle in front of the image of an extended object such as a galaxy. Then, the output fibre ends are arranged along the slit of the spectrograph so that multiple spectra are obtained, each corresponding to a portion of the observed object. Due to the circular shape of the fibres, part of the light is lost in the interstitial space between the fibres. This is solved by placing a square microlens array, that acts very similar to the insects' composite eyes. This is represented in Fig. 2.17. An example of such a system is the VIMOS Integral Field Unit (IFU) instrument in Paranal Observatory. It is made of 6400 (80x80) fibres, coupled to microlenses. [56]

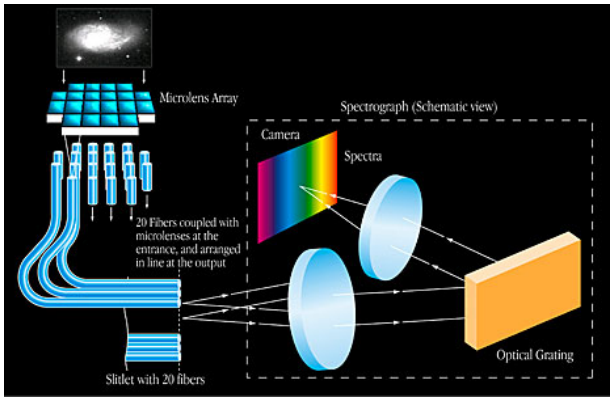

Figure 2.17: An illustration of how the integral field units function. The fibres are coupled with microlenses at the entrance and arranged in line at the output to form the spectrograph's input slit. Credit: ESO

Higher spectral resolution

Next to these applications, the use of fibre optics has many other advantages. Usually, higher spectral resolution can be obtained. As a matter of fact, the resolving power of a spectrograph is slightly higher for a circular aperture than for a slit with a width equivalent to the diameter of the fibre, at the expense of light flux reduction. Moreover, by separating a single thick fibre into a bundle of fibres with a smaller diameter, higher resolving power is obtained as the equivalent slit width is smaller. [57]

2.4.4 Limitations of fibre optics

Although fibre optics has many advantages, the properties of the fibres themselves are accompanied by undesirable effects such as transmission losses, focal ratio degradation (FRD) and image scrambling. When designing a fibre-fed spectrograph, those properties have to be analysed with care.

Focal Ratio Degradation (FRD)

The most dominant property of optical fibres that causes efficiency losses is the focal ratio degradation. It is characterized by a reduction of the focal length, increasing the f-number. This is caused by scattering effects within the fibre, which propagates the light to angles larger than the critical angle. Moreover, it will launch light into the extreme modes that result in a large exit angle. [58] In either case, the light is lost to the spectrograph. This is the result of several different factors, such as the presence of micro- and/or macro-bends and other sources of stresses within the core of the fibre. Generally, it is caused by manufacturing issues such as how good the polished end is, and how well the diameter was controlled in the fibre-drawing process. [59] A representation of such disruptions and their impact on the core and clad interface is shown in Fig. 2.18.

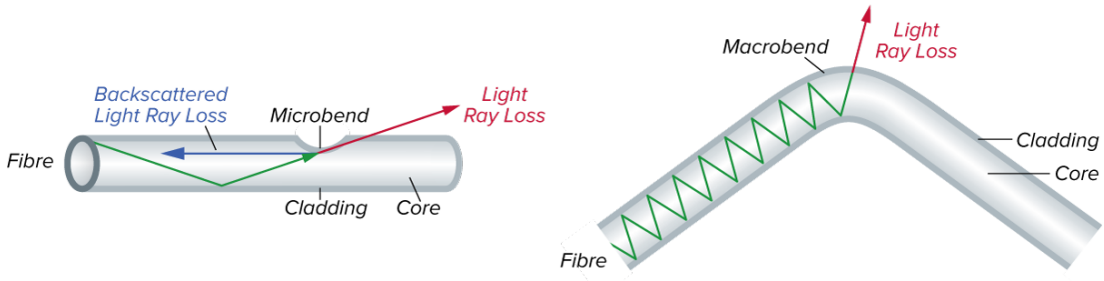

Figure 2.18: Representation of the impact of micro and macro bends on the internal reflection of fibres. [60]

The increase in focal ratio leads to the light exiting the fibre in a cone with an angular extent corresponding to a smaller focal length than the light illuminating the input end of the fibre. In a fibre-fed spectrograph, this causes a decrease in the resolving power and/or throughput efficiency. [59]

As illustrated in Fig. 2.19, FRD is always a loss when considering the astronomical spectroscopic application. As a matter of fact, a well-designed spectrometer has a collimator focal ratio equal to that of the telescope when using a circular aperture equal to the core diameter of a fibre. On the other hand, due to FRD, the use of fibres causes the output focal ratio to always be faster than the input number. The light loss induced by this can be recovered by increasing the collimator diameter.

However, this is associated with an enlargement of the grating and all successive optics. [61]

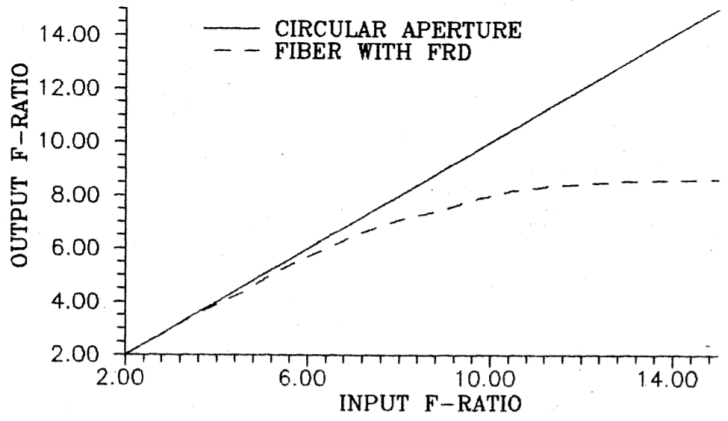

Figure 2.19: The Focal Ratio Degradation (FRD) of a typical fibre, compared to a circular aperture of the same diameter as the core of the fibre.

Scrambling

One other significant characteristic of fibres is their ability to scramble the input image. Two different types of scrambling mechanism take place in cylindrical fibres; azimuthal and radial scrambling. Azimuthal scramble refers to the capacity of fibres to distribute the input light's angular information into an output ring of light as depicted in Fig. 2.20. Radial scrambling relates to the effect of any lateral shifts from the centre position on the light pattern at the end side of the fibre.

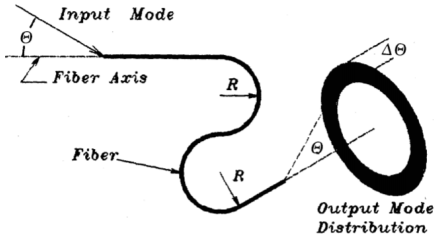

Figure 2.20: Azimuthal dispersion or scrambling of fibres. [61]

As determined by Heacox [62] and experimentally demonstrated by Ramsey [61], azimuthal image scrambling of the near-field output image is almost always complete. Radial scrambling, on the other hand, may not be complete. As shown in Fig. 2.21, the radial scrambling performance strongly depends on the input focal ratio. As a matter of fact, the fraction of light in the output image that retains the radial position of the input increases as the fibre is fed with faster input focal ratios. In the context of a spectrograph for which image stability is crucial, a

trade-off between low focal ratio degradation and the level of image scrambling is therefore necessary.

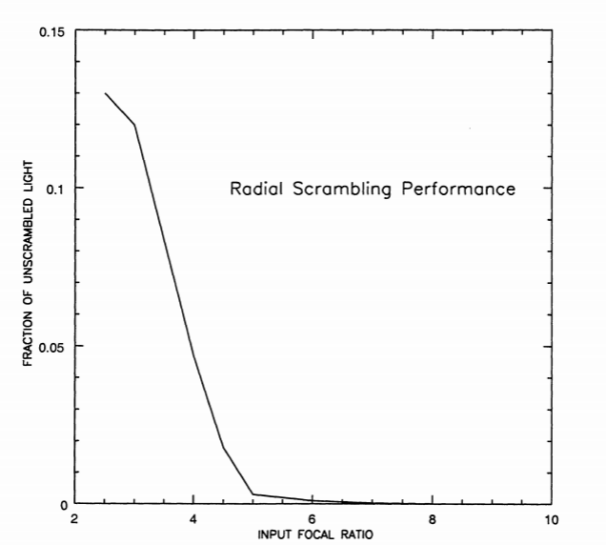

Figure 2.21: Fraction of unscrambled light as a function of input f-ratio. [59]

2.5 Infrared detector technologies

This section is intended to review the current detector technologies available in the required wavelength range and identify selection criteria. Moreover, the choice of the most suitable detector is not a negligible factor as it strongly influences many aspects of the instrument. Its characteristics are, for example, involved in the derivation of the instrumental parameters that define the spectrometer configuration (see Sec. 4.2.1).

Two main types of IR detectors are identified; thermal and photonic. The IR detectors using photoelectric effects are photon detectors or quantum detectors and are measuring the photons with quantum energy higher than the internal conduction energy gap. On the other hand, bolometric or thermal detectors measure the thermal effect of the incident IR radiation. For example, the variation of the vibration energy of a crystalline reticle caused by the incident infrared radiation is measured by the variation of electrical resistance. [63] The selection of the detector type can be made from three main criteria; volume, performance and cost. Thermal detectors generally have a lower cost but also lower performances and a higher volume. Inversely, photonic detectors have smaller sizes, higher performance and a higher cost. [64] Moreover, they need to operate at very low temperatures, depending on the wavelength and detector material.

Historically, detector technologies were mainly based on compound semiconductors. Early thermal detectors were mainly thermocouples and bolometers. These were sensitive to all infrared wavelengths but were of relatively low sensitivity and slow response time. The first practical photon detectors were made out of lead sulfide PbS and were sensitive to infrared wavelengths up to $\sim 3\,\mu$m. [63] Later, higher performance (TaS, PbSe and PbTe) IR detectors were developed by Cashman. These extended the spectral range beyond that of PbS, providing sensitivity in the $3-5\,\mu$m medium wavelength (MWIR) atmospheric window. By 1960, thanks to direct band gap materials based on ternary semiconductor compounds (HgCdTe ad PbSnTe), the first linear arrays of tens of elements were developed. In the mid-seventies, the first CCD IR bidimensional arrays were produced. It enables very high spatial resolution with a very large number of pixels.

Current technology is still mainly based on Mercury-Cadmium-Telluride (MCT) which has a tunable bandgap spanning the shortwave infrared to the very long IR regions. Moreover, the amount of cadmium in the alloy can be chosen to tune the optical absorption cutoff frequency. Secondly, quantum-well infrared photodetectors (QWIP) are used for IR observation. These detectors use electronic intersubband transitions in quantum wells to absorb photons (see Fig 2.22). The parameters of the quantum wells are then adjusted so that the energy difference between its first and second quantized states match the incoming infrared photon energy. The detector material is based on AlGaAs/GaAs quantum wells grown on GaAs substrates. Although they have a lower quantum efficiency, the performances are generally close to CMTs. Furthermore, they show higher homogeneity and stability in sensitivity thanks to a more reliable manufacturing process.

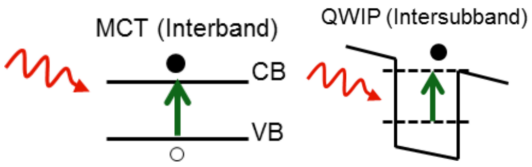

Figure 2.22: Energy band diagram of MCT and QWIP showing electronic transition. [64]

Thanks to the ability of MCT material to be tuned in terms of cut-off wavelength, it is possible to cover a very wide spectral range. This is represented and compared to other current technologies available in the infrared wavelength domain in Fig. 2.23. One can also see that each technology is associated to a well-defined wavelength range. For array detectors in the $1-5\,\mu$m range, devices developed by the Rockwell International Science Center are recommended. [65] Their next-generation, state-of-the-art HAWAII detectors are perfectly suited for the application of exoplanet spectroscopy.

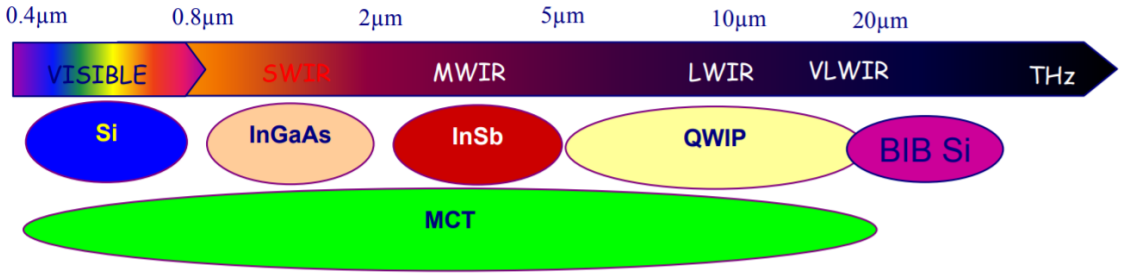

Figure 2.23: : Detection technologies covering infrared spectrum. [66]

Chapter 3

Theoretical background on spectroscopy

3.1 Basic principles of Spectrometers

The light collected by a telescope is composed of a certain range of wavelengths mixed together. A spectrometer is an optical instrument that separates and measures the wavelength of the observed light source. This can be achieved with a configuration composed of five optical components. The **entrance aperture** is the limiting physical aperture that determines the amount of light that reaches the imaging area[2]. The size and shape of the aperture also defines the diffraction pattern and therefore the resolution of the system (see Sec. 4.3.1 on the Rayleigh criterion). The light is then collimated by a **collimator** which changes the direction of diverging light into a parallel beam. This ensures that the light will hit the **dispersing element** with a constant incidence angle for optimal performance. The dispersing element, usually a diffraction grating or a prism, is the key element of the spectrometer. It causes light dispersion allowing to discriminate the different wavelengths. All light of the same wavelength and spectral order leaves the dispersive element under the same angle. Each wavelength is then collected by the **camera or focuser** which refocuses the spectrum onto the output plane, usually a **detector or an exit aperture**.

[2]Note that if present, an exit slit or aperture also limits the amount of light exiting the system.

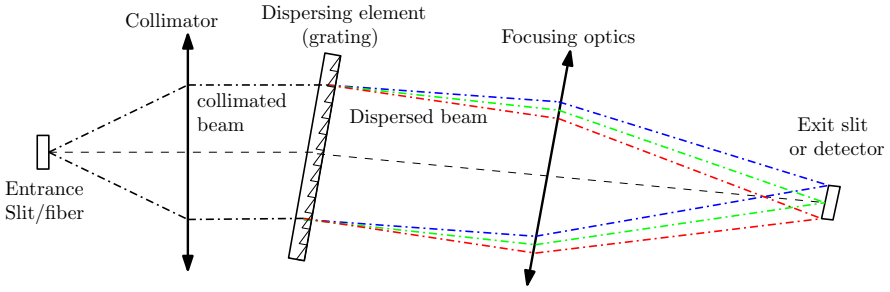

Figure 3.1: Schematic diagram of a spectrograph

A schematic view of a typical spectrograph and its optical components is shown in Fig. 4.1. However, in the context of this master thesis, the spectrograph designed in the following section is fully reflective but the basic concepts remain the same.

3.2 Diffraction gratings parameters

The dispersion of light into a spectrum is provided by the dispersing element, usually a grating. In the context of this report, a reflective diffraction grating is used which can be characterised by the following parameters:

- d = groove spacing
- L = size or length of the grating
- α = the incidence angle
- β = the diffraction angle
- m = spectral order of diffraction

The angles α and β are taken with respect to the grating normal which is the perpendicular axis to the grating surface and is noted N. This is schematized in Fig. 3.2.

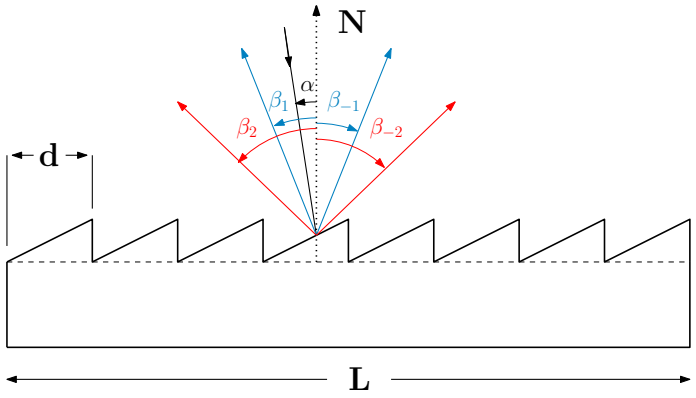

Figure 3.2: Schematic diagram of a reflective diffraction grating. The different diffraction orders are depicted with distinct colors.

Note that here, only the diffracted light rays are shown. In reality, there is also a part of reflection, absorption and scattering which needs to be taken into account. The subscripts of the diffraction angle $(-2, -1, 1, 2)$ correspond to the different orders of diffraction. For a given wavelength λ, the diffraction can be computed by the general grating equation.

$$m\lambda = d(\sin\alpha \pm \sin\beta) \tag{3.1}$$

Since the incoming light is usually collimated by the collimator, α can be considered constant. By convention, α and β are measured positive if they lie on the same side of the grating normal. When α and β are at opposite sides of the grating normal, the grating equation (Eq. 3.1) with the negative sign should be used. This is schematized in Fig. 3.3

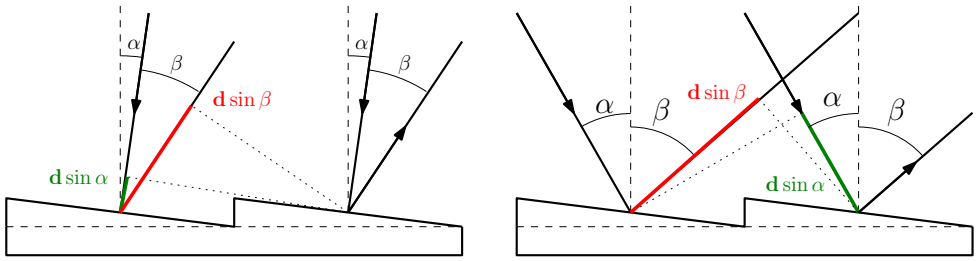

(a) $m\lambda = d(\sin\alpha + \sin\beta)$ (b) $m\lambda = d(\sin\alpha - \sin\beta)$

Figure 3.3: Possible optical arrangements for reflective gratings. The path differences of the incident and diffracted beams are highlighted in green and red respectively. **(a)** When adding the path differences, both incident and diffracted beams are on the same side of the grating normal. **(b)** When subtracting the path differences, the beams are at opposite sides of the grating normal.

3.2.1 Free spectral range

When light with a wide range of wavelengths is directed at a grating, neighbouring orders of spectra may partially overlap (see Fig. 3.4). The free spectral range is the range that is available without a spectral overlay. It can be determined from the condition that the shortest detectable wavelength λ_1 in the order $m+1$ just overlaps with the longest detectable wavelength λ_2 in the order m:

$$(m+1)\lambda_1 = m\lambda_2$$

The free spectral range of order m is then:

$$FSR = \lambda_2 - \lambda_1 = \frac{\lambda_1}{m} \tag{3.2}$$

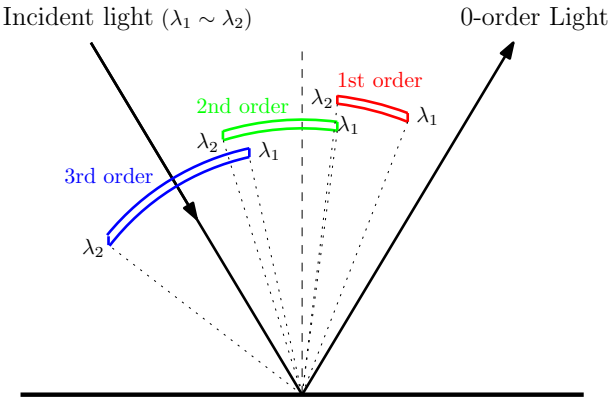

Figure 3.4: Free spectral range on a grating. The different colors are associated to the spectral dispersion of the three first diffraction orders for an incoming light with wavelengths between λ_1 and λ_2. The condition is respected between the first and second order as there is no spectral overlay.

3.2.2 Dispersion of grating

The angular dispersion is a measure of the angular separation of light rays of different wavelengths traversing a diffraction grating. It is defined as the rate of change of the angle of diffraction with respect to the change in wavelength,

$$D = \frac{\partial\beta}{\partial\lambda}$$

The theoretical angular dispersion can be obtain by differentiating Eq. 3.1,

$$m\partial\lambda = d\cos(\beta)\partial\beta \tag{3.3}$$

$$\Leftrightarrow \frac{\partial\beta}{\partial\lambda} = \frac{m}{d\cos(\beta)} \tag{3.4}$$

From Eq. 3.4, the linear dispersion (length per unit of λ) at the detector can be derived,

$$\frac{\partial L}{\partial \lambda} = f \frac{\partial \beta}{\partial \lambda} \tag{3.5}$$

where f is the focal length of the focusing mirror.

3.3 Geometrical considerations

When designing any optical component, it is of importance to identify the impact that a variation in any geometrical dimension (e.g. mirror size) will have on the performance of the component. The interrelation of the spectrometer's key parameters are listed below and will be covered in more detail in the parametric study in Sec. 4.2.2.

- **mirrors focal lengths:** Longer focal lengths allow a better dispersion and a higher resolution. It also enhances the quality of spectral and image transfer but lowers the light flux.
- **mirrors diameters:** A bigger diameter allows a higher light flux to pass through. However, larger apertures and angles produce lower transfer quality.
- **The groove density of the grating:** The higher the density is, the higher the dispersion and resolution are, but also the lower the projected area at higher working angles of the grating. A higher groove density is also more complicated to manufacture, which considerably increases the price of the grating.
- **The size of entrance and exit aperture:** A wider slit lets more light pass through but lowers the resolution. Similarly to the mirror diameter, a higher slit increases the light flux at the expense of transfer and image quality.
- **Internal angles:** Smaller angles allow a larger effective disperser area for better performance. Also, the tighter the angles are, the better the geometric functions, leading to smaller components or increased focal length. Furthermore, smaller off-axis angles at the mirrors are accompanied by reduced aberrations.

3.4 Reflective spectrometer configurations

The purpose of this section is to review the different existing spectrometer configurations to identify their main advantages and disadvantages to provide selection

criteria for the application of exoplanet spectroscopy.

In opposition to the use of refractive optics in a spectrometer, a fully reflective design eliminates the problem of chromatic aberration. Moreover, spherical aberration can be corrected with parabolic mirrors for axis-parallel beams reaching the reflectors. On the other hand, to avoid vignetting and due to geometrical considerations, a reflective spectrometer design requires an off-axis configuration. [67] This induces the presence of aberrations like coma and astigmatism.

3.4.1 Littrow configuration

The Littrow configuration was first introduced in 1963 by the lesser-known Otto von Littrow. A similar but simpler design was also introduced by Jules Dubosq, a French optician to which the 30° 'Littrow prism' is attributed. Both design variants and their derivatives were well received at the time and are still commonly used for today's applications, mainly for small telescopes. [68]

The initial configuration consists of only three components: a pinhole, a prism, and a spherical mirror. [69] The simplicity of the design allows a cheap and straightforward setup which explains its abundant use among amateur astronomers. The spherical mirror acts both as a collimator and focusing unit. In more recent versions a reflective diffraction grating is used instead. Also, the pinhole was separated into an entrance slit and an exit slit as represented in Fig. 3.5.

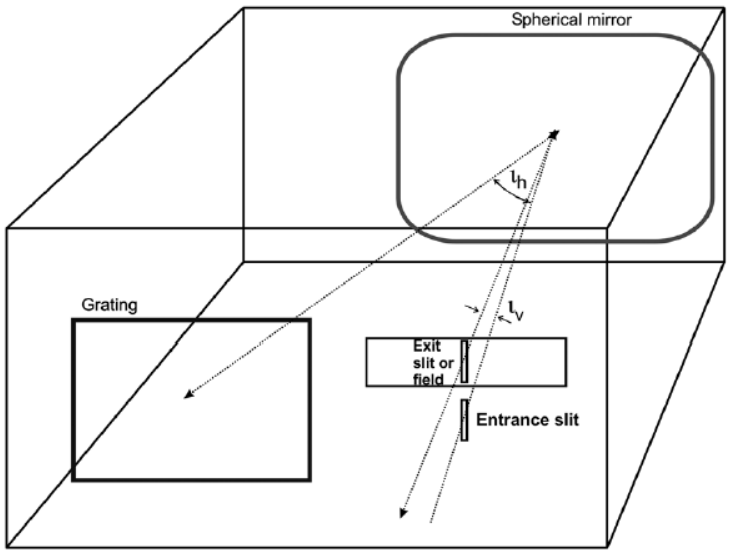

Figure 3.5: Schematic representation of the Littrow configuration. [69]

The design is mainly characterized by the blaze angle θ_B, the angle between the step normal and the grating normal. The latter is chosen such that the diffraction angle and incidence angle are equal,

$$\theta_B = \alpha = \beta$$

maximizing the efficiency for the wavelength of the used light. This is represented in Fig. 3.6. Equation 3.1 is then reduced to the Littrow equation.

$$m\lambda = 2d \sin \alpha \tag{3.6}$$

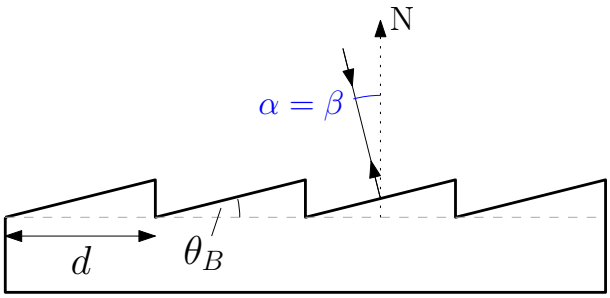

Figure 3.6: Diffraction at a Littrow grating

Advantages

- Small internal angles leads to smaller components, longer focal lengths and the use of only one mirror.
- High-quality image transfer, which produces high resolution and allows for high entrance slits and results in a large field at the exit.
- High, straight slits provide a high resolution and a large aperture.
- The optical setup only needs three degrees of adjustment: distance, and horizontal and vertical tilt.

Drawbacks

- The entrance and exit are extremely close to each other.
- A high risk of internal reflections and multiple dispersion at low grating angles.
- A high risk of stray light.

3.4.2 Ebert-Fastie configuration

The Ebert-Fastie configuration was firstly designed by William G. Fastie in 1952. Fastie based his design on a much older one by Ebert (1889). A major drawback of the original concept by Ebert is the possible direct reflection of light from the entrance to exit without diffraction. Fastie corrected this by increasing the width of the mirror to allow a baffle in the centre which avoids the direct transfer from the entrance to the exit slit. Fastie was a co-investigator in the Mariner 5 flyby of Venus in 1967 and the Mariner 6 and 7 flybys of Mars in 1969 and was also the principal investigator for the ultraviolet spectrometer experiment on Apollo 17 in 1972. All the missions except for the first flyby carried ultraviolet spectrometers based on his design. [70] [71]

The general Ebert-Fastie configuration consists of a single spherical mirror[1] and a grating centred on the optical axis of the spherical mirror. In opposition to Littrow's configuration, the entrance and exit slit are located at the two opposite sides of the dispersive element, requiring a much larger mirror. A particularity of Fastie's design is the curved slits located at the radius around the grating's centre, which is also the centre of the spectrometer. A schematic representation of the design is illustrated in Fig. 3.7. The simplicity and the ideal symmetry of the design allow for easy manufacturing.

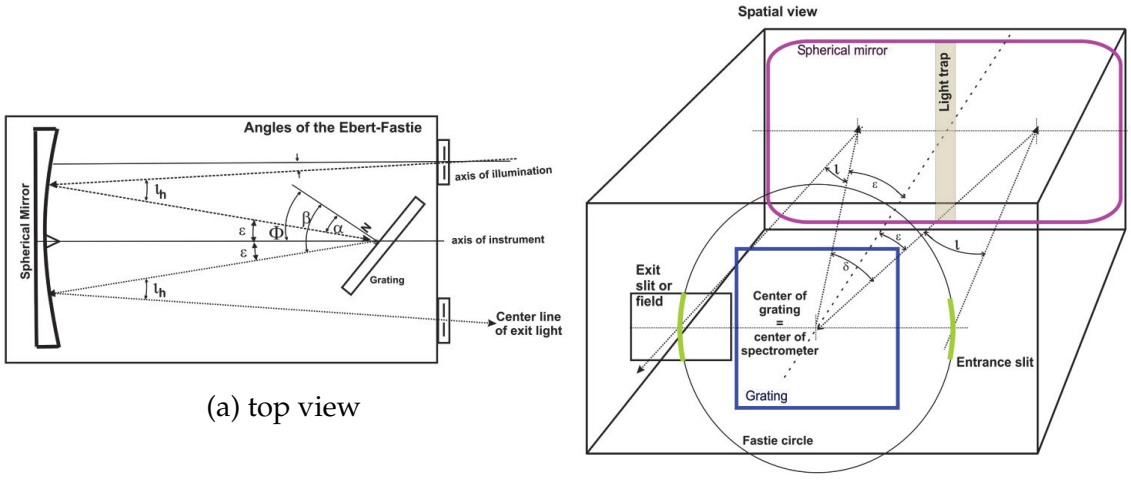

(a) top view

(b) spatial view

Figure 3.7: Schematic representation of the Ebert-Fastie configuration. [69]

The input and output angles ε of the grating are equal due to the symmetry of the

[1] Altough, in his paper, William G. Fastie already mentioned the possible use of two off-axis parabola mirrors for good imaging, which directly hints towards a Czerny-Turner system described in the following subsection.

design. One can also define Φ as the angle at which the grating is moved away from the position of pure reflection corresponding to the zeroth order:

$$\Phi = \frac{\alpha + \beta}{2} \tag{3.7}$$

This angle is also often called the blaze angle and plays an important role in the design of the spectrometer as described in Sec. 4.2.1.

Advantages

- The design makes uses of large curved slits offering a high light flux
- The use of only one spherical mirror acting as both collimator and focuser keeps the design simple.
- Very good stigmatic transfer, caused by symmetric design.
- All kind of dispersers (prisms & reflective gratings) can be used, especially echelle gratings for which $\varepsilon < 10\,\text{deg}$ is possible.

Drawbacks

- The spherical mirror causes image aberrations such as spherical aberration, and a curved image field.
- Larger internal angles ε could be required, increasing off-axis aberrations (coma, astigmatism).
- Risk of internal reflection and multiple dispersions at grating angles near ε.

3.4.3 Czerny-Turner configuration

Czerny and Turner presented their concept in the 1930s and is an improved form of the Ebert design. The main difference is that the spherical mirror has been separated into a collimator and a focusing mirror. It can also use an output slit behind the focusing mirror to select individual wavelengths and act as a monochromator. By selecting the right mirrors spherical aberration can be corrected as well as coma. However, adding optical components also increases the complexity of the system. The design of a Czerny-Turner spectrometer is illustrated in Fig. 3.8.

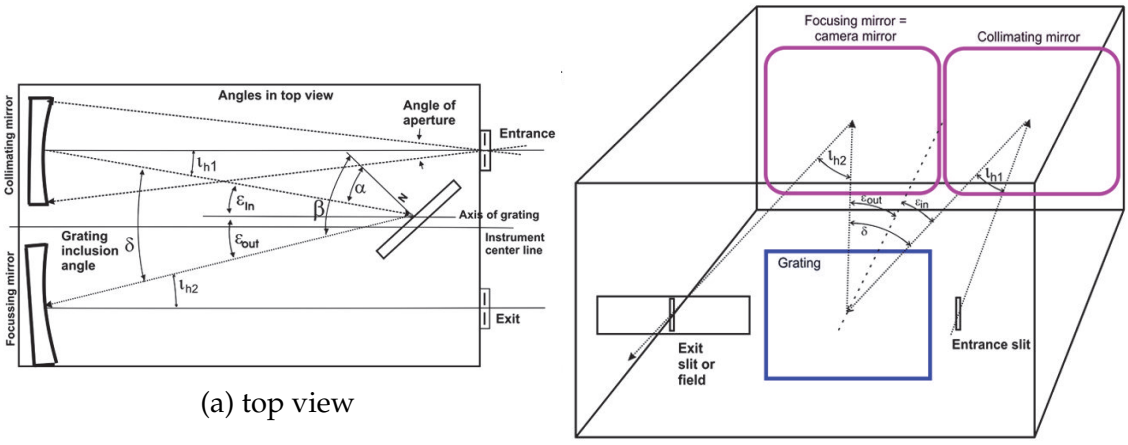

(a) top view

(b) spatial view

Figure 3.8: Schematic representation of the Czerny-Turner configuration. [69]

Unlike the Ebert-Fastie configuration, the grating input and output angles (ε_{in} and ε_{out} respectively) as well as the internal angles l_{h1} and l_{h2} are different from each other. A particular advantage of this configuration is the freedom of building the instrument. Different design can be used for the same focal lengths and f-number. It also allows to minimize internal reflections and multiple dispersions, and eventually produces less stray light. Despite the very flexible configuration, the nine degrees of adjustment freedom contribute to an increased complexity which might create some problem when aligning the instrument, reducing the performance of the spectrometer.

Advantages

- High flexibility of the design, both mirror can be made of different sizes
- The direct reflection of input to output is prohibited and internal reflection minimized.
- The beam configuration can be designed such that all entrances and exits are plane parallel to the housing

Drawbacks

- Increased complexity of the design may cause alignment error, deteriorating the performance
- When using concave mirrors, the off-axis nature of this system produces astigmatism and coma.
- The combination of mirror optics makes the spectrograph consequently relatively large and heavy.

Crossed Czerny-Turner variant

The flexibility of the Czerny-Turner design allows all sorts of configurations. An example of a derivative of the Czerny-Turner spectrograph is the crossed system represented in Fig. 3.9. It is widely used for Raman spectroscopy due to its relatively compact size, low cost and non-destructive nature. [72] It possesses the same advantages as the classical Czerny-Turner configuration except it has a stronger condenser capacity[1] as well as lower stray light. [73] On the other hand, even for crossed spectrometers verifying the coma-free condition established by Shafer [74] (see Sec. 4.5.1), a quite large residual astigmatism remains present. Although, several authors have determined astigmatism correction methods. [72] [73]

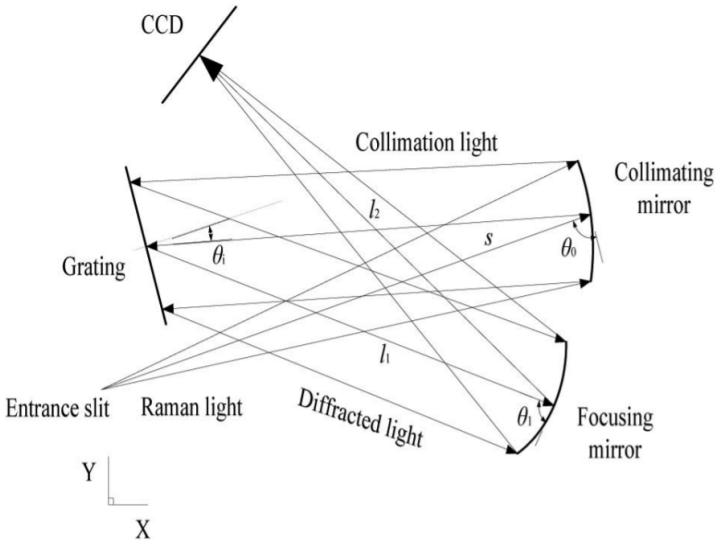

Figure 3.9: Optical scheme of the asymmetrical crossed Czerny–Turner spectrometer. [72]

[1] The condenser capacity of the classical C-T spectrometer is determined by the grating size that is restricted by the system miniaturization. [73]

Chapter 4

Optical design

This chapter focuses on the optical design of the spectrometer. First, the different parameters of the instrument are presented and computed by taking into account the scientific requirements fixed by the SCIFY project and using the equations developed in the previous chapter. As a reminder, a resolution power of 2000 is required in the 3.5 to 4.0 μm wavelength range. Also, each wavelength element has to be discretized over 3 pixels in the dispersion direction. The spot sizes should ideally be contained within the Airy disk whose radius must be the size of 2 pixels. This gives a restriction on the diffraction limitations of the system which is also discussed. Finally, the selection of the configuration is described and will be used as a basis for the implementation in ray-tracing software Code-V in the next chapter.

4.1 Spectrometer parameters

The key optical component in a spectrograph is the dispersive element. Before starting the calculation of the different parameters, it is of importance to pre-select the type of dispersive element that will be used. In the scope of this master thesis, the possibility of integrating a fully reflective spectrometer for the SCIFY project is analysed as a potential alternative to the refractive grism design considered by the SCIFY team. A grism (compound optical element composed of a grating and a prism) permits an in-line optical layout by exploiting the differences between gratings and prisms. However, grisms are considerably more expensive to manufacture then reflection gratings. Moreover, according to Jacquinot's analyses[2], gratings outperform similar size prisms by a factor of 50–100 in the near-infrared,

[2]Jacquinot's paper (1954) was published at a time when low-cost blazed gratings were becoming available. This availability, and Jacquinot's theoretical demonstration of the superiority of such gratings over prisms contributed to the decline in the use of prism spectrometers in the second half of the twentieth century.

and 5–10 times in the near-ultraviolet and infrared. [75] Additionally, a comparison study by Ch. Fehrenbach (1955) shows that under normal conditions of use of a large telescope a grating spectrograph is about three times more efficient than a prism instrument. [76] A blazed grating spectrograph is therefore selected.

Next, the scientific requirements described in section 1.3.2 have to be translated into technical specifications. Furthermore, an identification of the spectrometer parameters is required to know which parameters to fix and which to be deduced. Once those have been fixed, the relations described in the previous chapter are used to deduce the remaining parameters. The different parameters that describe the spectrograph are displayed in Tab. 4.1.

λ_1	Minimum wavelength
λ_2	Maximum wavelength
R	Resolving power
α	Incidence angle
β	Diffraction angle
m	Grating order
L_D	Detector size
f_{coll}	Focal length of collimator
D_{beam}	Beam diameter
f_{cam}	Focal length of camera
M	Magnification
d	Groove spacing
w_{slit}	Input slit width

Table 4.1: Parameters describing a spectrograph instrument

In Figure 4.1, a common reflective design in the Czerny-Turner configuration is illustrated and defines the key design parameters of a spectrometer.

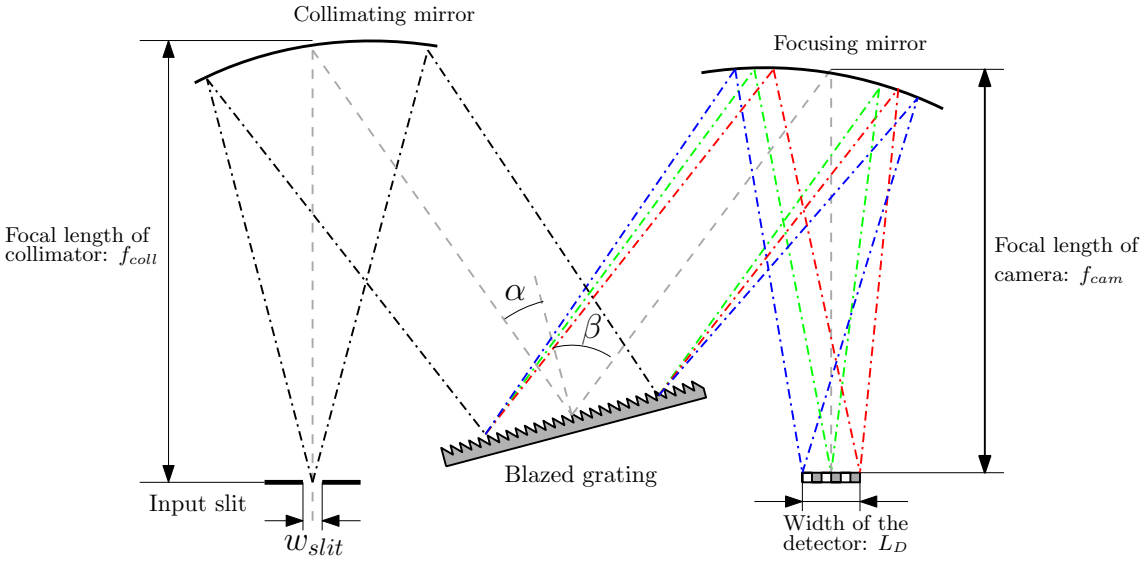

Figure 4.1: Schematic view of a Czerny-Turner configuration with the spectrometer parameters

4.2 Design methodology

4.2.1 Preliminary design

The wavelength range and resolving power have been defined by the scientific requirements, tabulated in Tab. 1.1. These are the key input parameters in the design process as it allows to define the centre wavelength λ_c which is also the design wavelength.

$$\lambda_c = \frac{\lambda_1 + \lambda_2}{2} \tag{4.1}$$

The scientific requirements impose a resolving power of $R = 2000$ over the spectral range $3.5 - 4\,\mu$m. Using the definition of the resolving power, the average spectral resolution $\delta\lambda$ can be computed,

$$R = \frac{\lambda_c}{\delta\lambda} \tag{4.2}$$

$$\begin{aligned} \Leftrightarrow \delta\lambda &= \frac{\lambda_c}{R} \\ &= 1.875\text{nm} \end{aligned}$$

From this, the detector parameters can be obtained. The Nyquist theorem states that each wavelength resolution element has to be discretized by at least two pixels. The scientific requirements impose a discretization over 3 pixels. Then,

the required number of pixels to cover the entire considered waveband of 500 nm is,

$$N_{pix} = 3\frac{\lambda_2 - \lambda_1}{\delta\lambda} = 3\frac{500\text{nm}}{1.875\text{ nm}} = 800\text{pixels}$$

For an off-the-shelf medium-wave infrared detector with a pixel width (p) of 18 μm, the minimum required detector size L_D can be assessed,

$$L_D = N_{pix}p = 14.4\text{mm}$$

The results show that the minimum required detector size is equal to 14.4 mm for $R = 2000$. For the low resolution mode ($R \sim 100$), only 40 pixels are required for a minimum size of 0.72 mm. On the other hand, the high resolution mode ($R \sim 10000$) requires the spectrum to be spread over 4000 pixels. This means that the HAWAII-2RG detector considered by the SCIFY team with a 2048×2048 resolution and pixel size of 18 μm is sufficient for the two lowest resolution modes. For the high resolution mode a larger detector is required such as the HAWAII-4RG that has a 4096×4096 pixel array with a pixel size of 10 or 15 μm. Another option is to separate the spectrum over two HAWAII-2RG detectors.

Next, the geometry of the system has to be assessed. It is mostly determined by the angles at the grating. As a matter of fact, the chosen incidence and diffraction angles at the grating define the configuration used as explained in Sec. 3.4. Instead of fixing α and β, the blaze angle is more likely to be specified. [77] It is defined as,

$$\theta_B = \frac{\alpha + \beta}{2} \tag{4.3}$$

This angle is usually specified by grating manufacturers and is optimized to maximize efficiency for the design wavelength λ_c. This means that θ_B is chosen such that the beam diffracted at the grating and the beam reflected at the steps are both deflected into the same direction. For the considered wavelength range, this angle usually lies around $25 - 30°$ for blazed (ruled) grating and at first-order diffraction. For echelle gratings, the blaze angle is significantly larger and can go up to 80°.

Another angle of interest is the Littrow angle γ which represents how far the spectrograph is from the Littrow configuration. It also gives an idea of the angular separation for the collimator-grating-camera optical chain. This parameter should be chosen carefully by the designer to ensure that there is no beam obstruction between the different optical components. It is defined as,

$$\gamma = \alpha - \beta \tag{4.4}$$

The groove spacing can then be deduced from Eq. 3.1,

$$\begin{aligned} m\lambda_c &= d(\sin\alpha + \sin\beta) \\ \Leftrightarrow m\lambda &= 2d\sin(\theta_B)\cos\left(\frac{\gamma}{2}\right) \\ \Leftrightarrow d &= \frac{m\lambda_c}{2\sin(\theta_B)\cos\left(\frac{\gamma}{2}\right)} \end{aligned}$$

Usually, diffraction grating manufacturers provide the blaze angle and groove density of the dispersing element. Then, d becomes a fixed parameter and the equation is solved for the Littrow angle γ instead.

Once the incidence and diffraction angles at the grating have been determined, the focal length of the focusing mirror can be obtained to ensure the required spectral dispersion. As a matter of fact, in order to obtain the required resolving power of $R = 2000$, the entire wavelength range of 500 nm has to be spread over the determined detector length (14.4 mm). From Eq. 3.5 and 3.4,

$$\frac{\partial L}{\partial \lambda} = \frac{L_D}{\lambda_2 - \lambda_1} = f_{cam}\frac{m}{d\cos(\beta)} \tag{4.5}$$

By solving for f_{cam}, Eq. 4.5 becomes,

$$f_{cam} = \frac{d \cdot L_D \cos\beta}{m(\lambda_2 - \lambda_1)} \tag{4.6}$$

Finally, the focal length of the collimating mirror can be assessed. Usually, collimator and camera optics have different focal lengths. Both influence the imaging magnification and reduction in the spectrometer. The image relation in a spectrograph can be determined, starting from the lens equation,

$$\frac{1}{f} = \frac{1}{u} + \frac{1}{v} \tag{4.7}$$

where f is the focal length of the respecting lens or mirror, u the object distance and v the image distance. Generally, in astronomy, the object is very distant (e.g. a star, an exoplanet, a galaxy,...). Thus, considering the object distance to be infinite ($u \to \infty$) is a good approximation. Eq. 4.7 can then be simplified as,

$$f = v \tag{4.8}$$

meaning that the object is imaged in the focal plane of the lens. The image size can be calculated starting with the intercept theorem which provides the following relation,

$$\frac{U}{u} = \frac{V}{v} \tag{4.9}$$

where U is the object size and V the image size. Coming back to the general thin lens equation (Eq. 4.7) and solving for u gives,

$$u = \frac{f \cdot v}{v - f} \tag{4.10}$$

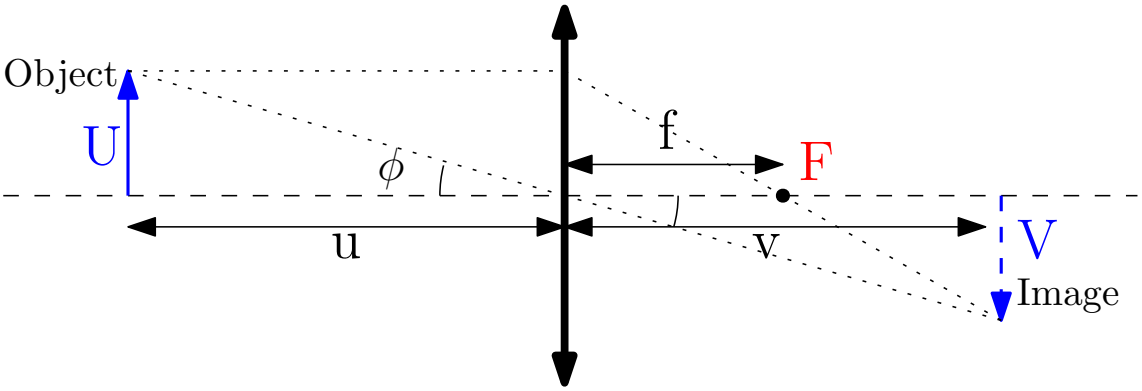

Figure 4.2: Scheme defining the parameters of the thin lens equation

By injecting Eq. 4.10 into Eq. 4.9, the image size U is obtained,

$$U = \frac{f \cdot v}{v - f} \frac{V}{v}$$

The ratio V/v is the tangent of the angular dimension of the object (see Fig. 4.2). The relation for the object size becomes,

$$U = \frac{f \cdot v}{v - f} \cdot \tan\phi \tag{4.11}$$

Factoring out v in the denominator and estimating v to be at infinity gives the final relation for the object size,

$$\begin{aligned} U &= \lim_{v \to \infty} \frac{f}{1 - \frac{f}{v}} \cdot \tan\phi \\ &= f \cdot \tan\phi \\ &\simeq f \cdot \phi \end{aligned}$$

In the context of a spectrograph, considering a slit of width s to be imaged by the collimator (virtually coming from infinity) at the angle $\phi \simeq s/f_{coll}$, the image size s' can be computed,

$$s' \simeq f_{cam} \cdot \phi \tag{4.12}$$

$$\simeq f_{cam} \cdot \frac{s}{f_{coll}} \tag{4.13}$$

The slit image s' in the camera focal plane depends linearly on s. Additionally, the effect of a diffraction grating placed between the collimator and the camera is investigated. Eq. 3.1 gives the relation between the angles at the grating and the wavelength. By deriving the grating equation for α and β we obtain,

$$\frac{d\lambda}{d\alpha} = \frac{d}{m} \cdot \cos\alpha \tag{4.14}$$

$$\frac{d\lambda}{d\beta} = \frac{d}{m} \cdot \cos\beta \tag{4.15}$$

We take the ratio of both derivatives,

$$\frac{d\lambda}{d\alpha} / \frac{d\lambda}{d\beta} = \frac{d\lambda}{d\alpha} \cdot \frac{d\beta}{d\lambda} = \frac{d\beta}{d\alpha} \tag{4.16}$$

and obtain by division,

$$\frac{d\beta}{d\alpha} = \frac{\cos\alpha}{\cos\beta} \tag{4.17}$$

which can be approximated as,

$$\Delta\beta \simeq \frac{\cos\alpha}{\cos\beta} \cdot \Delta\alpha$$

This means that when changing the angle of incidence α by $\Delta\alpha$, the diffraction angle changes proportionally with a factor $\cos\alpha / \cos\beta$ also called the anamorphic magnification factor. To account for this magnification or reduction factor, Eq. 4.12 becomes,

$$s' = s \cdot \frac{\cos\alpha}{\cos\beta} \cdot \frac{f_{cam}}{f_{coll}} \tag{4.18}$$

By defining the magnification of an image M as the ratio of the height of the image to the height of the object we have,

$$M = \frac{V}{U} = \frac{v}{u}$$

The spectrometer is imaging the input slit to the detector and we generally want to have the slit as wide as possible to collect as much light through the input slit as possible. Therefore, the magnification in the system M should preferably be close to 1 which means that the width of the input slit ideally is imaged 1:1 onto the detector array. Eq. 4.18 can then be solved for f_{coll},

$$f_{coll} = f_{cam} \frac{\cos\alpha}{\cos\beta} \tag{4.19}$$

The last parameter from Tab. 4.1, describing the spectrograph, that has to be computed is the input slit width. For a fibre-fed spectrograph, the numerical aperture

of the input slit is determined by the size of the fibre cores. For single-mode fibres, the equivalent slit width is typically around 10 μm. Finally, the main parameters describing the spectrograph have been determined. The general procedure used for the primary calculation of the design is schematized in Fig. 4.3.

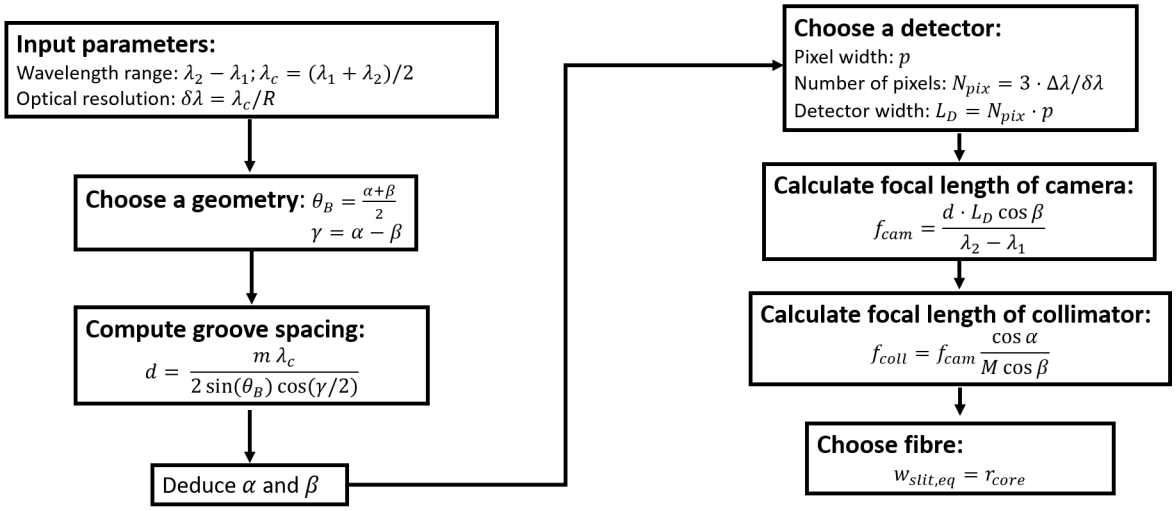

Figure 4.3: Schematic view of the general procedure used for the primary calculation of the design.

4.2.2 Parametric study

In order to explore the different possibilities in the design, a parametric analysis is performed. It allows examining how the system behaves to a variation of the input parameters. First, those input parameters have to be chosen with care. From Fig. 4.3, the input parameters are the wavelength range and optical resolution. However, those are fixed by the scientific requirements (spectral band and resolution power). Instead, the impact of the geometry of the spectrograph is investigated. This involves the blaze angle θ_B and the Littrow angle γ.

Now, the parameters ranges have to be identified. This can be assessed by an overview of dispersive elements proposed by several diffraction grating manufacturers in the required wavelength range. Tab. 4.2 shows a comparison of the gratings that can be found on the company's websites.

	Thorlabs	Edmund Optics	Nilt	Dynasil	Gratinglab	Opcolab
Design Wavelength	3.5 μm	3.0 μm	-	4.0 μm	3.75 μm	4.0 μm
wavelength range	$2.5-4\,\mu$m	$1-5\,\mu$m	-	$2-7\,mu$m	-	-
Blaze Angle	26.5°	26.7°	10-50°	36.87°	13/26.7°	-
Grooves per mm	300	300	-	300	120/240	150
Dispersion [nm/mrad]	2.86	-	-	2.67	-	-
Peak efficiency	90%	72%	-	90%	>90%	67%

Table 4.2: Comparison of blazed ruled grating provided by grating manufacturers in the infrared wavelength range. The parameters are given for the design wavelength at Littrow configuration. [78] [79] [80] [81] [82] [83]

Blazed (ruled) gratings are usually manufactured with blaze angles between 20° and 40° and groove densities between 200 and 300 gr/mm. Some manufacturers such as Nilt also propose custom gratings with blaze angles that go down to 10° and up to 50°. It can also be seen that blazed gratings achieve a high peak efficiency at the blaze wavelength ($\sim$ 90%).

The Littrow angle $\gamma = \alpha - \beta$ on the other hand can be associated with the angle formed by the collimator-grating-camera optical sequence. In practice, γ must be large enough to allow space for camera components and the detector which should not interfere with the beam from the collimator. In his paper, Bingham investigated the effect of this angle on the spectrograph. He concluded that γ should have the same sign as the blaze angle and can sometimes take high values (more than 40°). However, a small value of the Littrow angle may ease the use of different gratings. It is therefore preferred in cases where it does not make the collimator too large (or else beam obstruction would occur) or sacrifice camera field. It is thus a trade-off between compactness and avoiding beam obstruction.

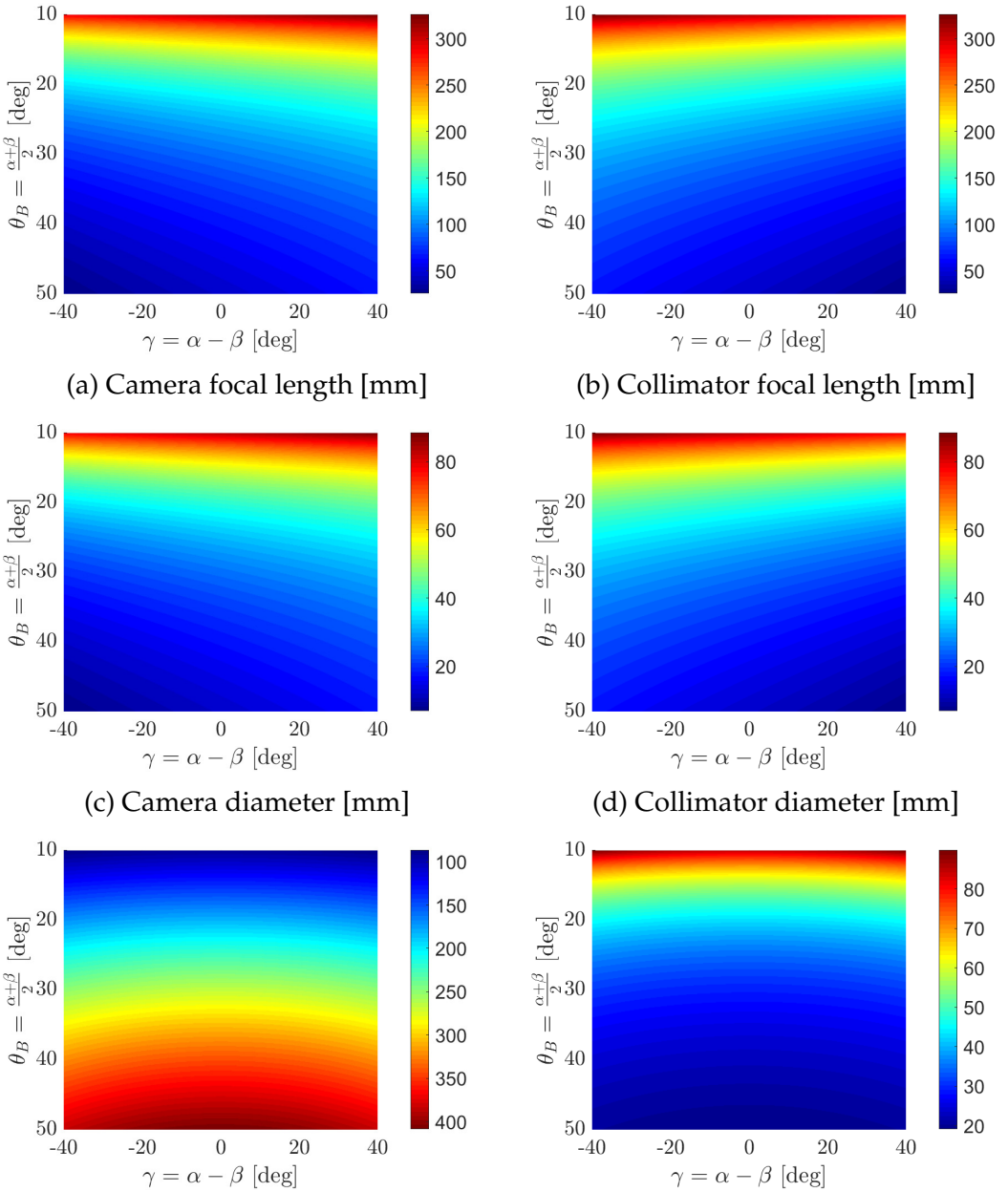

(a) Camera focal length [mm]

(b) Collimator focal length [mm]

(c) Camera diameter [mm]

(d) Collimator diameter [mm]

(e) Groove density [gr/mm]

(f) Grating size [mm]

Figure 4.4: Obtained specifications following the above mentioned design methodology for different values of θ_B and γ. The sizes and focal lengths for the different optical components are given by the colorbar on the right of each graph and are expressed in mm. The groove density in **(e)** is given in grooves per mm.

The variations of the instrument parameters are depicted in Fig. 4.4. First, it can be seen in **(a)** and **(b)** that the choice of a high blaze angle significantly decreases the mirrors focal lengths, allowing to limit the whole size of the instrument. Moreover, a decrease of both focal length is associated to a decrease of the

mirror sizes (see **(c)** and **(d)**) as those quantities are geometrically related by the relation,

$$\frac{D_{coll}}{D_{cam}} = \frac{\cos\alpha}{\cos\beta} \tag{4.20}$$

and where the focusing mirror aperture is determined by the diffraction limitation, directly related to f_{cam} (more details in Sec. 4.3). On the other hand, a reduction of the blaze angle leads to a higher grating size and a lower grating spatial frequency (see **(f)** and **(e)** respectively). The impact of the blaze angle on the grating size for a given Littrow configuration ($\gamma = 0$) is shown in Fig. 4.5.

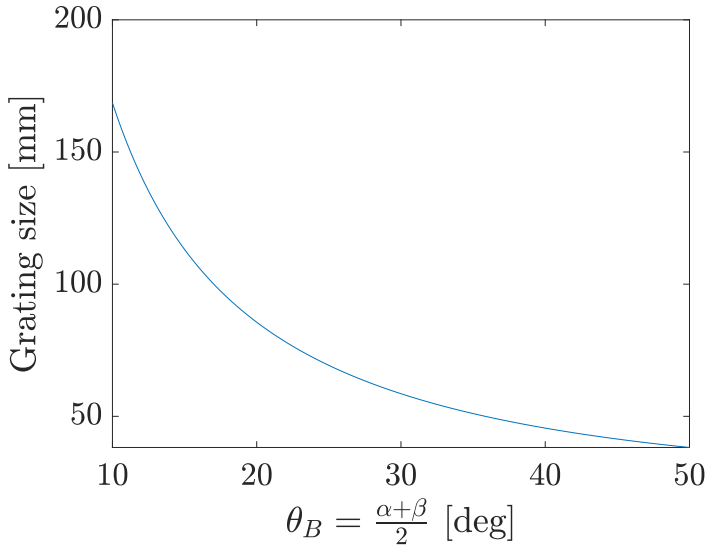

Figure 4.5: Grating size in mm as function of the blaze angle for the Littrow configuration ($\gamma = 0$)

Secondly, as stated by Bingham, the effect of reversing the sign of the Littrow angle causes variation opposite in signs for the mirrors focal lengths and apertures. In fact, the collimator size and focal length fall monotonically as $\alpha - \beta$ increases from zero with the same sign as the blaze angle, whereas the camera mirror size increases. This behaviour is interchanged if $\alpha - \beta$ is increased from zero with the other sign. Then, the collimator aperture increases while the camera size falls. This effect is illustrated in Fig. 4.6 for a fixed blaze angle. Usually, reducing A_{coll} is recommended when space is restricted, and increasing A_{cam} at constant relative aperture is often acceptable with regards to the induced aberrations. [77] Moreover, increasing the diameter of the focusing mirror is directly impacting the f-number of the system, reducing the Airy disk size. This is covered in more detail in Sec. 4.3.1.

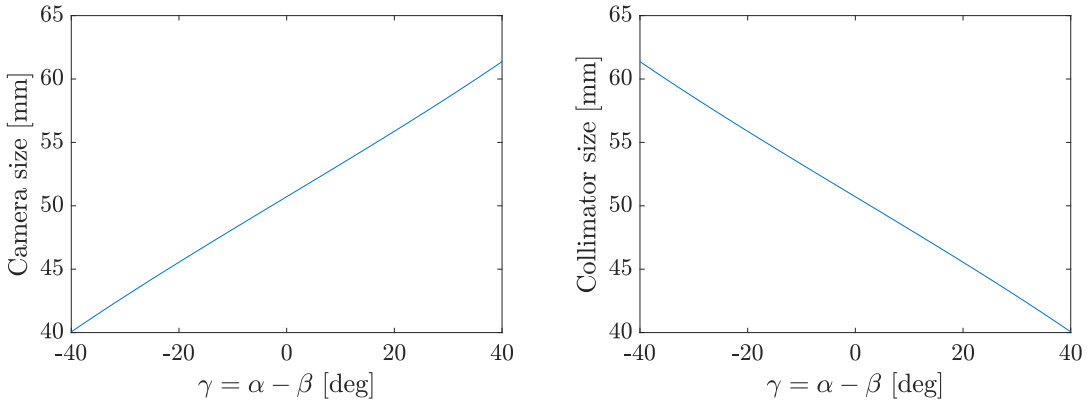

(a) Camera size

(b) Collimator size

Figure 4.6: Size of the collimating and focusing mirror as a function of the Littrow angle at a blaze angle $\theta_B = 30°$

4.2.3 Selected configuration

To implement the spectrograph into ray-tracing software for further analysis and optimisation, a configuration selection is performed. The design methodology established in Sec. 4.2.1 provides the necessary equations to obtain an initial design. First, the scientific requirements already provide the wavelength range ($3.5 - 4.0\,\mu$m) as well as the resolution power ($R = 2000$). Secondly, the geometry has to be chosen. An off-the-shelf grating with blaze angle $\theta_B = 26.7°$ is selected. Instead of fixing the Littrow angle, the groove density $G = 230$gr/mm has been carefully chosen such that the camera components and the detector do not interfere with the beam from the collimator. Finally, A Hawaii-2RG detector (2Kx2K pixels) with a square pixel size of $18\,\mu$m and cut-off wavelength of $5.3\,\mu$m has been selected.

The results of the calculations are shown in Tab. 4.3. The beam diameter has been determined from the diffraction limitations. As stated in the scientific requirements of the SCIFY project, the Airy disk as well as the spot size should be contained within a 2 by 2 pixels square. This is directly related to the size of the beam and therefore the diameter of the focusing mirror. The condition on the f-number of the system is described in Sec. 4.3.1 by using the Rayleigh criterion. The obtained configuration shows a relatively compact design as the highest focal length (collimator) is only 123.16mm. Both mirror sizes are also within an acceptable range. The size of the beam on the grating falls within the range of off-the-shelf gratings which usually have widths of 25 to 50 mm for the considered wavelength range.

Parameter	Value	Unit
Resolution ($\delta\lambda$)	1.875	nm
Size on detector (L_D)	14.4	mm
Grating order (m)	1	-
Groove density (G)	230	gr/mm
Angle of incidence (α)	10.4	°
Diffraction angle (β)	43	°
Grating size (W)	34	mm
Camera focal length (f_{cam})	91.57	mm
Camera size (A_{cam})	24.83	mm
Collimator focal length (f_{coll})	123.16	mm
Collimator size (A_{coll})	33.39	mm
Input slit width (w_{slit})	54	μm
Magnification (M)	1	-
Dispersion (D)	3.18	nm/mrad

Table 4.3: Spectrograph's parameters after calculation following the design methodology

For the spectrograph layout, a Czerny-Turner configuration has been adopted based on the comparison made in Sec. 3.4. It has a relatively simple design that incorporates three key optical elements; a spherical mirror, a plano dispersion grating, and a spherical focusing mirror. Furthermore, the separation between the collimator and camera enables high design flexibility as both mirrors can be made of different sizes.

4.3 Diffraction limitations

4.3.1 Rayleigh criterion

The resolution of an optical imaging system is limited by either external factors, an imperfection in the lenses due to manufacturing tolerances or even due to misalignment of the optical components. This mostly depends on the choice of the optical parameters as well as on the number of optical components. But even for a perfect system, the resolution of an image going through a small aperture is

limited by the aperture diffraction. The point at which the system is diffraction-limited is defined by the Rayleigh criterion. The Rayleigh criterion is a relation linking the aperture diameter of the imager to the smallest separation at which two points of light can be discerned. Mathematically, it is expressed as,

$$\sin\theta = 1.22\frac{\lambda}{D} \tag{4.21}$$

Where D is the diameter of the circular aperture and θ the angular separation of the two light points (see Fig. 4.7).

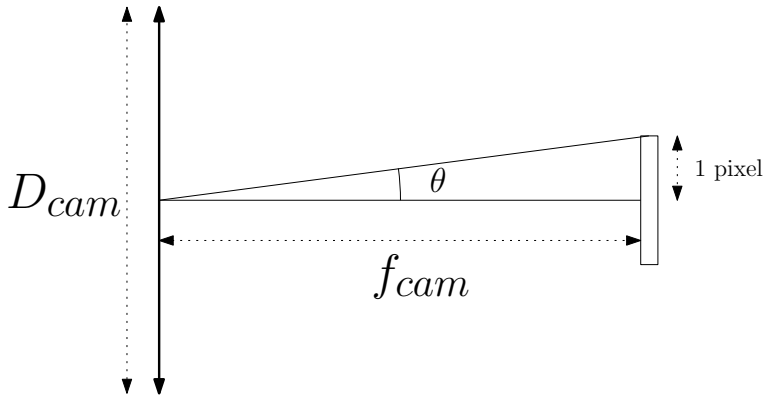

Figure 4.7: Definition of the parameters in Eq. 4.21

θ can also be seen as the angular separation for which the first diffraction minimum of the image of one source point coincides with the maximum of another. The spread of the diffraction-limited Point Spread Function (PSF) is thus approximated by the diameter of the first null of the Airy disk. By considering that the Airy disk must lie entirely within two pixels, a condition of the F-number can be obtained. From Fig. 4.7 and with the small-angle approximation, the Rayleigh criterion may be rewritten as,

$$\begin{aligned} \sin\theta \approx \theta &\approx \frac{p}{f_{cam}} \\ \Leftrightarrow F\# &< \frac{p}{1.22\lambda_{max}} \\ &< \frac{18\,\mu\text{m}}{1.22 \cdot 4.0\,\mu\text{m}} \approx 3.69 \end{aligned}$$

where p is the pixel width. This directly gives a condition on the minimum size of the camera,

$$D_{cam} = D_{beam} > \frac{1.22\lambda_{\max} f_{cam}}{p} \tag{4.22}$$

The size of the corresponding Airy disk determines the encircled energy for a diffraction-limited system. The system is said diffraction-limited when the spot size for each wavelength is contained within the Airy disk. The Fraunhofer diffraction for a single slit is described in Appendix A. It is then extended to a grating which is considered as a series of singles slits whose diffraction pattern interfere with each other in Appendix B. The theory of grating diffraction is then applied to the blazed grating to obtain the Blaze function that gives the efficiency of the grating as a function of the wavelength for the different diffraction orders (see Appendix C). This emphasizes the wavelength dependency of the grating efficiency and the concept of blaze wavelength.

4.4 Impact of incidence angle

The wavelength at which the grating has its maximum efficiency is called the blaze wavelength λ_{θ_B}. The blaze wavelength provided by grating manufacturers is generally given for a Littrow configuration ($\alpha = \beta$) such that,

$$\frac{n\lambda_{\theta_B}}{d} = 2\sin\theta_B \tag{4.23}$$

From Eq. 4.23, λ_{θ_B} is allocated to the blaze angle θ_B. When departing from the Littrow configuration, i.e. for an arbitrary incidence angle α, the blaze wavelength does not remain unchanged and slightly decreases. In fact, starting from Eq. 3.1, one can obtain,

$$\lambda_B = \lambda_{\theta_B}\cos(\alpha - \theta_B) \tag{4.24}$$

For a blazed grating with Littrow blaze wavelength $\lambda_{\theta_B} = 3.75\,\mu$m, blaze angle $\theta_B = 26.7°$ and the obtained angle of incidence displayed in Tab. 4.3, the blaze wavelength shifts to,

$$\begin{aligned}\lambda_B &= 3750\cos(10.4° - 26.7°)\\ &= 3599.2\text{ nm}\end{aligned}$$

This small deviation towards a shorter wavelength is acceptable as it stays within the wavelength range defined by the scientific specifications. However, if necessary, the Littrow angle $\alpha - \beta$ can be varied to slightly tune the blaze wavelength.

4.5 Aberration correction in spectrographs

The selected Czerny-Turner configuration has for advantage the separation between the collimating and focusing mirror, providing more degrees of freedom

for the design. However, the use of spherical optics and a plano grating inevitably introduce optical aberrations, mainly spherical, coma, and astigmatism. In its early days, the Czerny-Turner system was primarily used as a monochromator. In order to cover a spectral band, a rotating grating was used to scan the entire spectral range. Such a system was used in an on-axis configuration where the aberrations were kept small. [84] Later, the use of modern detector technology enabled the capture of the entire spectrum using a fixed grating. However, such a system includes off-axis optics and hence, aberration effects became more noticeable. To tackle this problem, several aberration correction designs have been proposed.

4.5.1 Coma

Coma aberration is the focal deviation for rays not parallel to the optical axis of an optical component. This creates a comet-like blur directed away from the optical axis. In their paper, Czerny and Turner showed that the coma aberration by the off-axis reflection of a spherical mirror can be corrected using symmetrical, but oppositely oriented, spherical mirrors for the spectrometer design. [85] However, this restricts the main advantage of the Czerny-Turner configuration; its design flexibility. This was until 1963 when Shafer published a paper showing that the coma aberration can still be corrected for asymmetrical Czerny-Turner configurations. [74] It places a condition on the geometry of the system, mathematically given by,

$$\frac{\sin\theta_C}{\sin\theta_F} = \left(\frac{R_C}{R_F}\right)^2 \left(\frac{\cos\beta\cos\theta_C}{\cos\alpha\cos\theta_F}\right)^3 \tag{4.25}$$

where θ_C and θ_F are the off-axis incident angles for the central ray on the collimating and focusing mirrors (see Fig. 4.8), α and β are the incidence and diffraction angles at the grating, and R_C and R_F are the radii of curvature of the collimating and focusing mirrors respectively.

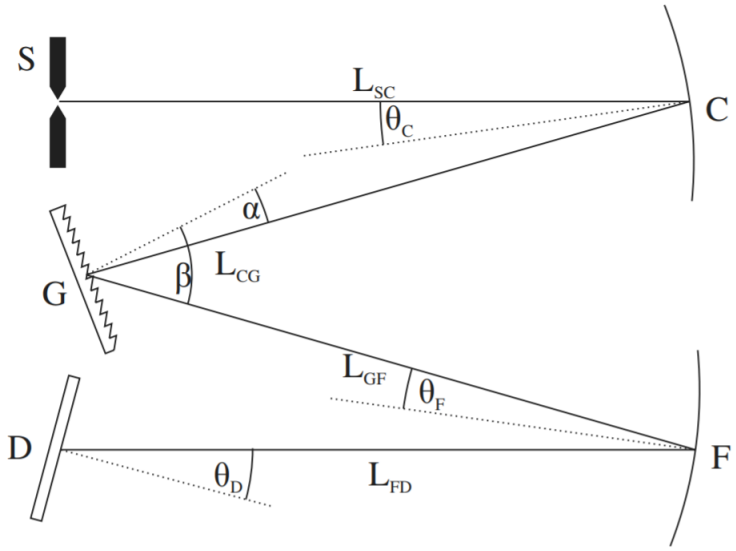

Figure 4.8: Classical Czerny-Turner spectrometer design with the collimating mirror C with angle of incidence in tangential plane θ_C and radius R_C and the focusing mirror F with angle of incidence in tangential plane θ_F and radius R_F. [86]

This condition is known as the Shafer equation. Typically, the off-axis angles remain quite small ($5° - 8°$ for θ_C and $\sim 10°$ for θ_F) so that the third-order term can be simplified to obtain the approximate relation, [87]

$$\frac{\sin\theta_C}{\sin\theta_F} = \left(\frac{R_C}{R_F}\right)^2 \left(\frac{\cos\beta}{\cos\alpha}\right)^3 \tag{4.26}$$

This means that the coma aberration can be corrected by adjusting the incident off-axis reflection angles θ_C and θ_F accordingly to fulfil Eq. 4.25.

4.5.2 Astigmatism

Another form of off-axis aberration is astigmatism. It is characterised by a variation of the focal length between the mirrors tangential and sagittal directions. Czerny-Turner spectrographs suffer from astigmatism, resulting from the off-axis reflections on the spherical mirrors. The focal distance to the tangential and sagittal image for a collimated beam reflected from a spherical surface is, [88]

$$f_{tn} = \frac{r_n}{2}\cos\theta_n + \Delta f_{tn} \tag{4.27}$$

$$f_{sn} = \frac{\rho_n}{2}\sec\theta_n + \Delta f_{sn} \tag{4.28}$$

with $n = 1, 2$, denoting the collimating and focusing mirrors. θ is the off-axis angle of the ray, Δf is the small distance added to the third-order approximation, and r and ρ are the radii of curvature in the tangential and sagittal plane respectively ($r = \rho$ for a spherical mirror). This means that astigmatism does not depends on wavelength but, rather, on the incident angles to the mirrors.

Several techniques have been studied to reduce astigmatism in broad-band spectrographs. For example, Xue et al. (2009) propose using a toroidal focusing mirror instead of a spherical one. The distinct radius of curvature between tangential and sagittal directions allows to correct for the difference in focal length between the two planes. Moreover, a toroidal mirror is particularly simple to make in comparison with other nonspherical surfaces. [87] In the same paper, they investigate the geometric relation between the distance L_{GF} (distance between the grating and the focusing mirror) and the incident angles to the focusing mirror for different wavelength. They found that when L_{GF} is equal to $2f_{t2}$, good imaging quality is obtained over the whole wavelength region. Xue also presents a design procedure to correct astigmatism by adding a tilted cylindrical lens between the focusing mirror and the detector. [89]

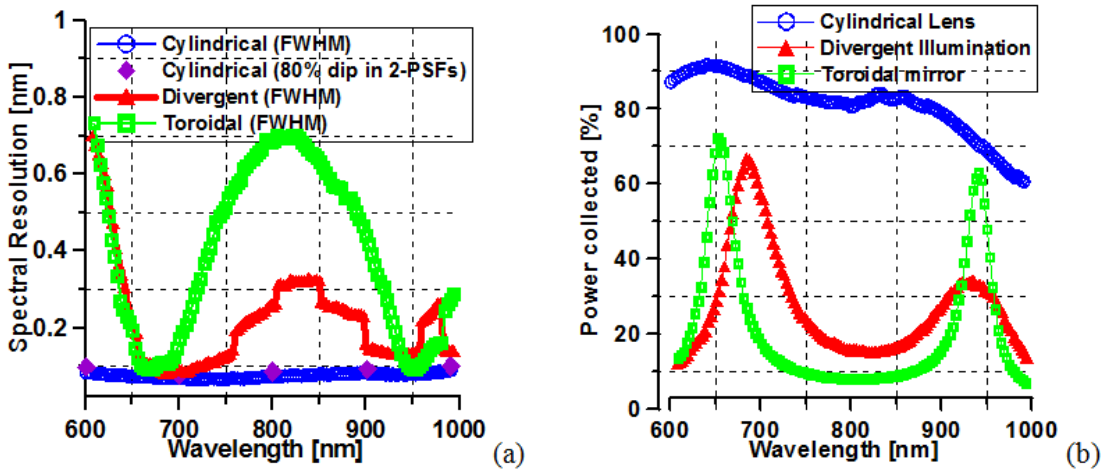

Figure 4.9: **(a)** Spectral resolutions based on the FWHM and **(b)** power percentage collected by a pixel array with 10 μm width for three spectrograph designs are presented. Each curve corresponds to a design for which one of the three astigmatism correction methods is implemented. Those are color-coded in the legend at the top of each graph. [90]

Another technique, proposed by Austin et al. (2009) and McDowell (1975), is to reduce the distance between the input slit and the collimating mirror so that the grating is under divergent illumination. This generates astigmatism that can compensate for the off-axis reflections from the spherical optics. [86] [91] The advantage of this method is that there is no need for additional optics while keep-

ing spherical surfaces. Finally, Lee et al. propose an optical design for a low-cost optics, broad-band, astigmatism-corrected spectrometer using a cylindrical lens. Additionally, they present a comparison of their design with the other solutions for astigmatism management and reduction (see Fig. 4.9) in the same conditions. [90] Results demonstrate an improvement of at least three times when compared to the other solutions.

Chapter 5

CODE V analysis

5.1 Code-V Implementation and Optimisation

Using the spectrograph parameters of the selected configuration presented in Tab. 4.3 together with the geometrical condition for coma correction established by Shafer, the design can be implemented in ray-tracing software for analysis and optimisation. This is performed with the optical design software CODE V. [92]

Different designs are investigated to find the optimal solution that meets the scientific requirements. This is done by first implementing a fairly simple design consisting of all-spherical mirrors. Then, different techniques are studied to reduce aberration (mainly astigmatism). As the preliminary design is optimised for only the centre wavelength, further automatic optimisation is performed by CODE V. This is done by varying the different parameters such as the distances between the different optics, the radii of curvature of the mirrors, and the position and tilt of the detector to match the focal plane. The main goal is to reduce the spot size below the airy disk size for the entire wavelength range. A design constraint has been specified for the spectral spreading on the detector to keep a resolution power of at least $R = 2000$ at the design wavelength.

5.1.1 Spherical mirrors design

First, two spherical mirrors are used for the collimator and camera. The grating is considered as a linear blazed grating with groove spacing $d = 1/G$ (G being the groove density). The layout of the design after optimisation is shown in Fig. 5.1. The initial and optimized values of the spectrograph parameters are compared in Tab. 5.1.

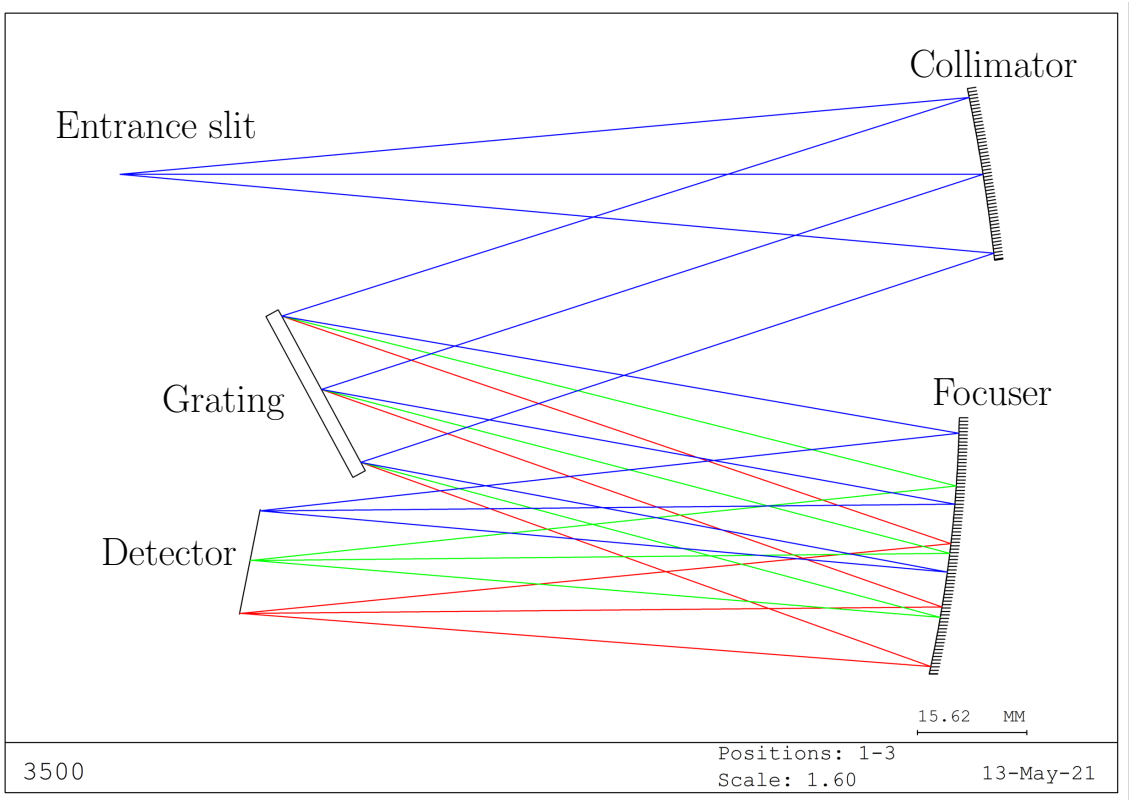

Figure 5.1: Geometrical representation of the design with two spherical mirrors to scale. The green ray corresponds to the central wavelength ($\lambda_c = 3.75\,\mu$m) while the red and blue rays are for $\lambda = 4\,\mu$m and $\lambda = 3.5\,\mu$m respectively.

Parameter	Calculated	Optimized
L_{GF} (mm)	85.5	83.25
L_{FD} (mm)	91.57	99.78
θ_C (°)	9	9
θ_F (°)	11.82	7
R_C (mm)	246.3	283.1
R_F (mm)	183.14	187.2

Table 5.1: Initial and optimised values of the spectrograph parameters defined in Fig. 4.8 for the spherical mirror design.

Most of the optimized values of the spectrograph parameters are in close agreement with the initial values computed with Matlab. However, it can be observed that the optimisation software tends to lower the incident off-axis angle on the

camera. Approaching the on-axis configuration by reducing θ_F is accompanied by a reduction of the off-axis aberration, mostly dominant astigmatism that the asymmetrical system induces. Nevertheless, it can be seen in Fig. 5.1 that the reduction of θ_F causes the detector to move closer to the grating, which could result in mechanical problems. Therefore, a trade-off must be made between reducing the aberrations and ensuring that enough spacing is provided between the optical components.

Spot size analysis

As previously mentioned, the optimisation process consists of reducing the spot size for the wavelengths defined in the ray-tracing software. These spot sizes for the optimised spherical mirror design are presented in Fig. 5.2.

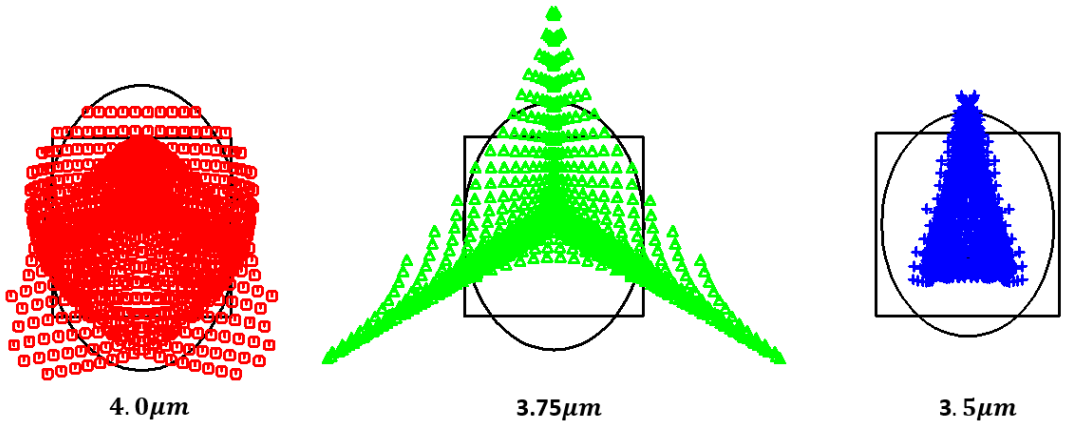

Figure 5.2: Spot sizes for the 3.5, 3.75 and 4.0 μm wavelengths for the spherical mirror design. A square of 36 $\times$ 36 μm (2 pixels) is represented for scale as well as the airy disk.

As expected, a design using only spherical mirrors suffers from aberrations. As a consequence, the spot sizes exceed the size of the airy disk, especially for the higher wavelengths. The system is thus limited by aberration and not by diffraction. Ideally, the spot sizes should be contained within the airy disk size such as to have a diffraction-limited system. The exact Root Mean Square (RMS) and 100% spot sizes for the different wavelengths of interests are tabulated in Tab. 5.1.

	3.5 μm	3.75 μm	4.0 μm
RMS spot size (μm)	21.24	39.28	31.09
100% spot size (μm)	40.76	97.53	60.73

Table 5.2: RMS (Root Mean Square) and 100% spot size for the 3.5, 3.75 and 4.0 μm wavelengths using spherical mirrors.

5.1.2 Aspherical mirror design

Although easier to manufacture, the use of spherical optics induces the presence of spherical aberration. This can be eliminated by making mirrors with an aspheric surface. The effect on spot size using an aspherical focusing mirror is therefore studied. This is done by starting from the fully spherical design and varying the conic constant of the second mirror as well as the higher-order coefficients. The resulting configuration is depicted in Fig. 5.3.

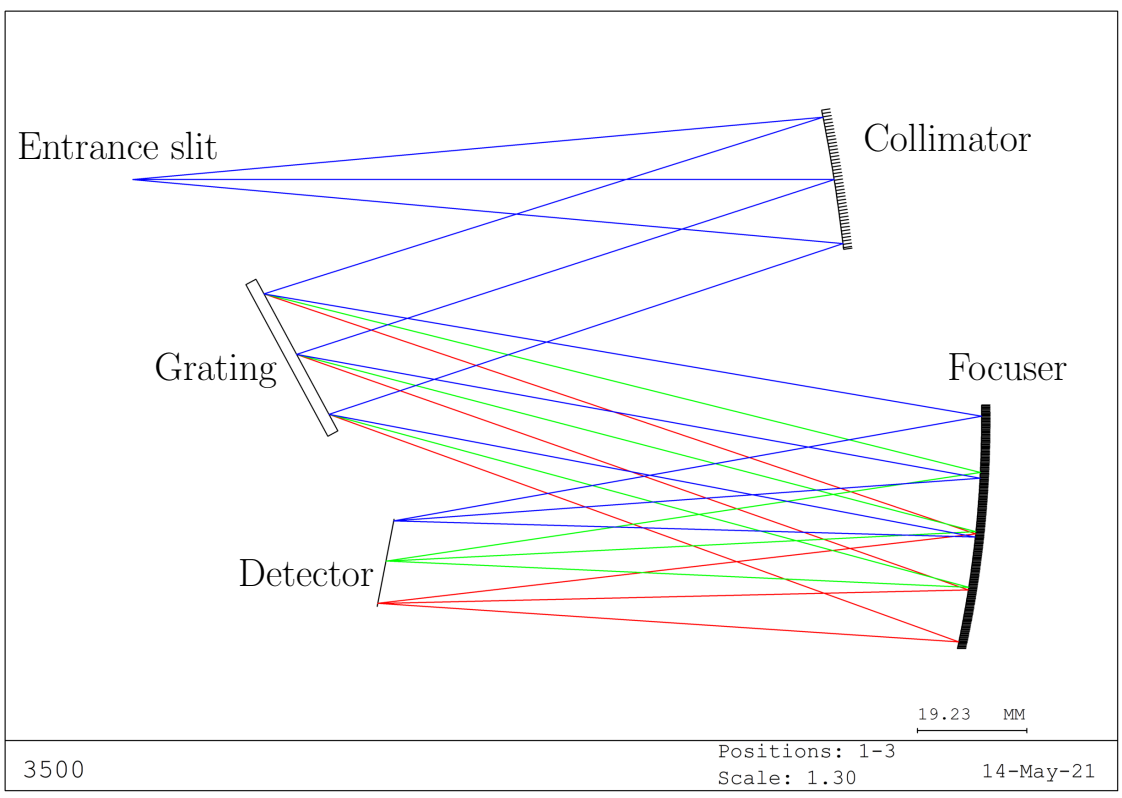

Figure 5.3: Geometrical representation of the design with an aspherical focusing mirror. The green ray corresponds to the central wavelength ($\lambda_c = 3.75\,\mu$m) while the red and blue rays are for $\lambda = 4\,\mu$m and $\lambda = 3.5\,\mu$m respectively.

Parameter	Calculated	Optimized
L_{GF} (mm)	85.5	100.97
L_{FD} (mm)	91.57	103.38
θ_C (°)	9	9
θ_F (°)	11.82	8.8
R_C (mm)	246.3	272.2
R_F (mm)	183.14	191.2
cc (mm)	0.0	0.0064

Table 5.3: Initial and optimised values of the spectrograph parameters defined in Fig. 4.8 for the aspherical mirror design with cc = conic constant.

The resulting optimised configuration is similar to the spherical one except it has been slightly increased in size. In fact, the distances between the different optical surfaces as well as the radius of curvature of the focusing mirror have increased. Moreover, the optimal value of the conic constant determined by the optimisation process of CODE-V has barely changed from the spherical configuration. Finally, the off-axis angle at the focusing mirror has been increased, allowing some additional room for the detector. The numerical data is presented in Tab. 5.3.

Spot size analysis

The spot sizes for this new configuration are illustrated in Fig. 5.4. The relative sizes between the different wavelengths have been equilibrated. It can be seen that the spot sizes of the two higher wavelengths (4.0 μm and 3.75 μm) have been slightly reduced while the size for the lower wavelength (3.5 μm) has increased. Although the spots now fit in the airy disk sizes for the two outer wavelengths, the centre wavelength is still spread over a too large area to fall within the requirements on resolution. Moreover, it is preferable to leave some margin of error for manufacturing tolerancing. As indicated by the numerical values in Tab. 5.3 , the spot sizes are still too large to validate the design.

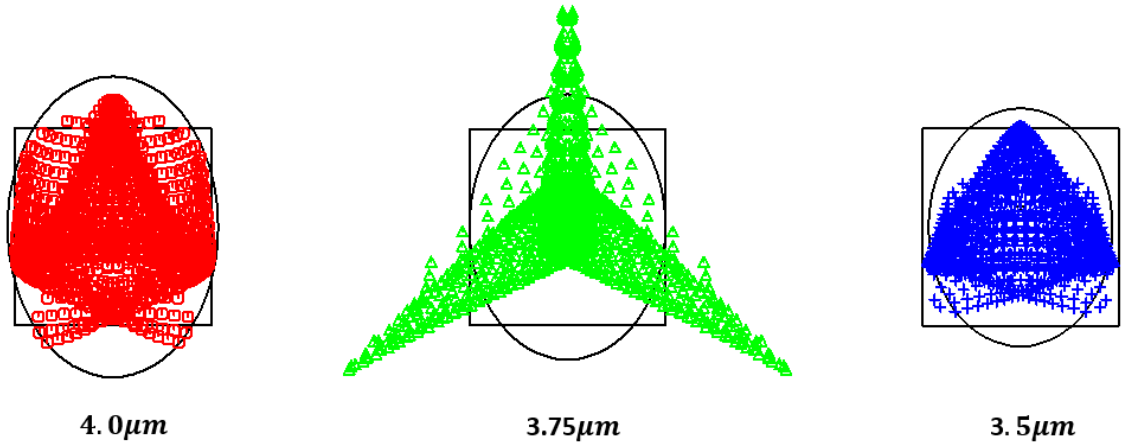

Figure 5.4: Spot sizes for the 3.5, 3.75 and 4.0 μm wavelengths for the aspherical mirror design. A square of 36 $\times$ 36 μm (2 pixels) is represented for scale as well as the airy disk.

	3.5 μm	3.75 μm	4.0 μm
RMS spot size (μm)	24.82	32.14	27.91
100% spot size (μm)	37.64	87.96	45.93

Table 5.4: RMS (Root Mean Square) and 100% spot size for the 3.5, 3.75 and 4.0 μm wavelengths using an aspherical focusing mirrors.

5.1.3 Toroidal mirror

Although it has caused some improvements, the use of an aspherical surface is not sufficient to reduce the off-axis aberrations caused by the Czerny-Turner configuration. The coma aberration can easily be corrected by adjusting the off-axis angles according to the Shafer condition described in Sec. 4.5.1. On the other hand, correction of astigmatism requires either an additional optical surface such as a cylindrical lens or the use of a toroidal focusing mirror. The latter is implemented into the ray-tracing software to study the impact on the system's performance. In fact, by optimising for the two radii of curvature in the sagittal and tangential plane of the toroidal mirror, astigmatism is expected to reduce significantly. The obtained configuration is shown in Fig. 5.5.

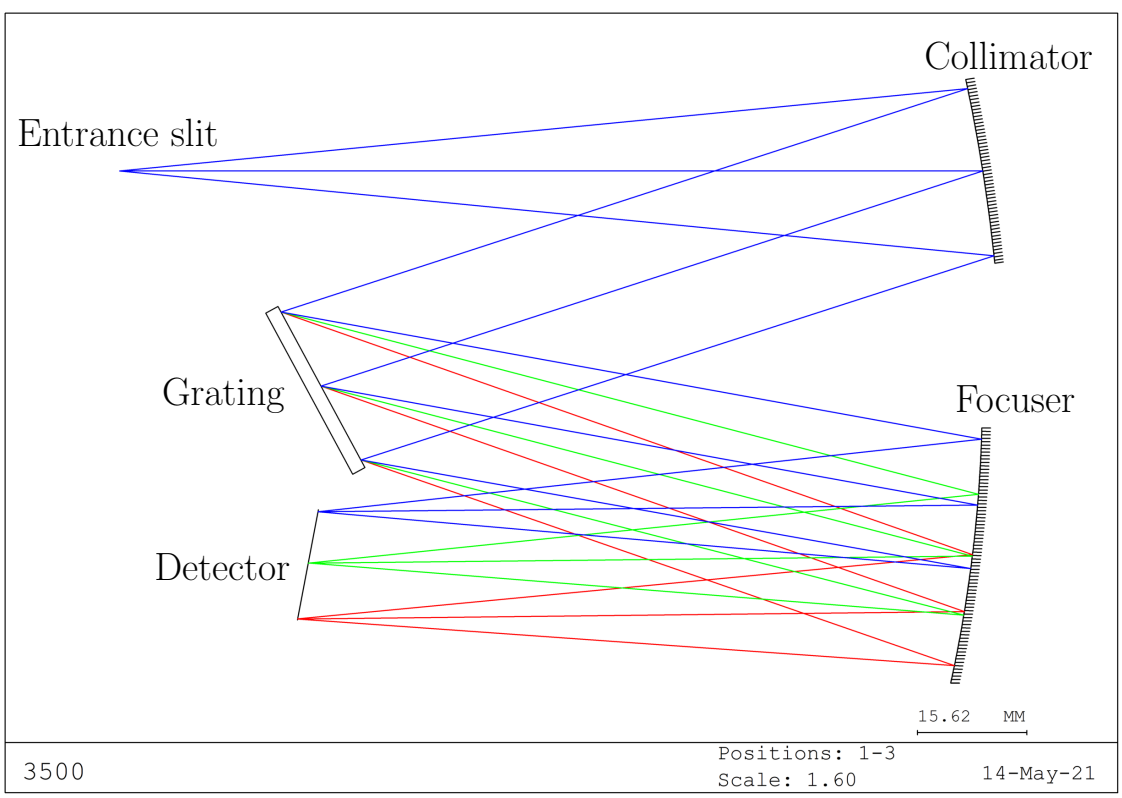

Figure 5.5: Geometrical representation of the design with a toroidal focusing mirror. The green ray corresponds to the central wavelength ($\lambda_c = 3.75\,\mu$m) while the red and blue rays are for $\lambda = 4\,\mu$m and $\lambda = 3.5\,\mu$m respectively.

Parameter	Calculated	Optimized
L_{GF} (mm)	85.5	80.0
L_{FD} (mm)	91.57	94.36
θ_C (°)	9	9
θ_F (°)	11.82	7.6
R_C (mm)	246.3	246.25
$R_{F,y}$ (mm)	183.14	190.2
$R_{F,x}$ (mm)	183.14	186.3

Table 5.5: Initial and optimised value of the spectrograph parameters defined in Fig. 4.8 for the toroidal focusing mirror design.

As for the initial spherical design, most of the optimized values of the spectrograph parameters are in close agreement with the initial values computed with

Matlab, providing a relatively compact configuration (see Tab. 5.5).

Spot size analysis

As shown in Fig. 5.6, the use of a toroidal focusing mirror significantly decreases the off-axis aberrations and therefore also the spot sizes. The two outer wavelengths (red and blue) are both contained within the Airy disk as well as within the 2 by 2-pixel square. Although the centre wavelength is slightly more spread, its energy is concentrated into a smaller spot. This can also be deduced from Tab. 5.5 as the centre wavelength has the largest 100% size but the smallest RMS spot size. Nevertheless, the configuration shown in Fig. 5.5 presents a small separation between the grating and detector which could cause some problem.

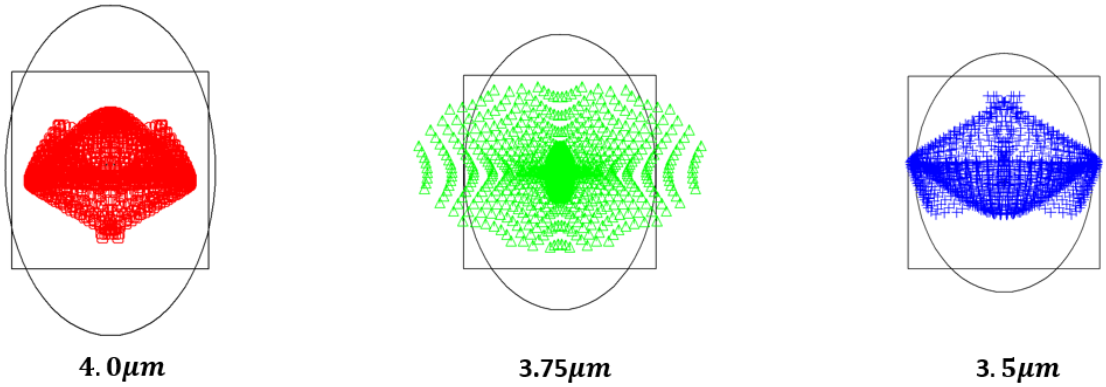

Figure 5.6: Spot sizes for the 3.5, 3.75 and 4.0 μm wavelengths for the toroidal mirror design. A square of 36 $\times$ 36 μm (2 pixels) is represented for scale as well as the airy disk.

	3.5 μm	3.75 μm	4.0 μm
RMS spot size (μm)	22.05	18.27	19.30
100% spot size (μm)	35.05	52.89	29.52

Table 5.6: RMS (Root Mean Square) and 100% spot size for the 3.5, 3.75 and 4.0 μm wavelengths using a toroidal focusing mirrors.

5.1.4 Toroidal mirror + cylindrical lens

Finally, to eliminate the problem of the small separation between detector and grating, a constraint on the minimum incident off-axis angle at the focusing mirror is added. However, this is accompanied by an increase of the off-axis aberrations, mainly astigmatism. Nonetheless, it also gives the possibility to insert

an additional optical surface into the configuration. Following the design procedures presented by Xue and Lee, a tilted cylindrical lens is added between the focusing mirror and detector. Moreover, this method is the most efficient for astigmatism reduction (see Fig. 4.9). For the implementation into CODE V, an off-the-shelf ZnSe cylindrical lens with a central thickness of 6 mm has been chosen. The design obtained after optimisation is shown in Fig. 5.7.

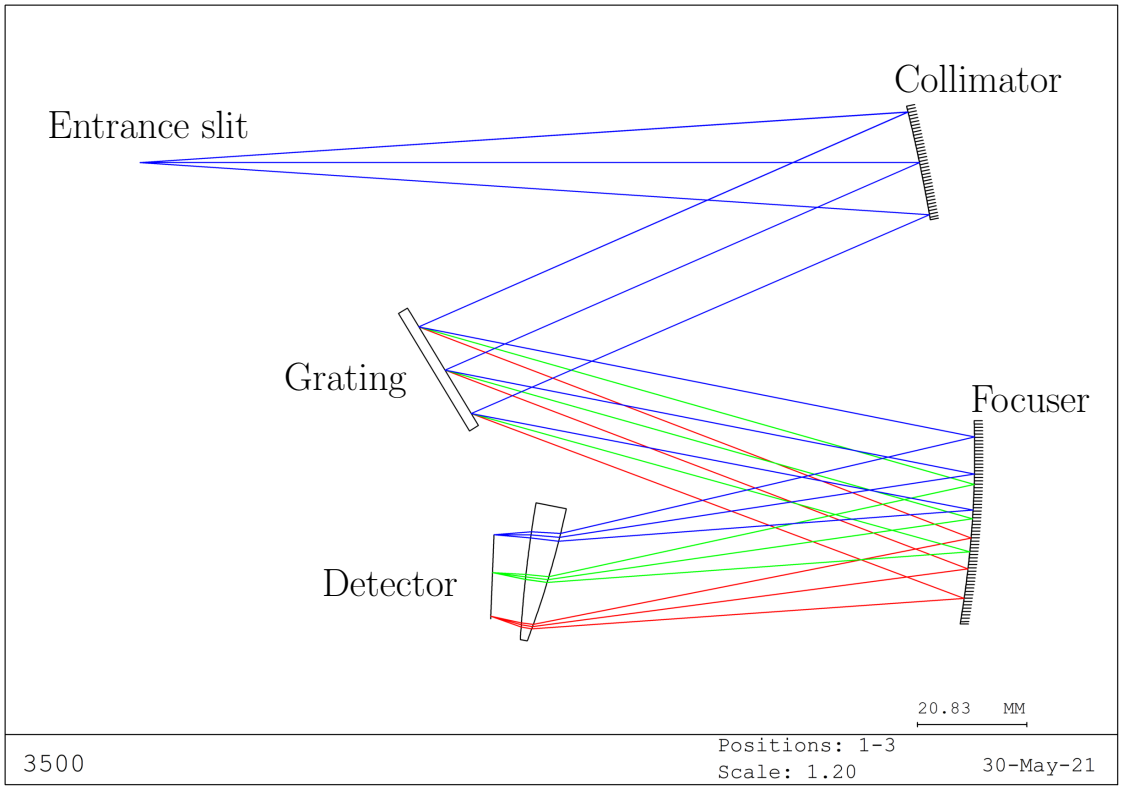

Figure 5.7: Geometrical representation of the design with a toroidal focusing mirror and a tilted cylindrical lens (ZnSe). The green ray corresponds to the central wavelength ($\lambda_c = 3.75\,\mu$m) while the red and blue rays are for $\lambda = 4\,\mu$m and $\lambda = 3.5\,\mu$m respectively.

Additionally to the other optimisations, the focal length of the collimator has been varied. Also, the off-axis angle on the collimator has been adapted to satisfy Shafer's condition (Eq. 4.25). The resulting optimised design is compared to the computed parameters in Tab. 5.7. Most values are relatively close to the computed values. The increased off-axis angle θ_F allows for more space between the detector and the grating to accommodate for the fixtures of these optical components.

Parameter	Calculated	Optimized
L_{GF} (mm)	85.5	80.0
L_{FL} (mm)	68.6	76.8
θ_C (°)	9	10.1
θ_F (°)	11.82	11.2
R_C (mm)	246.3	293.8
$R_{F,x}$ (mm)	183.14	174.53
$R_{F,y}$ (mm)	183.14	186.53

Table 5.7: Initial and optimised value of the spectrograph parameters defined in Fig. 4.8 for the design with a cylindrical lens. L_{FL} is the distance between the focusing mirror and the first surface of the cylindrical lens for the central ray.

Spot size analysis

As shown in Fig. 5.8, the use of an additional optical element significantly decreases the spot size for all wavelengths and especially for the centre wavelength. Moreover, both the RMS and 100% size are contained within the airy disk with some margin for alignment or manufacturing errors. The numerical results are displayed in Tab. 5.7. It can also be observed that the shape of the airy disk is particularly more elongated in the vertical direction. This asymmetry is explained by the off-axis nature of the system. The effect is reinforced by the increase of the incident angles at the mirrors θ_C and θ_F. More precisely, it means that the focal ratio of the design is slower (= higher f-number) in the vertical plane then in the horizontal plane. The impact on the encircled energy is described in the next section.

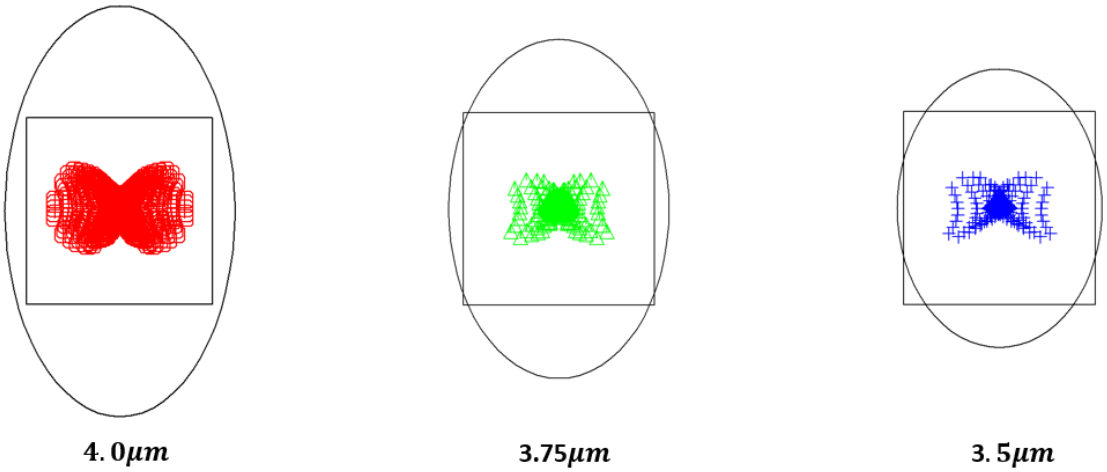

Figure 5.8: Spot sizes for the 3.5, 3.75 and 4.0 μm wavelengths for the toroidal mirror design with an additional cylindrical lens. A square of 36 $\times$ 36 μm (2 pixels) is represented for scale as well as the airy disk.

	3.5 μm	3.75 μm	4.0 μm
RMS spot size (μm)	6.85	6.36	7.49
100% spot size (μm)	22.40	20.21	23.55

Table 5.8: RMS (Root Mean Square) and 100% spot size for the 3.5, 3.75 and 4.0 μm wavelengths, using a toroidal focusing mirrors with a tilted cylindrical lens.

5.2 Encircled energy comparison

An encircled energy analysis is performed for the four presented designs. The encircled energy diameter computed from the Point Spread Function (PSF) and for a given field represents the diameter of a circle that encloses a specified percentage of the energy of the PSF.

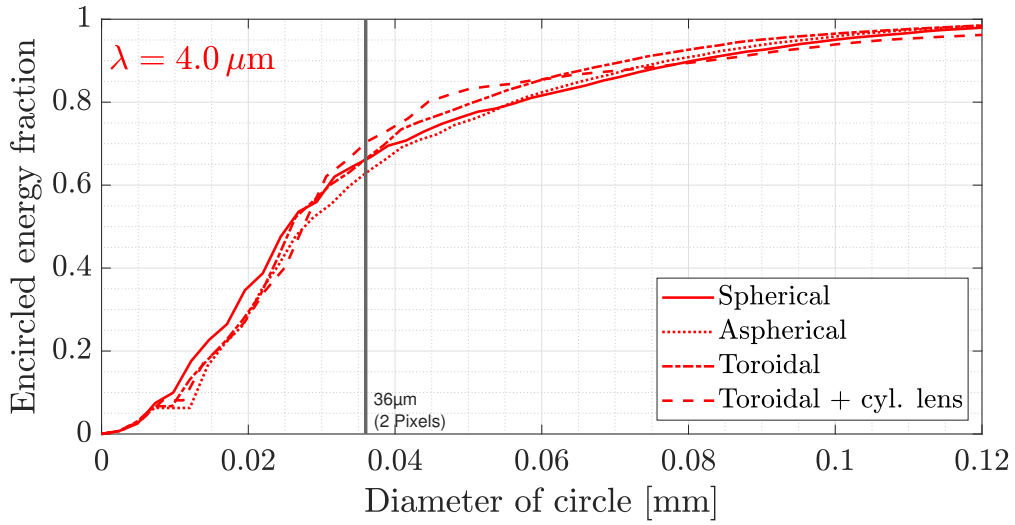

Figure 5.9: PSF based encircled energy comparison between the four presented designs for $\lambda = 4.0\,\mu$m. The encircled energy diameter represents the diameter of a circle that encloses a specified percentage of the energy centered on the PSF centroid.

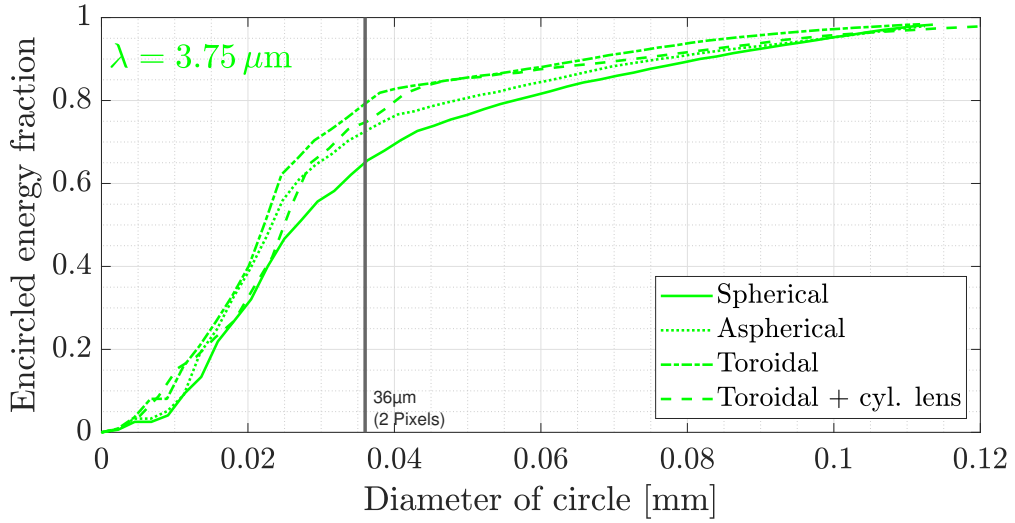

Figure 5.10: PSF based encircled energy comparison between the four presented designs for $\lambda = 3.75\,\mu$m. The encircled energy diameter represents the diameter of a circle that encloses a specified percentage of the energy centered on the PSF centroid.

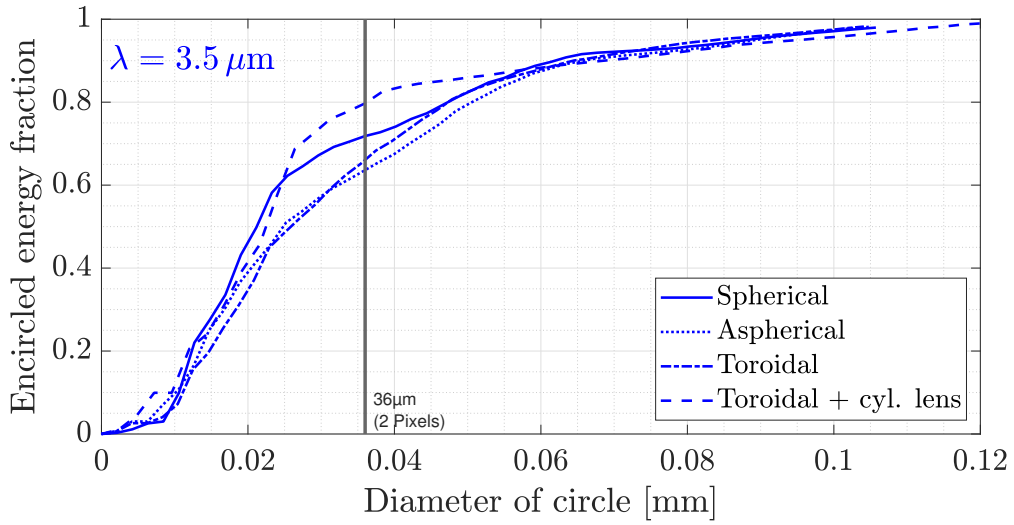

Figure 5.11: PSF based encircled energy comparison between the four presented designs for $\lambda = 3.5\,\mu$m. The encircled energy diameter represents the diameter of a circle that encloses a specified percentage of the energy centered on the PSF centroid.

The encircled energy for three relevant wavelengths (3.5, 3.75 and 4.0 μm) is plotted in Fig. 5.9, 5.10 and 5.11 respectively. It can be seen that the cylindrical lens design shows better performances, especially for the two border wavelengths (at 3.5 and 4.0 μm). Although the spot size of the centre wavelength (3.75 μm) has significantly decreased, the encircled energy between the toroidal focusing mirror design with and without the cylindrical lens show similar results. This can be explained by the fact that the system becomes diffraction-limited in the reduced spot size configuration (with a titled cylindrical lens). The encircled energy is then limited by the Airy disk size, which is slightly higher for the cylindrical lens design and compensates for the reduction of the spot size.

5.3 Performance verification

This section is dedicated to the analysis and verification of the performances of the cylindrical lens design. This is done along the spectral direction and through the slit, along the imaging direction. To do so, the fibre configuration at the entry slit has to be determined. As mentioned in Sec. 2.4 and illustrated in Fig. 2.17, the fibre bundle is rearranged in a line perpendicular to the dispersion direction to simulate a linear slit.

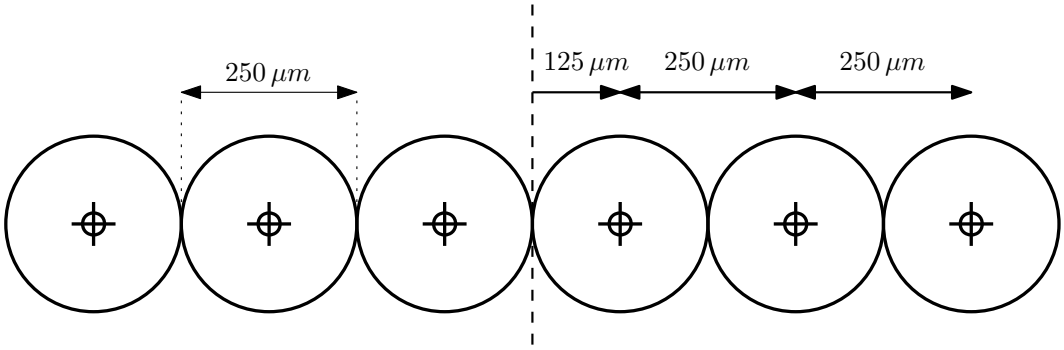

Figure 5.12: Selected fibre configuration along the imaging direction. The centre of the fibre cores are separated by 250 μm. The fibre pairs are symmetrically placed with respect to the vertical axis in the centre.

First of all, the separation between the fibres is constrained by their size. Typically, single-mode optical fibres have a core diameter between 8 and 10.5 μm. [93] Then, the cladding around the fibre core extends to approximately 125 μm. Additionally, a fibre coating might also be present, increasing the size of the fibre even more. However, the most important factor is the relative position of each fibre on the detector (see Sec. 5.3.2). To avoid overlapping of the spots, a separation of 250 μm between the fibre centres has been selected. The corresponding configuration for the 6 fibres is depicted in Fig. 5.12.

5.3.1 Spot size through slit

The fibre configuration shown in Fig. 5.12 is simulated by inserting additional fields in the imaging direction at the entry slit. The spot size is then analysed for these different fields, each associated with a fibre cable.

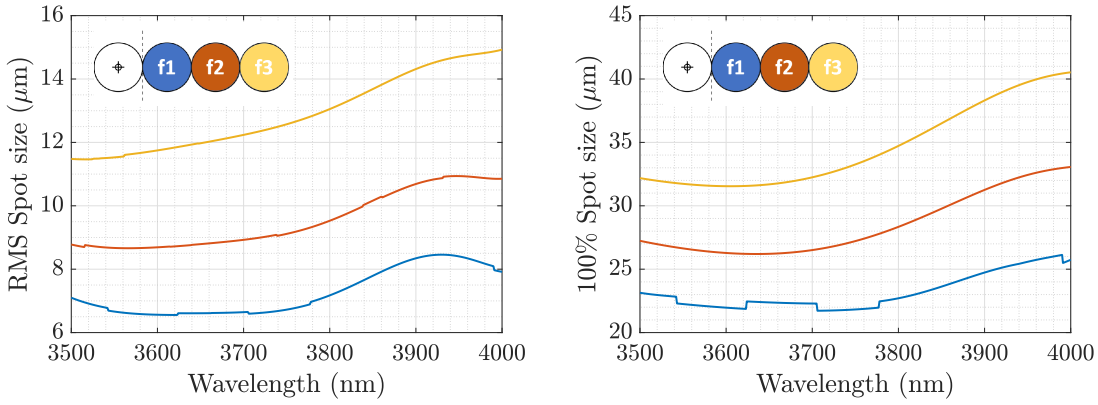

(a) (b)

Figure 5.13: **(a)** RMS spot size and **(b)** 100% spot size at the considered wavelength range for the corresponding fibres following the color code defined at the top left side of both graphs where the four rightmost fibres are represented.

The RMS and 100% spot size corresponding to each optical fibre cable is shown in Fig. 5.13a and b respectively. The symmetry with respect to the vertical axis shown in Fig. 5.12 is also observed in the spot sizes. This means that the sizes and shapes of the spots at equal distances along the horizontal direction are also equal. As this distance increases, the departure from the optical axis causes an increase in the spot size. However, these remain relatively small, keeping the design diffraction-limited at all wavelengths.

5.3.2 Position on the detector

The bidirectional position of the spots onto the focal plane is then analysed. The position along the imaging direction (defined as the X direction) for each fibre cable allows examining if the spots do not overlap. On the other hand, the position of each wavelength along the spectral direction (defined as the Y direction) gives the total size of the spectrum on the detector and allows the calculation of the linear dispersion (see Sec. 5.3.3).

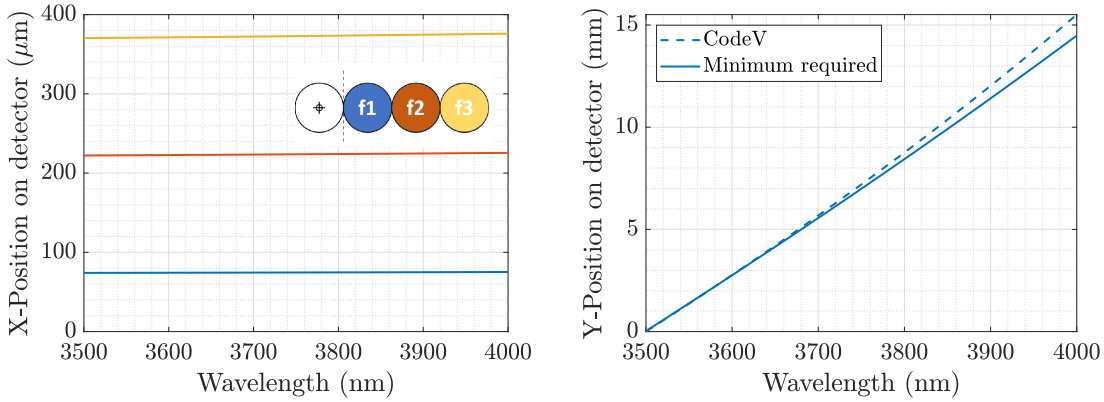

(a) (b)

Figure 5.14: **(a)** Position of the corresponding fibres in the imaging direction (along slit) w.r.t. the wavelength for the three leftmost fibres. **(b)** Position along the dispersion direction for all fibres and for each wavelength (the small variation between each fibre is neglected).

From Fig 5.14a, the separation between the images of the fibres can be deduced. Here, the detector is centred around $X = 0$ and only the positive side is depicted as the fibre configuration from Fig. 5.12 is perfectly symmetric. Note that there is an inversion of the image, meaning that a fibre cable at a positive X-position at the entry slit is imaged on a negative X-position on the detector. The distance between the images of each fibre is approximately 149.2 μm. This distance varies very slightly (a few microns) with the wavelength but can be considered negligible. Moreover, the separation between the images of the fibres in the imaging direction is sufficiently large to ensure that the spots do not overlap.

In Fig. 5.14b, the Y-position of each wavelength is depicted. The considered spectral band ($3.5 - 4.0\,\mu$m) is spread over 15.51 mm, slightly more than the required minimum size of 14.4 mm on the detector. There is a small variation of the Y-position between the different considered fields (only a few tenths of a micron) which is considered negligible. The bidirectional evaluation of the spots near the centre wavelength is depicted in Fig. 5.15 where a part of the focal plane of the instrument can be seen.

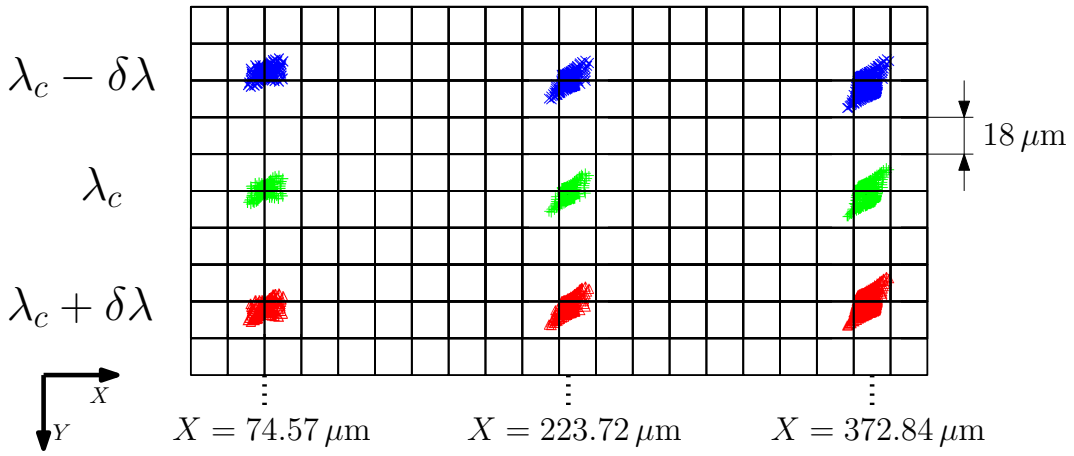

Figure 5.15: Part of the focal plane of the instrument is represented with an array of 18 μm pixels. The spots around the center wavelengths (λ_c) are represented at their corresponding X- and Y-positions ($\delta\lambda = 1.875$ nm).

5.3.3 Dispersion and resolving power

Finally, the linear dispersion on the detector is determined on the basis of the data obtained for the Y-position of each wavelength presented in Fig. 5.14b. As a matter of fact, the linear dispersion is obtained by the derivative of the curve,

$$D = \frac{\partial Y}{\partial \lambda} \tag{5.1}$$

This is computed by a central difference with a step size of $\Delta\lambda = 1\,\mu$m. The result is plotted in Fig. 5.16a and is compared to the theoretical value, calculated on the basis of Eq. 3.5.

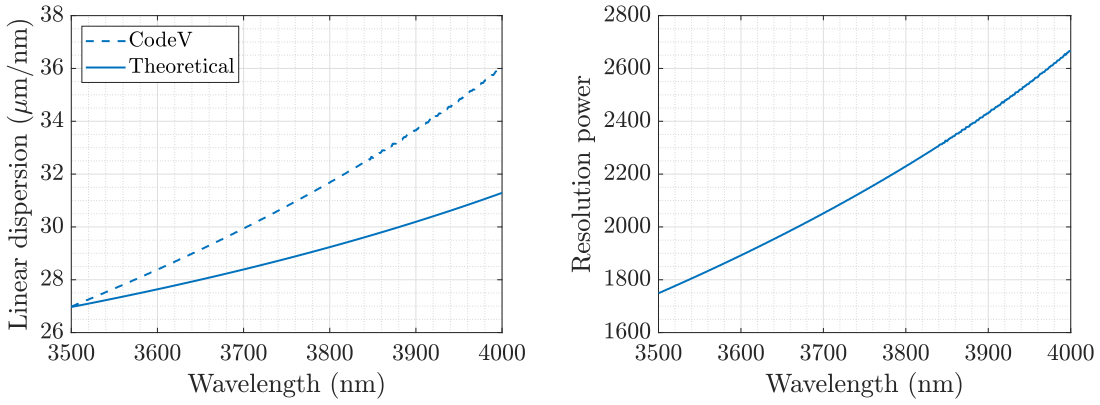

(a) (b)

Figure 5.16: **(a)** Linear dispersion of the cylindrical lens design compared with the theoretical value (Eq. 3.5). **(b)** Achieved resolving power of the spectrograph for each wavelength of the considered spectral band.

As expected, the linear dispersion of the CODE-V design is higher than the theoretical curve as the spectral band is dispersed over a wider region on the detector. This is accompanied by a higher resolving power at the design wavelength. In fact, the resolving power (R) is defined as,

$$R = \frac{\lambda}{\delta\lambda} \tag{5.2}$$

and is directly related to the linear dispersion. Considering a sampling over 3 pixels for each wavelength element $\delta\lambda$, the expression for the resolving power becomes,

$$R = \lambda \cdot \frac{\partial Y}{\partial \lambda} \cdot \frac{1}{3 \cdot p}$$

where p is the pixel size ($18\,\mu$m). The result for each wavelength is plotted in Fig. 5.16. The spectrograph reaches a resolving power of $R = 2138$ at the design wavelength which is slightly above the scientific requirements.

Chapter 6

Conclusion and perspectives

The first part of this work is dedicated to a global overview of ground-based spectroscopy. It was shown that the VLTI's infrared spectroscopic instruments cover a wide range of spectral bands. The wavelength range is expected to be extended even more by METIS, an in-development high-resolution instrument for the under-construction E-ELT. Also, several considerations related to ground-based spectroscopy were investigated. The different noise sources defining the atmospheric window have been identified to justify the considered wavelength range by the SCIFY project ($3.5 - 4.0\,\mu$m). Moreover, the properties of fibres were also studied as the correct use of these leads to increased instrument performance. Several advantages have been described as well as the most important limitations related to fibre-fed spectrographs. Finally, the available detector technologies were presented. For the considered wavelength range, MCT material has proven to be a good choice for the detector.

In Chapter 3, the theoretical background related to spectroscopy was presented. First, the different parameters describing a spectrograph were introduced. Secondly, The impact of each geometrical spectrograph parameter (mirror size, focal length, internal angle,...) on the performance as well as on the other optical elements has been qualitatively described. Eventually, the different existing spectrograph configuration and their history were introduced. This allowed identifying the main advantages and drawbacks of each configuration to provide selection criteria for the spectrograph design.

The optical design of the spectrograph is introduced in chapter 4. Starting from the scientific requirements, the different spectrograph parameters have been deduced. To explore the different possibilities in the design, a parametric analysis was performed. Similar observations to those of Bingham have been made. The choice of the configuration's geometry through the Blaze and Littrow angle has shown to be of paramount importance to obtain a robust design. The grating

was selected based on a review of the current grating manufacturers for the considered wavelength domain. This allowed obtaining a preliminary design based on the Czerny-Turner configuration, enabling high design flexibility. Also, the diffraction limitation on the airy disk size has been assessed. Finally, the off-axis aberrations introduced by the Czerny-Turner configuration were studied. A condition on the geometry of the system, known as the Shafer condition, has been fixed to correct for coma aberration. On the other hand, different astigmatism reduction methods proposed by several authors were compared.

In the last chapter, the implementation of the selected design into ray-tracing software CODE-V was described. Starting from a spherical mirror configuration, several designs were presented and optimised. The corresponding improvement induced after each subsequent modification was also analysed. As expected, the selected Czerny-Turner configuration suffers from off-axis aberration. Therefore, the camera was replaced by a toroidal mirror. Additionally, a cylindrical lens was introduced between the focusing mirror and the detector. Both astigmatism reduction techniques have shown to be effective as the spot size is below the Airy disk size for all considered wavelengths so that the system is diffraction-limited. The performances of the four presented designs were also analysed through the encircled energy, computed from the PSF. The tilted cylindrical lens configuration has shown to be the most performing design. The latter was finally used for the analysis of the image of the fibres. Their position on the detector together with the corresponding spot sizes allowed us to determine the linear dispersion as well as the obtained resolving power. The designed spectrograph reaches a resolving power of $R = 2138$ at the design wavelength, which is slightly above the goal requirement of 2000.

6.1 Perspectives for future work

Further improvement of the instrument has been considered by the SCIFY team. It consists of adding a Wollaston prism, which sends light with perpendicular polarization vectors in slightly different directions. This allows discriminating the not-polarized starlight from the polarized planetary light, increasing the dynamic range of the instrument. This has been implemented for the refractive spectrograph design considered by the SCIFY team. In continuation of this work, the analysis of the integration of a Wollaston prism in the reflective design may be the subject of a future study. Also, the study of a hybrid design should be investigated. Instead of using a reflective focusing mirror, a 3-lens camera as designed by the SCIFY team would reduce significantly the off-axis angle and therefore also the aberrations. This would be accompanied by a reduction of the asymmetry of the airy disk enabling better performance regarding the encircled energy.

Additionally, a calculation of the photometric budget of the spectrograph to evaluate the instrument's overall efficiency is required. In this regard, the fibre losses, coating reflectivity, grating efficiency and detector quantum efficiency have to be determined. Moreover, a deeper analysis of stray-light would enable an evaluation of the signal-to-noise ratio. Also, cross-talk between signals from different fibre cables and the impact on the PSF should be assessed. Finally, in the perspective of building the instrument, its thermo-mechanical behaviour must be investigated to improve the stability of the instrument.

Appendices

A Diffraction through a slit

For almost any astronomical observation, the light source is located at a very large distance or is virtually shifted into infinity by a lens. The far-field approximation can thus be applied. By considering that the incoming light is in a parallel beam, Fraunhofer diffraction occurs at the input slit. Mathematically, the intensity distribution of the electromagnetic wave across the observation screen is the integration of all elementary waves created by the slit. A two-dimensional rectangular slit $b_x \times b_y$ can be described by the product of two separate functions of two corresponding slit equations,

$$f(x) = \begin{cases} 1, & \text{for } x \leq b_x/2 \\ 0, & \text{for } x > b_x/2 \end{cases}$$

and

$$g(y) = \begin{cases} 1, & \text{for } y \leq b_y/2 \\ 0, & \text{for } y > b_y/2 \end{cases}$$

Then for the product $h(x,y) = f(x) \cdot g(y)$ the two-dimensional Fourier transform is obtained;

$$H(k_x,k_y) = \frac{1}{2\pi}\int_{-\infty}^{+\infty}\int_{-\infty}^{+\infty} h(x,y)e^{-i(xk_x+yk_y)}dxdy \tag{.1}$$

$$= \frac{1}{\sqrt{2\pi}}\int_{-\infty}^{+\infty} f(x)e^{-ixk_x}dx \cdot \frac{1}{\sqrt{2\pi}}\int_{-\infty}^{+\infty} g(y)e^{-iyk_y}dy \tag{.2}$$

$$= F(k_x) \cdot G(k_y) \tag{.3}$$

where the wave vectors k_x and k_y are defined as,

$$k_x = \frac{2\pi}{\lambda}\sin\theta_x$$
$$k_y = \frac{2\pi}{\lambda}\sin\theta_y$$

with θ_x and θ_y the angular positions behind the input slit. After integration, the Fourier transform becomes,

$$H(k_x,k_y) = \frac{b_1}{\sqrt{2\pi}}\frac{\sin(k_xb_x/2)}{k_xb_x/2} \cdot \frac{b_1}{\sqrt{2\pi}}\frac{\sin(k_yb_y/2)}{k_yb_y/2} \tag{.4}$$

Finally, the intensity $I(k_x,k_y)$ is the square of the absolute value of the amplitude and hence of the Fourier transform $H(k_x,k_y)$,

$$I(k_x,k_y) = |H(k_x,k_y)|^2 \tag{.5}$$

The intensity distribution is thus the square of the sinc function, the Fourier transform of the rectangular function. This is represented in Fig. 1

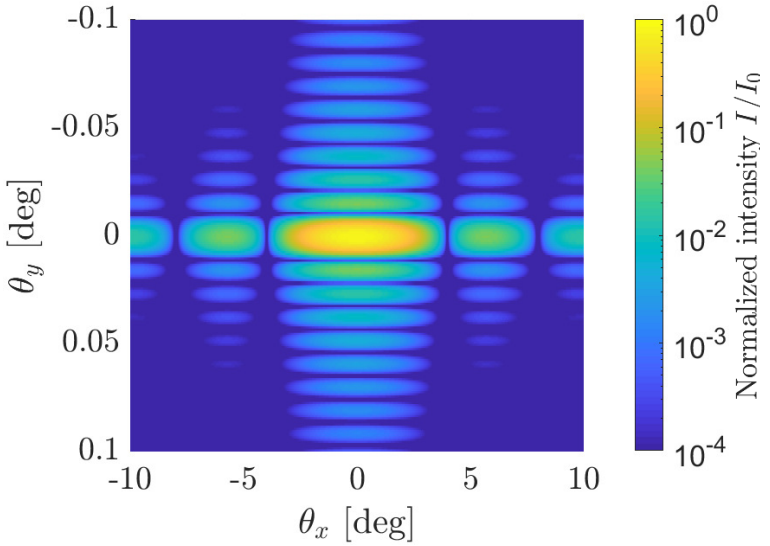

Figure 1: Normalized intensity distribution for a rectangular slit with $b_x = 54\,\mu$m and $b_y = 20$ mm and for $\lambda = 3.75\,\mu$m

The diffraction minima are located at,

$$\sin\theta_{x,min} = n_1 \cdot \frac{\lambda}{b_x} \tag{.6}$$

$$\sin\theta_{y,min} = n_2 \cdot \frac{\lambda}{b_y} \tag{.7}$$

with $n_1, n_1 = \pm 1, \pm 2, ...$ and the slit widths in the x and y direction b_x andb_y respectively. This allows identifying the cone of light in which the majority of the initial electromagnetic energy is contained.

B Diffraction at the grating

In the previous section, the Fraunhofer diffraction for a single slit was calculated. The calculation can be extended to a grating which is considered as a series of single slits whose diffraction patterns interfere with each other. For simplification, a one-dimensional grating consisting of N slits is considered. The grating is mathematically represented by the use of the Dirac δ-function.

$$f(x) \circledast \delta(x) \tag{.8}$$

For the general case of N slits separated with a distance d, the slit function is convoluted with the sum of all corresponding δ functions,

$$f_N = f(x) \circledast \sum_{n=0}^{N-1} \delta(x - nd) \tag{.9}$$

After convolution and by applying the Fourier transform of f_N,

$$F_N(k_x) = \frac{b}{\sqrt{2\pi}} \frac{\sin(k_x b/2)}{k_x b/2} \cdot \frac{1 - e^{-ik_x Nd}}{1 - e^{-ik_x d}} \tag{.10}$$

Again, the intensity function is obtained by squaring the amplitude,

$$\begin{aligned} I(k_x) &= |F_N(k_x)|^2 \\ &= I_0 \cdot \frac{\sin^2(k_x b/2)}{(k_x b/2)^2} \cdot \frac{\sin^2(k_x Nd/2)}{\sin^2(k_x d/2)} \end{aligned}$$

Assuming the slit width b to be infinitely narrow but transparent, the sinc^2 term becomes a constant value of unity. By considering the general case with an incident angle α at the grating and replacing the wave number component k_x accordingly gives the normalized intensity distribution for a one-dimensional grating,

$$\frac{I(\sin\alpha_x, \sin\beta_x)}{I(0)} = \frac{\sin^2(kNd/2(\sin\alpha_x + \sin\beta_x))}{N^2 \sin^2(kd/2(\sin\alpha_x + \sin\beta_x))} \tag{.11}$$

where $1/N^2$ is a normalization factor. The maxima of the function are located at,

$$\frac{kd}{2}(\sin\alpha + \sin\beta) = n\pi$$

with $n = 0, \pm 1, \pm 2, ...$ After simplification, the expression becomes the general grating equation (Eq. 3.1). The intensity distribution for the selected configuration is displayed in Fig. 2.

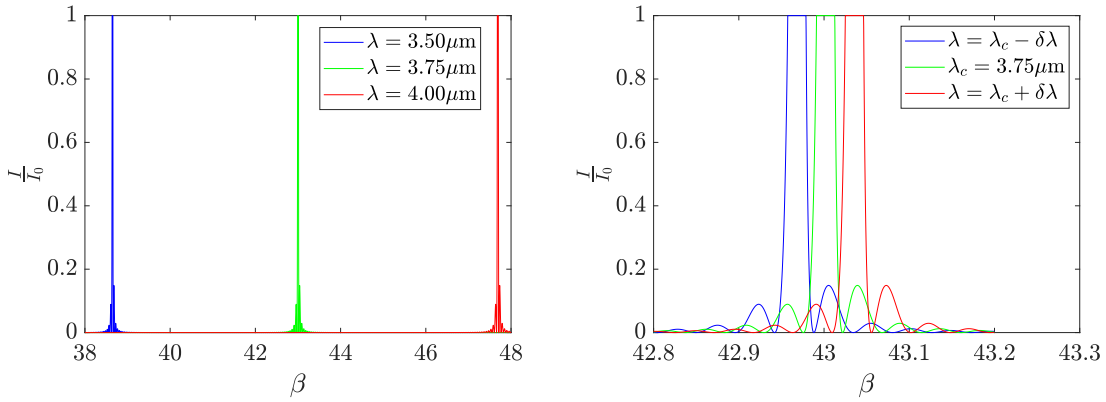

(a) (b)

Figure 2: Intensity distribution for the grating as function of the diffraction angle β for the selected configuration at the centre and border wavelengths in **(a)** while in **(b)**, the diffraction angle of the centre wavelength is compared with the neighbour wavelengths separated by $\delta\lambda = 1.875$ nm.

The constant height between each peak represents infinitely narrow grating grooves. In reality, grating grooves have a finite width and provide a modulating slit function, in addition to the intensity function. This ensures that the intensity of the individual orders decreases with the order number.

C Grating efficiency

Blazed diffractive gratings are widely used as a dispersing element in spectrographs because of their high efficiency. In fact, for a given diffraction order, it is optimised to achieve maximum grating efficiency at the blaze wavelength associated with the blaze angle of the grating. This allows concentrating the optical power around the wavelength of interest in the desired diffraction order while minimizing the residual power in the other orders. However, in contrast to prisms, blazed gratings do not show a constant efficiency over the wavelength range.

By applying the theory of grating diffraction to the blazed grating, the Blaze function can be obtained. It corresponds to the efficiency distribution which determines the efficiency for the order maxima. it is expressed as, [94]

$$B(\alpha, \beta, \theta_B) = \left[\frac{\sin(\frac{1}{\lambda} \cdot \pi \cdot d \cdot (\sin(\alpha - \theta_B) + \sin(\beta - \theta_B)))}{\frac{1}{\lambda} \cdot \pi \cdot d \cdot (\sin(\alpha - \theta_B) + \sin(\beta - \theta_B))} \right]^2 \tag{.12}$$

The blaze function has its maximum when the argument of the sinc function vanishes, so when,

$$\sin(\alpha - \theta_B) = \sin(\theta_B - \beta)$$

and hence,

$$\frac{\alpha + \beta}{2} = \theta_B \tag{.13}$$

This means that the blaze function has its maximum where the average of the incidence and diffraction angle is equal to the blaze angle θ_B. For the selected off-the-shelf grating with a groove density of 230 gr/mm and a blaze angle of 26.7°, the theoretical efficiency curves for the first 4 order are displayed in Fig. 3.

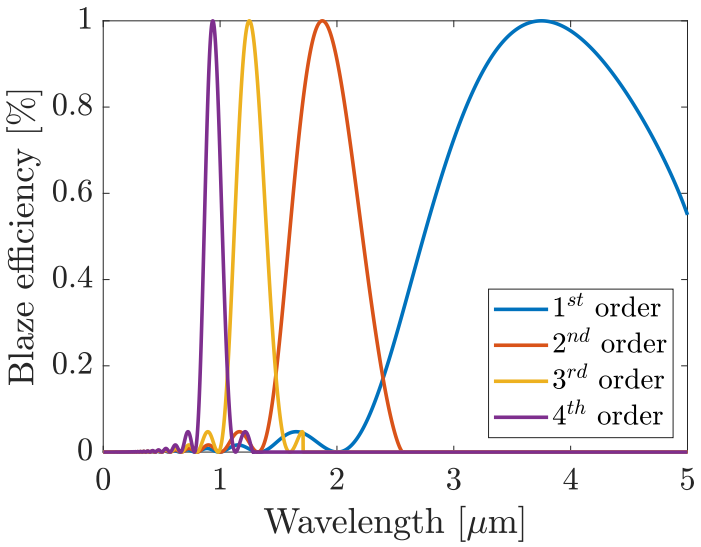

Figure 3: Computed blaze efficiency according to Eq. .12 for the selected grating ($G = 230$ gr/mm, $\theta_B = 26.7°$)

It can be seen that the spectral distance (and therefore also the geometrical distance) between the orders decrease with the diffraction order n. In practice, this is accompanied by a decrease in the light intensity respectively. Moreover, a ruled grating is produced by physically forming the grooves on a reflective surface by using a diamond tool mounted on a ruling engine. [95] This manufacturing process induces a peak round-off, degrading the efficiency of the grating. Typically, grating manufacturers achieve 90% of the theoretical groove depth.

References

[1] Schneider J. *Interactive Extra-solar Planets Catalog*. 2019. http://exoplanet.eu/catalog/ (cit. on pp. 1, 2).

[2] NASA Exoplanet Archive. *Exoplanets and candidates statistics*. 2019. https://exoplanetarchive.ipac.caltech.edu/docs/counts_detail.html (cit. on pp. 1, 3).

[3] J. T. WrightDr. and B. S. GaudiAssociate Professor. "Exoplanet Detection Methods". In: *Planets, Stars and Stellar Systems: Volume 3: Solar and Stellar Planetary Systems*. Ed. by T. D. Oswalt, L. M. French, and P. Kalas. Dordrecht: Springer Netherlands, 2013, pp. 489–540. ISBN: 978-94-007-5606-9. DOI: 10.1007/978-94-007-5606-9_10. https://doi.org/10.1007/978-94-007-5606-9_10 (cit. on p. 2).

[4] Wikipedia. *Fermi paradox — Wikipedia, The Free Encyclopedia*. https://en.wikipedia.org/wiki/Fermi_paradox. [Online; accessed 25-May-2021]. 2021 (cit. on p. 2).

[5] M. Perryman. "The History of Exoplanet Detection". In: *Astrobiology* 12.10 (2012). PMID: 23013272, pp. 928–939. DOI: 10.1089/ast.2011.0784. https://doi.org/10.1089/ast.2011.0784 (cit. on p. 2).

[6] E. Gibney and D. Castelvecchi. "Physics Nobel goes to exoplanet and cosmology pioneers". In: *Nature* 574.7777 (Oct. 2019), pp. 162–162. DOI: 10.1038/d41586-019-02964-z. https://doi.org/10.1038/d41586-019-02964-z (cit. on p. 2).

[7] *NASA's Kepler Mission Announces a Planet Bonanza, 715 New Worlds*. 2015. \url{}https://www.nasa.gov/ames/kepler/nasas-kepler-mission-announces-a-planet-bonanza (cit. on p. 2).

[8] G. Anglada-Escudé et al. "A terrestrial planet candidate in a temperate orbit around Proxima Centauri". In: *Nature* 536.7617 (Aug. 2016), pp. 437–440. DOI: 10.1038/nature19106. https://doi.org/10.1038/nature19106 (cit. on p. 2).

[9] F. Selsis. "The Atmosphere of Terrestrial Exoplanets: Detection and Characterization". In: 321 (Nov. 2004), p. 170 (cit. on p. 3).

[10] D. Defrère. "Characterizing extrasolar planetary systems using infrared interferometry". PhD thesis. University of Liège, 2009 (cit. on pp. 3, 6, 7).

[11] C. Harman. *Habitable zone diagram*. https://commons.wikimedia.org/w/index.php?curid=64107813 (cit. on p. 5).

[12] J. Wang and C. Jurgenson. "Exoplanet Sciences with Nulling Interferometers and a Single-mode Fiber-fed Spectrograph". In: *The Astronomical Journal* 160.5 (2020), p. 210. ISSN: 1538-3881. DOI: 10.3847/1538-3881/abb5a3. http://dx.doi.org/10.3847/1538-3881/abb5a3 (cit. on p. 6).

[13] R. N. Bracewell and R. H. MacPhie. "Searching for nonsolar planets". In: *Icarus* 38.1 (1979), pp. 136–147. ISSN: 0019-1035. DOI: https://doi.org/10.1016/0019-1035(79)90093-9. https://www.sciencedirect.com/science/article/pii/0019103579900939 (cit. on p. 6).

[14] O. Absil. "Astrophysical studies of extrasolar planetary systems using infrared interferometric techniques". In: (Mar. 2006) (cit. on p. 6).

[15] D. Defrère. "Self-Calibrrated Interferometry For exoplanet spectroscopY". In: (2020). DOI: 10.5281/ZENODO.4249889. https://zenodo.org/record/4249889 (cit. on pp. 7, 17).

[16] D. Defrère et al. "Hi-5: a potential high-contrast thermal near-infrared imager for the VLTI". In: *Optical and Infrared Interferometry and Imaging VI*. Ed. by M. J. Creech-Eakman, P. G. Tuthill, and A. Mérand. Vol. 10701. International Society for Optics and Photonics. SPIE, 2018, pp. 223 –237. DOI: 10.1117/12.2313700. https://doi.org/10.1117/12.2313700 (cit. on p. 7).

[17] European Southern Observatory. *Very Large Telescope The world's most advanced visible-light astronomical observatory*. https://www.eso.org/public/unitedkingdom/teles-instr/paranal-observatory/vlt/?lang (cit. on p. 9).

[18] European Southern Observatory. *Very Large Telescope*. https://commons.wikimedia.org/w/index.php?curid=8002756 (cit. on p. 10).

[19] European Southern Observatory. *MIDI Instrument Characteristics*. 2013. https://www.eso.org/sci/facilities/paranal/decommissioned/midi/inst.html (cit. on p. 10).

[20] U. Grothkopf et al. *Basic ESO Publication Statistics*. en. Tech. rep. 2021. DOI: 10.18727/DOCS/1. http://doi.eso.org/10.18727/docs/1 (cit. on pp. 10, 11).

[21] European Southern Observatory. *AMBER Instrument Description*. 2016. https://www.eso.org/sci/facilities/paranal/decommissioned/amber/inst.html (cit. on p. 11).

[22] Gravity Collaboration et al. "First light for GRAVITY: Phase referencing optical interferometry for the Very Large Telescope Interferometer". In: 602, A94 (June 2017), A94. DOI: 10.1051/0004-6361/201730838. arXiv: 1705.02345 [astro-ph.IM] (cit. on p. 12).

[23] B. Lopez et al. "An Overview of the MATISSE Instrument — Science, Concept and Current Status". In: *The Messenger* 157 (Sept. 2014), pp. 5–12 (cit. on p. 13).

[24] ESO. *The E-ELT construction proposal*. http://dag-tr.org/uploads/Ekip/EELT.Constr.Proposal.pdf. (Accessed on 06/01/2021) (cit. on p. 14).

[25] B. R. Brandl et al. "METIS: the Mid-infrared E-ELT Imager and Spectrograph". In: *Ground-based and Airborne Instrumentation for Astronomy II* (2008). Ed. by I. S. McLean and M. M. Casali. DOI: 10.1117/12.789241. http://dx.doi.org/10.1117/12.789241 (cit. on p. 14).

[26] B. R. Brandl et al. "METIS: A Mid-infrared E-ELT Imager and Spectrograph". In: *Ground-based and Airborne Instrumentation for Astronomy II* (20010). Ed. by I. S. McLean and M. M. Casali. DOI: 10.1117/12.789241. https://www.eso.org/sci/publications/messenger/archive/no.140-jun10/messenger-no140-30-31.pdf (cit. on p. 15).

[27] *Infrared Spectroscopy*. 2020. https://chem.libretexts.org/@go/page/1847 (cit. on pp. 16, 24).

[28] F. Selsis, L. Kaltenegger, and J. Paillet. "Terrestrial exoplanets: diversity, habitability and characterization". In: *Physica Scripta Volume T* 130, 014032 (Aug. 2008), p. 014032. DOI: 10.1088/0031-8949/2008/T130/014032 (cit. on pp. 17, 18).

[29] L. Tremblay et al. "The Detectability and Constraints of Biosignature Gases in the Near- and Mid-infrared from Transit Transmission Spectroscopy". In: *The Astronomical Journal* 159.3 (2020), p. 117. ISSN: 1538-3881. DOI: 10.3847/1538-3881/ab64dd. http://dx.doi.org/10.3847/1538-3881/ab64dd (cit. on p. 18).

[30] E. W. Schwieterman et al. "Exoplanet Biosignatures: A Review of Remotely Detectable Signs of Life". In: *Astrobiology* 18.6 (June 2018), pp. 663–708. DOI: 10.1089/ast.2017.1729. arXiv: 1705.05791 [astro-ph.EP] (cit. on p. 18).

[31] F. Patat. *The Brightness of the Night Sky*. http://www.eso.org/~fpatat/science/skybright/ (cit. on pp. 21, 22).

[32] F. Falchi et al. "The new world atlas of artificial night sky brightness". In: *Science Advances* 2.6 (2016). DOI: 10.1126/sciadv.1600377. eprint: https://advances.sciencemag.org/content/2/6/e1600377.full.pdf. https://advances.sciencemag.org/content/2/6/e1600377 (cit. on p. 21).

[33] Patat, F. "UBVRI night sky brightness during sunspot maximum at ESO-Paranal ***". In: *A&A* 400.3 (2003), pp. 1183–1198. DOI: 10.1051/0004-6361:20030030. https://doi.org/10.1051/0004-6361:20030030 (cit. on p. 22).

[34] S. F. Sánchez et al. "The Night Sky at the Calar Alto Observatory II: The Sky at the Near-infrared". In: *Publications of the Astronomical Society of the Pacific* 120.873 (2008), pp. 1244–1254. DOI: 10.1086/593981. https://doi.org/10.1086/593981 (cit. on p. 22).

[35] S. Stuke. "Characterizing thin clouds using aerosol optical depth information". PhD thesis. Nov. 2016 (cit. on p. 23).

[36] GSP216. *Atmospheric Scattering*. http://gsp.humboldt.edu/OLM/Courses/GSP_216_Online/lesson2-1/scatter.html (cit. on p. 23).

[37] A. Cox, A. DeWeerd, and J. Linden. "An experiment to measure Mie and Rayleigh total scattering cross sections". In: *American Journal of Physics* 70 (2002), pp. 620–625 (cit. on p. 23).

[38] D. Lopes and A. Ramires Fernandes. "Atmospheric Scattering -State of the Art". In: Nov. 2014 (cit. on p. 24).

[39] Weather Edge Inc. *Atmospheric Scattering*. http://www.severewx.com/Radiation/scattering.html (cit. on p. 24).

[40] A. Alkholidi and K. S. Altowij. "Free Space Optical Communications - Theory and Practices". In: 2014 (cit. on p. 24).

[41] "Chapter 3 - Absorption and Scattering of Solar Radiation in the Atmosphere". In: *An Introduction to Atmospheric Radiation*. Ed. by K. Liou. Vol. 84. International Geophysics. Academic Press, 2002, pp. 65–115. DOI: https://doi.org/10.1016/S0074-6142(02)80018-3. https://www.sciencedirect.com/science/article/pii/S0074614202800183 (cit. on p. 25).

[42] "SCIAMACH Handbook version 2". In: ESA Earth Online. Chap. Chapter 5 - From Radiation Fields to Atmospheric Concentrations – Introduction into the Retrieval of Geophysical Parameters (cit. on p. 25).

[43] R. C. Smith. "Astrophysical Techniques, Sixth Edition, by C.R.Kitchin". In: *Contemporary Physics* 55.4 (2014), pp. 359–360. DOI: 10.1080/00107514.2014.948932. eprint: https://doi.org/10.1080/00107514.2014.948932. https://doi.org/10.1080/00107514.2014.948932 (cit. on pp. 25, 26).

[44] J. G. Cuby, D. Bottini, and J. P. Picat. "Handling atmospheric dispersion and differential refraction effects in large-field multiobject spectroscopic observations". In: *Optical Astronomical Instrumentation*. Ed. by S. D'Odorico. Vol. 3355. Society of Photo-Optical Instrumentation Engineers (SPIE) Conference Series. July 1998, pp. 36–47. DOI: 10.1117/12.316769 (cit. on p. 26).

[45] A. V. Filippenko. "The importance of atmospheric differential refraction in spectrophotometry". In: *Publications of the Astronomical Society of the Pacific* 94 (1982), p. 715. DOI: 10.1086/131052. https://doi.org/10.1086/131052 (cit. on p. 26).

[46] R. H. Donnelly et al. “The implications of atmospheric effects for fiber-fed spectroscopy”. In: *Publications of the Astronomical Society of the Pacific* 101 (1989), p. 1046. DOI: 10.1086/132572. https://doi.org/10.1086/132572 (cit. on p. 26).

[47] “Concepts of Classical Optics”. In: Freeman & Co., 1958. Chap. Appendix N (cit. on p. 26).

[48] E. N. Hubbard, J. R. P. Angel, and M. S. Gresham. “Operation of a long fused silica fiber as a link between telescope and spectrograph.” In: 229 (May 1979), pp. 1074–1078. DOI: 10.1086/157041 (cit. on p. 26).

[49] J. Hearnshaw. *Astronomical Spectrographs and their History*. Cambridge University Press, 2009. DOI: 10.1017/CBO9780511735288 (cit. on pp. 26, 29).

[50] T. Cabral. “A First Approach to Structural Health Monitoring of Adhesive Bonded Joints in Pipelines Using Integrated Fiber Optic Sensors”. PhD thesis. Nov. 2016. DOI: 10.13140/RG.2.2.10258.25283 (cit. on p. 27).

[51] R. Paschotta. *article on 'fiber core' in the Encyclopedia of Laser Physics and Technology, 1*. https://www.rp-photonics.com/fiber_core.html (cit. on p. 28).

[52] A. Al-Azzawi. *Fiber optics: Principles and advanced practices, second edition*. Jan. 2017, pp. 1–448. DOI: 10.1201/9781315154619 (cit. on p. 28).

[53] F. Aït Hocine. “Master thesis and internship[BR]- Master’s Thesis : Coupling of a single-mode fiber with a deformable mirror in a space-based nulling interferometer[BR]- Internship (linked to master’s thesis)”. MA thesis. University of Liège, 2020. \url{https://matheo.uliege.be/handle/2268.2/10470} (cit. on pp. 28, 29).

[54] M. Mayor et al. “Setting New Standards with HARPS”. In: *The Messenger* 114 (Dec. 2003), pp. 20–24 (cit. on p. 29).

[55] L. Pasquini et al. “Installation and commissioning of FLAMES, the VLT Multifibre Facility”. In: *The Messenger* 110 (Dec. 2002), pp. 1–9 (cit. on p. 30).

[56] O. Le Fèvre et al. “Commissioning and performances of the VLT-VIMOS instrument”. In: *Instrument Design and Performance for Optical/Infrared Groundbased Telescopes*. Ed. by M. Iye and A. F. M. Moorwood. Vol. 4841. Society of Photo-Optical Instrumentation Engineers (SPIE) Conference Series. Mar. 2003, pp. 1670–1681. DOI: 10.1117/12.460959 (cit. on p. 30).

[57] Ovejabiennegra. *Advantages and drawbacks of optical fibres in astronomical instrumentation*. 2009. https://spectroscopy.wordpress.com/2009/02/27/advantages-and-drawbacks-of-optical-fibres-in-astronomical-instrumentation/ (cit. on p. 30).

[58] W. W. Craig, C. J. Hailey, and J. P. Brodie. “Measurement of fibers to be used in fiber fed spectroscopy.” In: *Fiber Optics in Astronomy*. Ed. by S. C. Barden. Vol. 3. Astronomical Society of the Pacific Conference Series. Jan. 1988, pp. 41–51 (cit. on p. 31).

[59] S. Barden. "Review of Fiber-Optic Properties for Astronomical Spectroscopy". In: 152 (Jan. 1998), p. 14. DOI: 10.1117/12.211837 (cit. on pp. 31, 33).

[60] L. 2000. *Loss of intensity between input and output*. https://www.laser2000.co.uk/applications/optical-return-loss-in-networks (cit. on p. 31).

[61] L. W. Ramsey. "Focal ratio degradation in optical fibers of astronomical interest." In: *Fiber Optics in Astronomy*. Ed. by S. C. Barden. Vol. 3. Astronomical Society of the Pacific Conference Series. Jan. 1988, pp. 26–39 (cit. on p. 32).

[62] W. D. Heacox. "Radial image transfer by cylindrical, step-index optical waveguides". In: *J. Opt. Soc. Am. A* 4.3 (1987), pp. 488–493. DOI: 10.1364/JOSAA.4.000488. http://josaa.osa.org/abstract.cfm?URI=josaa-4-3-488 (cit. on p. 32).

[63] C. Corsi. "History highlights and future trends of infrared sensors". In: *Journal of Modern Optics* 57 (2010), pp. 1663 –1686 (cit. on pp. 33, 34).

[64] A. Karim and J. Y. Andersson. "Infrared detectors: Advances, challenges and new technologies". In: *IOP Conference Series: Materials Science and Engineering* 51 (2013), p. 012001. DOI: 10.1088/1757-899x/51/1/012001. https://doi.org/10.1088/1757-899x/51/1/012001 (cit. on pp. 33, 34).

[65] *Electronic Imaging in Astronomy*. Springer Berlin Heidelberg, 2008. DOI: 10.1007/978-3-540-76583-7. https://doi.org/10.1007/978-3-540-76583-7 (cit. on p. 34).

[66] Y.-R. Nowicki-Bringuier and P. Chorier. "Sofradir SWIR hyperspectral detectors for space applications". In: *Sensors, Systems, and Next-Generation Satellites XIII*. Ed. by R. Meynart, S. P. Neeck, and H. Shimoda. Vol. 7474. International Society for Optics and Photonics. SPIE, 2009, pp. 396 –407. DOI: 10.1117/12.830721. https://doi.org/10.1117/12.830721 (cit. on p. 35).

[67] T. Eversberg and K. Vollmann. *Spectroscopic Instrumentation*. Springer Berlin Heidelberg, 2015. DOI: 10.1007/978-3-662-44535-8. https://doi.org/10.1007/978-3-662-44535-8 (cit. on p. 41).

[68] F. Kerschbaum and I. Muller. "Otto von Littrow and his spectrograph". In: *Astronomische Nachrichten* 330.6 (June 2009), p. 574. DOI: 10.1002/asna.200911219 (cit. on p. 41).

[69] W. Neumann. "Fundamentals of Dispersive Optical Spectroscopy Systems". In: 2014 (cit. on pp. 41, 43, 45).

[70] F. Sigernes. "The EbertFastie SpectrometerControl Hardwareand Software". In: (cit. on p. 43).

[71] P. D. Feldman, R. C. Henry, and H. W. Moos. "William George Fastie". In: *Physics Today* 54.5 (May 2001), pp. 82–83. DOI: 10.1063/1.1381116. https://doi.org/10.1063/1.1381116 (cit. on p. 43).

[72] M. Tang et al. “General study of asymmetrical crossed Czerny–Turner spectrometer”. In: *Appl. Opt.* 54.33 (2015), pp. 9966–9975. DOI: 10.1364/AO.54.009966. http://ao.osa.org/abstract.cfm?URI=ao-54-33-9966 (cit. on p. 46).

[73] Y. An et al. “The design of astigmatism-free crossed Czerny-Turner spectrometer”. In: *Optik* 124.16 (2013), pp. 2539–2543. ISSN: 0030-4026. DOI: https://doi.org/10.1016/j.ijleo.2012.07.009. https://www.sciencedirect.com/science/article/pii/S0030402612005773 (cit. on p. 46).

[74] A. B. Shafer, L. R. Megill, and L. Droppleman. “Optimization of the Czerny–Turner Spectrometer∗”. In: *J. Opt. Soc. Am.* 54.7 (1964), pp. 879–887. DOI: 10.1364/JOSA.54.000879. http://www.osapublishing.org/abstract.cfm?URI=josa-54-7-879 (cit. on pp. 46, 62).

[75] P. Jacquinot. “The Luminosity of Spectrometers with Prisms, Gratings, or Fabry-Perot Etalons”. In: *J. Opt. Soc. Am.* 44.10 (1954), pp. 761–765. DOI: 10.1364/JOSA.44.000761. http://www.osapublishing.org/abstract.cfm?URI=josa-44-10-761 (cit. on p. 48).

[76] C. Fehrenbach. “Comparison of the efficiency of prism and grating spectrographs”. In: *Vistas in Astronomy* 1 (1955), pp. 414–422. ISSN: 0083-6656. DOI: https://doi.org/10.1016/0083-6656(55)90053-2. https://www.sciencedirect.com/science/article/pii/0083665655900532 (cit. on p. 48).

[77] R. G. Bingham. “Grating spectrometers and spectrographs re-examined”. In: *QJRAS* 20 (Dec. 1979), pp. 395–421 (cit. on pp. 50, 57).

[78] Thorlabs. *Mid-IR Ruled Reflective Diffraction Gratings*. https://www.thorlabs.com/newgrouppage9.cfm?objectgroup_id=8628&pn=GR2550-30035. [Online; accessed 27-May-2021] (cit. on p. 55).

[79] Edmund Optics. *Richardson Gratings™ High Precision Plane Ruled Reflective Diffraction Gratings*. https://www.edmundoptics.eu/f/richardson-gratingst-high-precision-plane-ruled-reflective-diffraction-gratings/37274/. [Online; accessed 27-May-2021] (cit. on p. 55).

[80] Nil Technology. *Blazed gratings*. https://www.nilt.com/technology/blazed-gratings/. [Online; accessed 27-May-2021] (cit. on p. 55).

[81] Dynasil. *High Quality Ruled Gratings*. https://www.dynasil.com/product-category/diffraction-gratings/ruled-diffraction-gratings. [Online; accessed 27-May-2021] (cit. on p. 55).

[82] Gratinglab. *Plane Ruled Reflection Gratings*. https://www.gratinglab.com/Products/Product_Tables/T2.aspx#. [Online; accessed 27-May-2021] (cit. on p. 55).

[83] Opcolab. *Typical Stock Grating Efficiency Curves*. https://www.opcolab.com/capabilities/optical-products/ruled-diffraction-gratings/stock-gratings/. [Online; accessed 27-May-2021] (cit. on p. 55).

[84] T. P. Instruments. *New Aberration-Free Spectrographs Improve Signal-to-Noise Ratio of Spectral Data*. 2019. https://www.princetoninstruments.com/wp-content/uploads/2020/04/TechNote_AberrationFreeImproveSNR.pdf (cit. on p. 62).

[85] M. Czerny and A. F. Turner. "Uber den Astigmatismus bei Spiegelspektrometern". In: *Zeitschrift fur Physik* 61.11-12 (Nov. 1930), pp. 792–797. DOI: 10.1007/bf01340206. https://doi.org/10.1007/bf01340206 (cit. on p. 62).

[86] D. R. Austin, T. Witting, and I. A. Walmsley. "Broadband astigmatism-free Czerny-Turner imaging spectrometer using spherical mirrors". In: *Appl. Opt.* 48.19 (2009), pp. 3846–3853. DOI: 10.1364/AO.48.003846. http://ao.osa.org/abstract.cfm?URI=ao-48-19-3846 (cit. on pp. 63, 64).

[87] Q. Xue, S. Wang, and F. Lu. "Aberration-corrected Czerny-Turner imaging spectrometer with a wide spectral region". In: *Appl. Opt.* 48.1 (2009), pp. 11–16. DOI: 10.1364/AO.48.000011. http://ao.osa.org/abstract.cfm?URI=ao-48-1-11 (cit. on pp. 63, 64).

[88] F. A. Jenkins and H. E. White. "Fundamentals of Optics". In: *Acta Crystallographica* 11.4 (1958), pp. 314–314. DOI: https://doi.org/10.1107/S0365110X58002723. eprint: https://onlinelibrary.wiley.com/doi/pdf/10.1107/S0365110X58002723. https://onlinelibrary.wiley.com/doi/abs/10.1107/S0365110X58002723 (cit. on p. 63).

[89] Q. Xue. "Astigmatism-corrected Czerny–Turner imaging spectrometer for broadband spectral simultaneity". In: *Appl. Opt.* 50.10 (2011), pp. 1338–1344. DOI: 10.1364/AO.50.001338. http://ao.osa.org/abstract.cfm?URI=ao-50-10-1338 (cit. on p. 64).

[90] K.-S. Lee, K. P. Thompson, and J. P. Rolland. "Broadband astigmatism-corrected Czerny–Turner spectrometer". In: *Opt. Express* 18.22 (2010), pp. 23378–23384. DOI: 10.1364/OE.18.023378. http://www.opticsexpress.org/abstract.cfm?URI=oe-18-22-23378 (cit. on pp. 64, 65).

[91] M. McDowell. "Design of Czerny-Turner Spectrographs Using Divergent Grating Illumination". In: *Optica Acta: International Journal of Optics* 22.5 (1975), pp. 473–475. DOI: 10.1080/713819063. eprint: https://doi.org/10.1080/713819063. https://doi.org/10.1080/713819063 (cit. on p. 64).

[92] Synopsys. CODE V. 2016 (cit. on p. 66).

[93] *Fiber Optic Cable single-mode multi-mode Tutorial*. https://web.archive.org/web/20181023040952/https://arcelect.com/fibercable.htm. (Accessed on 05/30/2021) (cit. on p. 79).

[94] D. F. Gray. *The Observation and Analysis of Stellar Photospheres*. 2008 (cit. on p. v).

[95] Thorlabs. *Optics selection guide*. https://www.thorlabs.com/images/Catalog/V19_08_Optics.pdf (cit. on p. vi).

[96] Public Domain. *Atmospheric transmittance spectrum of Earth*. https://commons.wikimedia.org/w/index.php?curid=34818020.